

**CHARACTERIZING THE MECHANICAL, TRANSPORT AND
ADHESION PROPERTIES OF HYDROGELS USING
INDENTATION METHOD**

A Dissertation
Presented to
The Academic Faculty

by

Yang Lai

In Partial Fulfillment
of the Requirements for the Degree
Doctor of Philosophy in the
School of Mechanical Engineering

Georgia Institute of Technology
August 2020

COPYRIGHT © 2020 BY YANG LAI

**CHARACTERIZING THE MECHANICAL, TRANSPORT AND
ADHESION PROPERTIES OF HYDROGELS USING
INDENTATION METHOD**

Approved by:

Dr. Yuhang Hu, Advisor
School of Mechanical Engineering
Georgia Institute of Technology

Dr. Shuman Xia
School of Mechanical Engineering
Georgia Institute of Technology

Dr. Ting Zhu
School of Mechanical Engineering
Georgia Institute of Technology

Dr. Julie Champion
School of Chemical & Biomolecular
Engineering
Georgia Institute of Technology

Dr. Todd Sulchek
School of Mechanical Engineering
Georgia Institute of Technology

Date Approved: May 22, 2020

ACKNOWLEDGEMENTS

First and foremost, I wish to thank my advisor, Dr. Yuhang Hu, for supporting me during the time of my Ph.D. study. I appreciate her guidance and feedback on doing research since I entered the program and her patience as I was learning along the way. Her advice and insight on research are invaluable to me, and her enthusiasm for this field has been inspiring. I would also like to thank the professors in my committee, Dr. Ting Zhu, Dr. Shuman Xia, Dr. Todd Sulchek, and Dr. Julie Champion, for their helpful suggestions on this thesis project.

I would like to extend my gratitude to Dr. Scott MacLaren and Dr. Kathy Walsh in UIUC, for their teaching and helpful tips on conducting experiments on the atomic force microscope.

Many thanks to my colleagues, all the past and present members in the Hu research group. I would like to acknowledge the great help from Dongjing He in discussing ideas and carrying out calculations in several topics, and many valuable discussions and feedbacks from Inkyu Oh, Jiahe Huang, Haohui Zhang, Jiehao Chen, Bohan Wang, and Yifu Chen, and help in experiments from Qinan Zhou and Yefei Si. I very much appreciate the nice and supportive atmosphere created by all the members of the group.

Lastly, I would like to thank my parents for all their love and encouragement. And thanks to my boyfriend for his support and understanding. Thank you.

TABLE OF CONTENTS

ACKNOWLEDGEMENTS	iii
LIST OF TABLES	vi
LIST OF FIGURES	vii
LIST OF SYMBOLS AND ABBREVIATIONS	xiii
SUMMARY	xix
CHAPTER 1. INTRODUCTION	1
1.1 Hydrogels in Nature and Engineering Applications	1
1.2 Applying Indentation Technique to Hydrogels	2
1.3 Characterization of Mechanical and Transport Properties of Hydrogels	4
1.3.1 Mechanical and Transport Parameters of Hydrogels in the Theory of Linear Poroelasticity	4
1.3.2 Using Indentation to Measure the Mechanical and Transport Properties of Hydrogels	5
1.4 Characterization of Adhesion Properties of Hydrogels	7
1.5 Polyacrylamide Hydrogel as a Model Material for Studying Hydrogel Mechanics	9
1.6 Thesis Organization	9
CHAPTER 2. DEVELOPING THE METHOD OF POROELASTIC DYNAMIC INDENTATION	12
2.1 Introduction	12
2.2 Linear Poroelasticity Applied on Gels	13
2.3 The Poroelastic Oscillation Indentation Method	17
2.3.1 Design of Experimental Procedure	17
2.3.2 Analytical Solution	21
2.3.3 Theoretical Results	26
2.3.4 Differentiation between Viscoelasticity and Poroelasticity	31
2.4 Experiments	34
2.5 Conclusion	38
CHAPTER 3. PROBING THE SWELLING-DEPENDENT MECHANICAL AND TRANSPORT PROPERTIES OF POLYACRYLAMIDE HYDROGELS	40
3.1 Introduction	40
3.2 Experiments	42
3.3 Results and Discussion	50
3.4 Modifying the Flory-Rehner Model for Hydrogels	59
3.5 Conclusion	75
CHAPTER 4. STUDY OF ADHESION PROPERTIES OF HYDROGELS USING INDENTATION OVER A WIDE RANGE OF LENGTH AND TIME SCALES	76

4.1	Introduction	76
4.2	Experiments	77
4.2.1	Fabrication of Hydrogel Samples	77
4.2.2	Indentation Adhesion Tests using Atomic Force Microscope	77
4.2.3	Indentation Adhesion Tests using Microindenter	79
4.3	Results and Discussion	80
4.3.1	Time-Dependent Adhesion of Hydrogels	80
4.3.2	Length-Dependent Pull-Off Force and Energy of Separation	90
4.3.3	Modified Maugis-Dugdale Model	92
4.4	Conclusion	100
 CHAPTER 5. STUDY OF ADHESION PROPERTIES OF HYDROGELS WITH DIFFERENT COMPOSITIONS		102
5.1	Introduction	102
5.2	Experiments	103
5.2.1	Preparation of Hydrogel Samples	103
5.2.2	Indentation Adhesion Experiment on AFM	104
5.2.3	Indentation Adhesion Experiment on Microindenter	107
5.3	Results and Discussion	107
5.3.1	Force Response of Hydrogels in Indentation Adhesion Tests	108
5.3.2	Adhesion Parameters Obtained from the Modified Maugis-Dugdale Model	115
5.4	Conclusion	131
 CHAPTER 6. CONCLUSIONS		132
 APPENDIX A. Experimental data		135
A.1	Phase Lag Degree Results for Dynamic Indentation Tests	135
A.2	Calculating the Shear Moduli of Hydrogel Samples in Chapter 5	144
 REFERENCES		145

LIST OF TABLES

Table 3.1	Compositions of the polyacrylamide hydrogels for the study of swelling-dependent poroelastic properties.....	60
Table 3.2	Fitting results of parameters G_1 , G_2 and K_e	68
Table 4.1	List of the fitting slope of the pull-off force and energy of separation against contact time results from AFM and microindenter tests under different indentation depths in Figure 4.4.....	89
Table 5.1	Compositions of the polyacrylamide hydrogel samples.	104

LIST OF FIGURES

Figure 1.1	Schematic of the molecular structure of gels consisting of cross-linked polymer network and solvent molecules.....	2
Figure 2.1	A representative volume element of a gel is in a homogeneous state. Work can be done to the element by mechanical load σ_{ij} and pumping solvent molecules with chemical potential μ into it.	15
Figure 2.2	A gel body is in an inhomogeneous state. The mechanical boundary can be enforced by mechanical forces \mathbf{T} or displacement constraints \mathbf{u} . Chemical boundary can be enforced by the environment chemical potential μ or the solvent flux \mathbf{J} . Each small piece of the gel is marked by the coordinate x . The gel evolves through a sequence of inhomogeneous states.	17
Figure 2.3	The schematics of poroelastic oscillation indentation experiment for three shapes of indenters: (a) cylindrical punch indenter, (b) spherical indenter, and (c) conical indenter.....	19
Figure 2.4	(a) Schematic of the testing procedure of the poroelastic oscillation: an indenter is pressed into the material to a fixed depth h_0 , which is held constant for a period of time until the force on the indenter reaches a constant value, and then an oscillation indentation of small magnitude δh is superimposed with a wide range of different frequencies. The phase lag can be obtained by comparing the shift between the displacement and force spectra. (b) The phase lag can also be calculated by quantifying the energy dissipated through one cycle of the loading and unloading process from Equation (2-10).	20
Figure 2.5	The master force relaxation function for cylindrical punch is plotted. (a) The Abaqus simulation result is plotted together with the original two-term fitting function. (b) The Abaqus simulation result is plotted together with the four-term fitting function used in this study.	25
Figure 2.6	The analytical solution of the phase lag degree Δ , which is a universal plot for cylindrical punch, spherical indenter, and conical indenter. The phase lag degree is a function of two variables: the normalized angular frequency Ω and the Poisson's ratio ν	27
Figure 2.7	(a) The Poisson's ratio is plotted against the critical phase lag degree. (b) The critical normalized angular frequency is plotted against the Poisson's ratio. The black solid lines are the analytical solutions; the blue squares, green triangles and red circles are numerical results from finite element analysis for cylindrical punch, conical and spherical indenters respectively; and the orange dash lines are the fitting functions.	29

Figure 2.8	Schematics to illustrate the method of multi-depth oscillation indentation to differentiate poroelastic and viscoelastic behaviors of soft hydrated materials. Two peaks of the phase lag (Δ_c^{visco} and Δ_c^{poro}) are expected corresponding to viscoelastic and poroelastic effects respectively. The black, blue and red curves are from indentations with different radius of contact $a_1 < a_2 < a_3$. (a) The critical frequency corresponding to the viscoelastic peak is independent of contact size. (b) The critical frequency corresponding to the poroelastic peak inversely scales with contact radius squared.	32
Figure 2.9	Experimental results of oscillation indentation on PAAm gel under one oscillation frequency using the atomic force microscope. (a) Indentation depth (black line) and indenting force (blue line) are recorded as functions of time. (b) The force-displacement curve recorded during one cycle of loading and unloading.....	36
Figure 2.10	Experimental results of dynamic indentation on PAAm gel under a wide range of actuation frequencies. (a) Phase lag degree is plotted against the angular frequency for three different depths of indentations. (b) Phase lag degree is plotted against the product of angular frequency and contact radius squared for the three depths of indentations.	37
Figure 3.1	Mechanical characterization of gels in different swelling ratios. (a) Indentation of gels using AFM. (b) The swelling ratio of the PAAm gel against the concentration of the external PEG solution.	44
Figure 3.2	Dynamic indentation of PAAm gels swollen in pure water: (a) the displacement and force spectrums, (b) force response in one oscillation cycle at 1.22 Hz, (c) phase lag degree versus actuation angular frequency, (d) phase lag degree versus angular frequency times contact radius squared. The sphere radius and the indentation depth for each group of data are: red: $R=12.5 \mu\text{m}$, $h_0=1.0 \mu\text{m}$, green: $R=12.5 \mu\text{m}$, $h_0=0.5 \mu\text{m}$, blue: $R=12.5 \mu\text{m}$, $h_0=0.25 \mu\text{m}$, grey: $R=2.25 \mu\text{m}$, $h_0=0.25 \mu\text{m}$	46
Figure 3.3	Dynamic indentation of PAAm gels in PEG solutions of different concentrations. Sphere size and indentation depth for (a) and (b) are: Blue: $R=12.5 \mu\text{m}$, $h_0=0.25 \mu\text{m}$; Green: $R=12.5 \mu\text{m}$, $h_0=0.5 \mu\text{m}$; Red: $R=12.5 \mu\text{m}$, $h_0=1.0 \mu\text{m}$; Grey: $R=2.25 \mu\text{m}$, $h_0=0.25 \mu\text{m}$. Sphere size and indentation depth for (c) and (d) are: Blue: $R=2.25 \mu\text{m}$, $h_0=0.25 \mu\text{m}$; Green: $R=2.25 \mu\text{m}$, $h_0=0.5 \mu\text{m}$; Red: $R=2.25 \mu\text{m}$, $h_0=0.75 \mu\text{m}$; Grey: $R=12.5 \mu\text{m}$, $h_0=2.0 \mu\text{m}$	47
Figure 3.4	The phase lag degree measured in the dynamic indentation tests at three individual frequencies. The PAAm gel was swollen in water, and the indentation depth was around 500 nm.	48
Figure 3.5	Loading and unloading curve from the AFM indentation test with a speed of 50 nm/s. The Hertzian model fits well to the loading curve and most of the unloading curve.....	50

Figure 3.6	Linear poroelastic properties of the PAAM gels: (a) shear modulus, (b) Poisson's ratio, and (c) diffusivity against swelling ratios.	53
Figure 3.7	Thermodynamic properties of the PAAM gels: (a) the parameter N , (b) the Flory-Huggins interaction parameter χ , and (c) the effective pore size for solvent transport d , against swelling ratios.	57
Figure 3.8	The swelling ratio of the polyacrylamide hydrogels against the mass concentration of the external PEG solution. In the legend, the letter A means the concentration of acrylamide, and the letter B means the concentration of N,N' -Methylenebis(acrylamide).	61
Figure 3.9	The experimental results for the four hydrogel compositions at different swelling ratios. (a) The shear modulus. (b) The Poisson's ratio. (c) The diffusivity.	62
Figure 3.10	Experimental results and the fitting curves of the shear modulus and Poisson's ratio as functions of the swelling ratio. (a) (b): acrylamide 10%, bisacrylamide 0.2%. (c) (d): acrylamide 8%, bisacrylamide 0.2%. (e) (f): acrylamide 6%, bisacrylamide 0.2%. (g) (h) acrylamide 6%, bisacrylamide 0.4%.	67
Figure 3.11	Fitting curve for the Flory-Huggins interaction parameter χ as a function of the swelling ratio.	69
Figure 3.12	Fitting of the modified model when forcing $G_2 = 0$. (a) shows the results on the shear modulus. (b) shows the results on the Poisson's ratio. The purple curves represent a set of fitting parameters that only fits the shear modulus better ($G_1 = 1.631E4$ Pa, $K_e = 1.612E6$ Pa, $\beta = 20$). The blue curves represent another set of fitting parameters that only fit the Poisson's ratio better ($G_1 = 0.820E4$ Pa, $K_e = 6.953E6$ Pa, $\beta = 50$).	70
Figure 3.13	Fitting of the modified model when forcing $K_e = 0$. (a) shows the results on the shear modulus. (b) shows the results on the Poisson's ratio. The green curves represent a set of fitting parameters that only fits the shear modulus better ($G_1 = 1.582E4$ Pa, $G_2 = 0.793E4$ Pa, $\beta = 350$). The orange curves represent another set of fitting parameters that only fit the Poisson's ratio better ($G_1 = 1.419E4$ Pa, $G_2 = 0.905E4$ Pa, $\beta = 40$).	70
Figure 3.14	Best fitting results of the modified model when forcing $\beta = 1$ ($G_1 = 0.868E4$ Pa, $G_2 = 1.462E4$ Pa, $K_e = 3.068E6$ Pa). (a) shows the results on the shear modulus. (b) shows results on the Poisson's ratio.	71
Figure 3.15	Permeability of the polyacrylamide hydrogels at different swelling ratios. .	75
Figure 4.1	Testing method. (a) Displacement-controlled indentation testing procedure on AFM. (b) The measured force-time curve on AFM. (c) The force-displacement plot from AFM test. (d) Displacement controlled indentation testing procedure	

- on microindenter. (e) The measured force-time curve on microindenter. (f) The force-displacement plot from the microindenter test. 81
- Figure 4.2 Time-dependent poroelastic behaviors of gels. The force relaxation curves from AFM and microindenters are plotted as (a) normalized force $(P(t)-P(\infty))/(P(0)-P(\infty))$ against time t , and (b) normalized force $(P(t)-P(\infty))/(P(0)-P(\infty))$ against normalized time t/c_0^2 . The black, red, and blue solid lines are from AFM measurements with a contact radius of 1.94, 2.50, and 3.06 μm respectively. The black, red and blue dash lines are from microindenter measurements with contact radius of 43.6, 61.6 and 75.5 μm respectively.. 83
- Figure 4.3 Measurements at different contact times. (a) The force-time plot of AFM tests with a series of different contact times before retraction. The sphere is of 12.5 μm radius, and indentation depth is 0.5 μm during holding. (b) The force-time plot of microindenter tests with a series of different contact times before retraction. The sphere is of 190 μm radius, and indentation depth is 20 μm during holding. In both AFM and microindenter tests, the unloading rate is 25 $\mu\text{m/s}$ 86
- Figure 4.4 Time-dependent adhesion. (a) Pull-off force and (b) energy of separation are plotted as a function of contact time at different indentation depths in AFM experiments (indenter radius 12.5 μm). (c) Pull-off force and (d) energy of separation are plotted as a function of contact time at different indentation depths in microindenter experiments (indenter radius 190 μm). 88
- Figure 4.5 Length-dependent pull-off force and energy of separation. (a) Pull-off force and (b) energy of separation are plotted as functions of contact radius under 10 seconds contact time. (c) Pull-off force and (d) energy of separation are plotted as functions of contact radius for 120 seconds contact time..... 92
- Figure 4.6 Modified Maugis-Dugdale model. (a) Schematics of the cohesive model and illustration of the retraction process. (b) Analytical result of the normalized force-displacement curve at a few different values of the normalized initial contact radius $\mathbf{c0}$, for $\lambda=2$. (c) The setup of the numerical simulation in Comsol. (d) Comparison of the numerical and theoretical results for the case of $\mathbf{c0} = 2$ and $\lambda=2$ for verification of the analytical result. (e) The normalized pull-off force and (f) the normalized energy of separation against normalized initial contact radius $\mathbf{c0}$, at different values of parameter λ 94
- Figure 4.7 (a) Pull-off force as a function of initial contact radius for both experimental and theoretical fitting; (b) Energy of separation as a function of initial contact radius for both experimental and theoretical fitting. (c) Fitting results of adhesion energy as a function of contact time. (d) Fitting results of adhesion strength and separation distance as a function of contact time. 100
- Figure 5.1 Illustration of the indentation depth-time relation in (a) an AFM test and (b) a microindenter test. Result of the contact force-time relation from (c) an AFM

	test and (d) a microindenter test. Result of the force-indentation depth relation from (e) an AFM test and (f) a microindenter test.	106
Figure 5.2	Illustration of the pull-off forces as functions of holding time at different indentation depths. (a) Results from the AFM tests. (b) Results from the microindenter tests.	110
Figure 5.3	Illustration of the pull-off forces across different initial contact radii for the hydrogel samples. The empty signs are results from the AFM tests, and the full signs are results from the microindenter tests. Inserted figures show the results from the AFM tests with the zoomed-in x-axis.	113
Figure 5.4	Illustration of curve fitting for holding time of 2 s (red), 20 s (yellow) and 120 s (blue) for hydrogel sample No.1.	114
Figure 5.5	Adhesion energy versus holding time for (a) the first group of hydrogel samples and (b) the second group of hydrogel samples. Cohesive strength versus holding time for (c) the first group of hydrogel samples and (d) the second group of hydrogel samples. Separation distance versus holding time for (e) the first group of hydrogel samples and (f) the second group of hydrogel samples.	117
Figure 5.6	Mass concentration of polymer in the hydrogels after reaching swelling equilibrium in water. (a) The first group of hydrogels. (b) The second group of hydrogels.	119
Figure 5.7	(a) Adhesion energy versus polymer concentration at equilibrium. (b) Adhesion energy versus surface chain density. Results are from the holding time of 180s.	122
Figure 5.8	(a) Cohesive strength versus polymer concentration at equilibrium. (b) Cohesive strength versus surface chain density. Results are from the holding time of 180s.	124
Figure 5.9	(a) Separation distance versus the average chain size. (b) Separation distance versus the straightened chain length. Results are from the holding time of 180 s.	126
Figure 5.10	Mechanism of hydrogel adhesion at the length scale of a single polymer chain. The gray semi-sphere represents the indenter surface. The dark blue chains are polymer chains, the dark blue circles are crosslinkers, the orange circles represent monomers that are in adhesive contact with the indenter surface. The yellow dashed circles illustrate the deformation of the surface polymer chain. (a) Before contact, the polymer chain on the hydrogel surface is in a stress-free state. (b) Upon contact, the entire polymer chain deforms following the bulk compressive strain, only a few monomers in close contact with the indenter can form adhesive sites. (c) After relatively short holding time, some monomers close to the initial adhesive sites form adhesive contact with the	

indenter. (d) Upon unloading, the polymer chain is stretched to pull off the adhered monomers. (e) After a longer holding time, more monomers close to the initial adhesive sites form adhesive contact with the indenter. (f) When unloading after longer holding time, the polymer chain is stretched more to pull off more adhered monomers..... 130

LIST OF SYMBOLS AND ABBREVIATIONS

- C Solvent molecule concentration (linear poroelastic model)
- C_0 Initial solvent molecule concentration (linear poroelastic model)
- μ Chemical potential
- μ_0 Initial chemical potential
- W Free energy of a representative volume element
- σ_{ij} Stress
- ε_{ij} Strain
- V_0 Volume of a single solvent molecule
- G Shear modulus
- ν Poisson's ratio
- x_i Coordinate of a representative volume element
- t Time
- u_i Displacement of a representative volume element
- J_i Flux of solvent molecules

- k Permeability
- η Dynamic viscosity of solvent
- D Diffusivity of solvent in gel
- \bar{T}_l Traction boundary condition
- \bar{u}_l Displacement boundary condition
- $\bar{\mu}$ Chemical potential boundary condition
- \bar{J}_l Diffusion boundary condition
- h Indentation depth
- h_0 Initial indentation depth
- δh Oscillation amplitude in dynamic indentation method
- ω Angular frequency
- F Indenting force
- Δ Phase lag
- F_a Oscillation amplitude of indenting force
- Δ_c Critical phase lag degree
- ω_c Critical angular frequency

a_{cp} Contact radius with cylindrical punch indenter

R_{cp} Radius of cylindrical punch indenter

a_s Contact radius with the spherical indenter

R_s Radius of the spherical indenter

a_c Contact radius with conical indenter

θ Half angle of the conical indenter

w Displacement in the vertical direction

r Radial position with respect to the axisymmetric axis of indenter

λ_L A function of the Poisson's ratio

τ Normalized time

Ω Normalized angular frequency

f Normalized force in cylindrical punch indentation

Ω_c Critical normalized angular frequency

N Number of polymer chains per unit volume of dry polymer

χ Flory-Huggins interaction parameter

λ_{SR} Linear swelling ratio

m_{hydrogel}	Mass of hydrogel
m_{polymer}	Mass of dry polymer
ρ_{polymer}	Density of dry polymer
ρ_{water}	Density of water
F_{iK}	Deformation gradient
k_B	Boltzmann constant
T	Temperature
X_i	Reference coordinate
d	Pore size
τ_t	Tortuosity
φ	Porosity
β_t	Parameter for pore geometry
G_1	Parameter in the Mooney-Rivlin model
G_2	Parameter in the Mooney-Rivlin model
K_e	Parameter in modified Flory-Rehner model
β	Parameter in modified Flory-Rehner model

- p_a Parameter in Koningsveld and Kleintjens (KK) expression
- p_b Parameter in Koningsveld and Kleintjens (KK) expression
- p_c Parameter in Koningsveld and Kleintjens (KK) expression
- Φ Polymer concentration
- P Contact force
- R Radius of the spherical indenter
- c Apparent contact radius
- c_0 Initial contact radius (Initial apparent contact radius)
- P_{pf} Pull-off force
- W_s energy of separation
- \bar{P} Normalized contact force in Maugis-Dugdale model
- δ Indentation depth in Maugis-Dugdale model
- $\bar{\delta}$ Normalized indentation depth in Maugis-Dugdale model
- \bar{c}_0 Normalized initial contact radius in Maugis-Dugdale model
- A Normalized contact radius
- γ Adhesion energy

- λ Parameter in Maugis-Dugdale model
- σ_0 Cohesive strength
- l_0 Separation distance
- K Reduced modulus
- E Young's modulus
- s Surface chain density
- l_f Average polymer chain size
- l_s Straightened polymer chain length
- l_{cb} Length of carbon-carbon bond
- C_∞ Flory's characteristic ratio
- n Average number of monomers per polymer chain
- N_A Avogadro constant
- M Molar mass of monomer acrylamide
- m_c Average number of monomers forming contact per polymer chain
- R_p Radius of a polymer chain blob
- b_0 Molecular distance for forming adhesive contact

SUMMARY

Hydrogels are crosslinked polymer networks that imbibe a large amount of water. Various hydrogels exist both in nature and in engineering applications. The mechanical, transport and adhesion properties of hydrogels are all important properties to characterize. The indentation method is practically suitable for hydrogels, but extracting material properties from indentation tests on hydrogels is still challenging, especially at a small length scale. There is a need to establish a set of indentation methods that considers both the current instrument capability and the hydrogel properties. In this study, robust indentation methods are developed to characterize the mechanical, transport and adhesion properties of hydrogels, which can be applied on instruments such as the atomic force microscope and the micro-indenter.

In this thesis, two methods, the dynamic indentation method and the indentation adhesion method are developed for characterizing hydrogels' poroelastic properties and adhesion properties, respectively. The dynamic indentation method proposes to superimpose a fixed indentation depth with a small-amplitude oscillation and to obtain the poroelastic properties from the frequency-dependent force response. The dynamic indentation method is further applied to several hydrogel samples to probe their swelling-dependent properties. With the measurements, the applicability of a widely used nonlinear thermodynamics model for hydrogels, the Flory-Rehner model, is examined, and a modification to the model is suggested.

The indentation adhesion method proposes to conduct indentation tests at a wide range of contact radius for the contact time of interest and to extract adhesion parameters

from the results obtained at different contact radii. To establish the method, the adhesion behavior of a model hydrogel is examined at a wide range of contact time and length scales, and the existing contact mechanics models are proved to be not adequate to explain the results. Therefore, a modified model is developed in this thesis to properly extract the adhesion parameters. This indentation adhesion method is further applied to hydrogels with different compositions to study the possible relation between the adhesion parameters and the hydrogel composition.

CHAPTER 1. INTRODUCTION

1.1 Hydrogels in Nature and Engineering Applications

Hydrogels are composed of cross-linked polymer networks infused with a large amount of water as solvent molecules (Figure 1.1). In nature, many bio-tissues can be categorized as hydrogels, typical examples including cornea¹, cartilage², mucus³, and brain tissues^{4,5} in animals, alginate and pectin in plants⁶, as well as biofilms⁷. In engineering fields, synthetic hydrogels are invented and fabricated, applications including wound dressings⁸, contact lenses^{9,10}, drug delivery vehicles¹¹⁻¹⁴, culturing structures for cell growth and tissue engineering¹⁵⁻¹⁷, sensors^{18,19}, actuators^{20,21}, speakers²², soft robots²³, wearable electronics^{24,25} and many others.

In both the biological environment and engineering setting, hydrogels are always in contact with other substances, bearing load and constantly exchanging solvent and other small molecules with the surrounding environment. The appropriate mechanical, transport and adhesion properties are critical for the normal functioning of many hydrogels. For living tissues, the flow-deformation-coupled reactions and the bonding and debonding of specific molecules both contribute to the communication and coordination between cells and between different parts of the tissue²⁶. For some bio-tissues, having specific surface properties are necessary, either being highly adhesive to hold the tissue on specific locations²⁶, such as biofilms²⁷, or being less adhesive for a better lubrication property, such as mucus, cornea and cartilage^{1,3,28}. Meanwhile, synthetic gels are designed with a specific range of elastic modulus, and with the capability to selectively allow solvent and other chemical species to diffuse in and out. The surface properties for synthetic hydrogels also

varies. While most hydrogels are slippery, some synthetic hydrogels are being developed to be highly adhesive even under water, capable of gluing surfaces from soft hydrated tissues²⁹ to hard impenetrable materials^{30,31}. For all these scenarios, quantifying and understanding the mechanisms contributing to the mechanical, transport and adhesion properties of hydrogels are of significant importance.

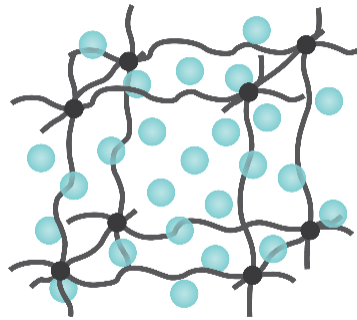


Figure 1.1 Schematic of the molecular structure of gels consisting of cross-linked polymer network and solvent molecules.

1.2 Applying Indentation Technique to Hydrogels

Various methods have been used to measure the mechanical properties of hydrogels, including tensile test^{32,33}, compression test^{34–37}, shear rheology^{38,39} and indentation test^{40,41}. The traditional experimental settings, such as the tensile test and the compression test, face challenges on hydrogels, because most gels are soft, slippery and brittle. Among the various characterization methods, indentation⁴² is a more suitable method for hydrogels as it requires minimal sample preparation, can be easily conducted in liquid, and can be

performed several times on a single specimen. Indentation can also be easily applied in different length scales. In macroscopic scale (e.g. cm to m), indentation tests can be carried out using normal testing machines with a macro-sized indenter^{40,43}. In a smaller length scale (e.g. μm to mm), the indentation tests can be conducted on micro-/nano-indenters⁴⁴ and atomic force microscopes (AFM)⁴⁵⁻⁴⁸. For samples with very small sizes or with inhomogeneous properties, such as biological materials, indentation is the only method that can be conveniently applied in small-scale measurement.

Indentation is also the most suitable method for adhesion measurement on soft hydrated materials, especially on small length scale⁴⁹⁻⁵². Other existing methods for measuring material adhesion include peeling test and rolling test. Peeling test has been widely used to characterize the adhesion properties of materials. Although it is easy to be applied on samples as long as the instability of surface separation is not invoked⁵³, the peeling test is not applicable for inhomogeneous materials or very small samples. Rolling test has also been explored to characterize the adhesion of materials,^{54,55} but it is only applicable to homogeneous and flat surfaces. It also requires a more complicated experimental setup. Comparatively, indentation can be used to probe adhesion at a length scale as small as submicron, thus capable of testing a wide range of soft hydrated materials. For materials with moderate or small adhesion, the effect of adhesion becomes larger at a smaller contact length scale⁵⁶. Therefore, indentation tests carried out on instruments such as atomic force microscopes or micro-indenters can provide adhesion measurements of higher accuracy.

To extract material properties from the indentation measurements, one needs to solve the specific boundary value problem with a suitable material constitutive model and a

surface interaction model. In the past, this type of indentation problem has been solved for the linear elastic material^{42,57,58} and elastic-plastic material⁴², and the indentation technique has been widely applied on these materials. For soft hydrated materials, some of the existing contact mechanics models are applied to interpret the measurements from indentation tests^{59–62}. However, due to the difference between the physics of hydrogels and the assumptions in the existing models, the calculated results of material parameters may not solely reflect the intrinsic material properties, but also include other factors from the experiments. It is also difficult to compare the results across different literature because different settings of experiments may invoke different mechanisms, and different models chosen for analyzing the data may ignore different factors. There are still questions to be answered for a complete understanding of the mechanical, transport and adhesion properties of hydrogels, being either the bio-tissues that are long existing in nature or the synthetic hydrogels that are newly developed. Developing robust contact mechanics models for measuring hydrogel properties is necessary to answer the existing questions, yet the related studies are still in the state of infancy.

1.3 Characterization of Mechanical and Transport Properties of Hydrogels

1.3.1 Mechanical and Transport Parameters of Hydrogels in the Theory of Linear Poroelasticity

Hydrogels exhibit time-dependent mechanical properties, which can be attributed to two mechanisms, the viscoelasticity due to the reconfiguration of polymer chains⁶³ and the poroelasticity due to solvent migration inside the polymer network^{64–66}. The viscoelastic

response is independent of the characteristic length in the experiment, while the poroelastic response is related to the characteristic length scale of the experiment⁶⁷. Using this difference, it has been shown that the time-dependent behavior of covalently crosslinked gels is mostly dominated by poroelastic effect.⁴⁰

Hydrogels under small deformation can be described by the model of linear poroelasticity^{64,65}, which was originally developed for soils and rocks⁶⁸, and lately applied on soft hydrated materials such as hydrogels and biological tissues^{40,69–76}. The theory of linear poroelasticity describes the coupling behavior of the hydrogel: the flow of liquid causes the network to deform, meanwhile the deformation of the network also causes the solvent to flow. There are three material parameters in the theory: the shear modulus, the Poisson's ratio and the diffusivity^{64,65,77}. The shear modulus describes the difficulty of inducing shear strain of the polymer network in the hydrogel. The definition of the Poisson's ratio in linear poroelasticity is different from that in the linear elastic model. For hydrogels under small loading, both the molecules of the polymer network and molecules of solvent are assumed to be incompressible. Under loading, the hydrogel changes volume mainly by solvent molecules being squeezed out or imbibed into the polymeric network. The Poisson's ratio represents the volume change of the hydrogel caused by solvent flow after the chemical potential equilibrium of the solvent is reached. The parameter diffusivity in linear poroelasticity represents the rate of diffusion of solvent molecules inside hydrogels driven by the gradient of chemical potential. The shear modulus, Poisson's ratio and diffusivity are all phenomenological parameters.

1.3.2 Using Indentation to Measure the Mechanical and Transport Properties of Hydrogels

To extract the mechanical and transport parameters of hydrogels from the indentation measurements, the exact relation between the measured force and the material parameters is needed, which requires solving a mixed boundary value problem corresponding to a specific indentation procedure (e.g. relaxation test, creep test, or dynamic oscillation test)^{40,78,79}, and with a specific material constitutive model. Meanwhile, it is expected that the indentation procedure is designed in such a way that all the material parameters can be determined from the force measurements conveniently.

In the past, a poroelastic relaxation indentation method has been developed and applied on several types of gels.⁴⁰ This method adopts the linear poroelastic model, which is phenomenological but general for a wide range of soft hydrated materials. In this method, an indenter is set to press onto the hydrogel surface with a fast speed, and then hold at a constant indentation depth over time. The solvent molecules inside the hydrogels will flow due to the change of chemical potential until a new state of equilibrium is reached, the entire process causing the contact force to relax to a constant value. The three parameters defined in the theory of linear poroelasticity can be determined simply by fitting the relaxing force curve to a master curve derived in the poroelastic relaxation method, without the need of further parameter fitting with excess numerical simulations.

Although the poroelastic relaxation method has been demonstrated robust for measuring hydrogels' poroelasticity on a large length scale (i.e. cm), practically it is difficult to be applied on a small length scale. The poroelastic relaxation time scales with contact radius squared⁴⁰, so when the size of contact is small, the poroelastic relaxation time is short. The typical diffusivity of a hydrogel is on the order of $10^{-10} \sim 10^{-11}$ m²/s. For a micro-indentation with a radius of contact around 1 μ m, the relaxation time is on the

order of 0.01 ~ 0.1 s. As a result, it becomes difficult to capture an accurate instantaneous force after the indenter is applied rapidly on the material and hauled to stop. On the other hand, the idea of measuring poroelastic properties of hydrogels at a small length scale is still intriguing, not only because of the increasing demand of characterizing samples with small sizes or inhomogeneous properties, but also because of the possibility of greatly reducing the entire testing time by the shortened relaxation time. Therefore, there is still a need for a robust method that can characterize the poroelasticity of hydrogels in small length scales.

1.4 Characterization of Adhesion Properties of Hydrogels

Adhesion of hydrogels is a complicated problem, as adhesion properties of hydrogels can be related to several factors, such as polymer chemistry⁴⁹, surface topology³¹, even contact time^{49,80}. Indentation tests on hydrogels may provide information for understanding the different roles played by various possible factors. However, interpreting the results from indentation measurements is still challenging. Although there are several methods available to extract adhesion properties from indentation measurements, it is not clear whether the existing methods are applicable and robust for hydrogels, considering the difference between the physics of hydrogels and the assumptions made in these methods.

The force-displacement curve obtained from an indentation measurement has been used to extract adhesion properties⁸¹⁻⁸⁴. Often, people report the pull-off force and/or energy of separation from the indentation measurements^{10,60,85}. Because neither of the two values is material intrinsic, the measured values are different for different size and

geometry, and thus are not readily comparable across the literature. A more rigorous approach is to analyze the data and extract the adhesion energy of the contacting surfaces through particular adhesion models. The widely used models include the Derjaguin-Muller-Toporov (DMT) model⁸⁶, and the Johnson-Kendall-Roberts (JKR) model⁸¹. Each model has its own assumptions, limitations, and ranges of applications^{87,88}. Generally speaking, the DMT model is more suitable for contacting surfaces that are hard, small in radius, and low in adhesion energy, while the JKR model is more suitable for contacting surfaces that are soft, large in radius, and high in adhesion energy. Maugis introduced the cohesive zone into the contact problem and derived a general solution that connects JKR and DMT approximations and determines the applicability of each theory⁸⁸. For soft materials such as polymers and polymeric gels, the JKR model has been widely adopted^{51,61,89,90}. However, for soft hydrated materials, such as hydrogels and soft biological tissues, it is not clear that JKR is readily applicable before knowing their exact surface and bulk properties. First of all, although these materials are soft, the adhesion energy of these materials in the underwater environment is also small^{52,91}, and the loosely crosslinked polymer chains on the surface may lead to long-range adhesion force underwater. At a small length scale, these factors imply the possibility of a cohesive zone of finite size, and thus the necessity of using the Maugis-Dugdale model, rather than the JKR model. Additionally, these materials have complicated time-dependent behaviors involving reconfiguration of polymer chains and solvent migration^{63,66} which may lead to adhesion hysteresis between loading and unloading^{51,52}, but this phenomenon has not been thoroughly studied. Therefore, a systematic and integrated study of theory and experiment

is still in need to examine the applicability of the existing models, especially on hydrogels tested underwater.

1.5 Polyacrylamide Hydrogel as a Model Material for Studying Hydrogel Mechanics

Hydrogels in nature and engineering applications are composed of polymer networks with different chemistries and are crosslinked with different types of bonds. To develop a general understanding of the mechanical and transport properties of hydrogels, model hydrogels are used to build theories and explore unknown behaviors. Among the model hydrogels, the polyacrylamide (PAAm) hydrogel has often been used. Polyacrylamide hydrogels are formed through free-radical polymerization of monomer (Acrylamide) and crosslinker (*N,N'*-Methylenebis(acrylamide)) in water, and have stable properties after they are made⁹². The polyacrylamide hydrogel is a routinely used material in fields such as biology and bioengineering⁹³, and there are previous studies reporting the measurements of its mechanical properties using traditional methods and models^{77,94-96}. In recent years, polyacrylamide hydrogel has also been used as a model material to further study hydrogels' mechanical, transport and surface properties^{41,97-103}.

1.6 Thesis Organization

This thesis aims at developing robust indentation methods that can measure hydrogels' mechanical, transport and adhesion properties, especially on a small length

scale, and studying the key factors influencing these properties using the model hydrogels. The thesis is composed of five chapters, with the first chapter being the introduction of the background and motivation for each study.

In Chapter 2, a dynamic indentation method is developed to measure the linear poroelastic parameters of hydrogels on the small length scale. In this chapter, the procedure of the dynamic indentation method is proposed, and the solutions to the corresponding boundary value problems are calculated. A simple procedure to extract the linear poroelastic properties from experimental measurements is suggested. This method is illustrated experimentally on a polyacrylamide hydrogel.

In Chapter 3, the dynamic indentation method is applied to study the swelling-dependent mechanical and transport properties of polyacrylamide hydrogels. By relating the linear poroelastic parameters at different swelling ratios to the thermodynamics parameters in the Flory-Rehner model, the assumption of the thermodynamic parameters being constants is examined quantitatively. Based on the measurements on the polyacrylamide hydrogels with more compositions, modifications of the Flory-Rehner model for hydrogels are suggested.

In Chapter 4, an indentation adhesion method is developed to measure hydrogels' adhesion properties. Before developing the method, indentation relaxation tests are carried out on a polyacrylamide hydrogel in a wide range of length and time scales to examine the applicability of the existing adhesion models. Based on the analysis of the experimental observations, a modified contact mechanics model is developed that can predict the length-

dependent adhesion behavior of hydrogels and can give consistent adhesion parameters of hydrogels.

In Chapter 5, the indentation adhesion method is used to study the relation between the adhesion parameters of hydrogels and the hydrogel composition. Polyacrylamide hydrogels with different compositions are prepared and tested using the indentation adhesion method, and their adhesion parameters are extracted. The possible dependence of the adhesion parameters on the polymer chain parameters are discussed, and a more detailed mechanism of hydrogel adhesion is proposed.

CHAPTER 2. DEVELOPING THE METHOD OF POROELASTIC DYNAMIC INDENTATION

2.1 Introduction

This chapter aims at developing a poroelastic dynamic indentation method, which can solve the challenge of obtaining poroelastic properties of hydrogels using the indentation technique at small length scales.

In recent years, AFM has become a widely used technique for characterizing soft materials due to its flexibility in choosing cantilevers of different stiffness and tips of different shapes.⁴⁶⁻⁴⁸ For AFM, the driving speed of the indenter is limited by the piezo actuator. When using an AFM to carry out the poroelastic relaxation indentation test on a hydrogel, the hydrogel will start to relax before the preset indentation depth is reached, and the poroelastic parameters could not be accurately obtained by fitting the force relaxation curve. On the other hand, AFM can still apply indentation accurately when the indenting velocity is not very high, such as an oscillation indentation even with a wide range of frequencies (0.1 ~ 100 Hz). It is therefore expected that the force response from an oscillation-patterned indentation can provide information on both the mechanical and transport properties of a hydrogel, and the question has been how to relate the experimentally measured data to the material properties.

In this chapter, a detailed loading process of a dynamic indentation test is first proposed, in which small oscillation in a series of frequencies is superimposed on a larger initial indentation depth, and the force on the indenter is measured. A phase lag exists

between the displacement and the force spectra due to the dissipative nature of the solvent diffusion in the gel. The corresponding boundary value problem is solved using a linear poroelastic material model, both analytically and numerically, aiming to provide simple solutions for extracting material properties. The dynamic indentation problem is a mixed boundary value problem, which requires displacement boundary within the contact area, and stress-free boundary outside of the contact area. When the flow of liquid is considered as in poroelasticity, the boundary is impermeable within the contact area and permeable outside of the contact area. Three shapes of indenters, including cylindrical punches, spheres, and conical indenters are analyzed, and a unified form of solutions are obtained. A simple approach is suggested for extracting material parameters from the oscillation indentation measurements. Finally, a complete process of applying the dynamic indentation method is illustrated on a polyacrylamide (PAAm) gel.

2.2 Linear Poroelasticity Applied on Gels

To adapt poroelasticity^{64,65,68} to gels, there are two important considerations. Firstly, although gels can absorb a large amount of solvent and generate volume change as large as 1000 times of its original size, indentation is induced after the gel swells to a certain state. Shallow indentation is applied, so the deformation induced by indentation remains in the linear region. Secondly, since most gels are soft and brittle, the stress they can support is usually small. Under this condition, the individual polymer chains and solvent molecules in gels can be viewed as incompressible. Therefore, the volume change of the

gel is entirely due to the change of the solvent amount, which is a widely adapted assumption in literature^{70,104,105}.

Consider a representative volume element of gels undergoing homogeneous deformation. As shown in Figure 2.1, the element in the reference state is stress-free with a concentration of solvent C_0 (i.e. the number of solvent molecules per unit volume) and chemical potential μ_0 . Work can be done to the element by both mechanical and chemical load,

$$\delta W = \sigma_{ij} \delta \varepsilon_{ij} + (\mu - \mu_0) \delta C, \quad (2-1)$$

where σ_{ij} is the stress, μ is the chemical potential in the current state, $\delta \varepsilon_{ij}$ is the corresponding strain, and $\delta C = C - C_0$ is the change of solvent concentration, which is related to the volume change of the element as

$$\varepsilon_{kk} = V_0 (C - C_0), \quad (2-2)$$

with V_0 being the volume of a single solvent molecule.

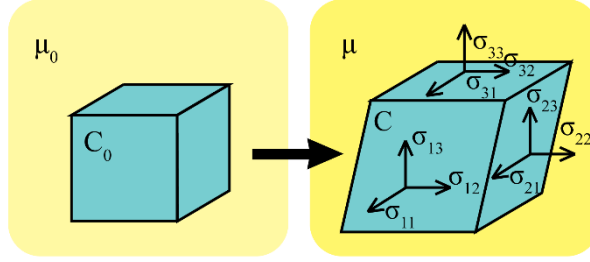


Figure 2.1 A representative volume element of a gel is in a homogeneous state. Work can be done to the element by mechanical load σ_{ij} and pumping solvent molecules with chemical potential μ into it.

For linear elastic and isotropic material, W can be written as,

$$W = G \left[\varepsilon_{ij} \varepsilon_{ij} + \frac{\nu}{1 - 2\nu} (\varepsilon_{kk})^2 \right], \quad (2-3)$$

where G is the shear modulus, and ν is the Poisson's ratio.

Substituting Equations. (2-2) and (2-3) into Equation (2-1), the constitutive behavior of the material in a state of equilibrium can be expressed as,

$$\sigma_{ij} = 2G \left(\varepsilon_{ij} + \frac{\nu}{1 - 2\nu} \delta_{ij} \varepsilon_{kk} \right) - \delta_{ij} \frac{\mu - \mu_0}{V_0}. \quad (2-4)$$

Taking a gel body, the displacement is a time-dependent field $u_i = u_i(x_1, x_2, x_3, t)$. (Figure 2.2)

The deformation is assumed to be small. The kinematic relation gives

$$\varepsilon_{ij} = \frac{1}{2} \left(\frac{\partial u_i}{\partial x_j} + \frac{\partial u_j}{\partial x_i} \right). \quad (2-5)$$

The balance of force requires that

$$\frac{\partial \sigma_{ij}}{\partial x_j} = 0. \quad (2-6)$$

The conservation of solvent molecules requires that

$$\frac{\partial C}{\partial t} + \frac{\partial J_k}{\partial x_k} = 0. \quad (2-7)$$

where $C(x_i, t)$ denotes a field of solvent concentration, and $J_k(x_i, t)$ is the flux (i.e. the number of solvent molecules passing through a unit area per second), which is driven by the chemical potential gradient. Darcy's law⁶⁴ is adapted as the kinetic model,

$$J_i = -\frac{k}{\eta V_0^2} \frac{\partial \mu}{\partial x_i}. \quad (2-8)$$

Here k is the permeability, and η is the dynamic viscosity of the solvent.

A combination of Equations (2-4), (2-6), (2-7), (2-8) gives a diffusion equation

$$\frac{\partial C}{\partial t} = D \nabla^2 C. \quad (2-9)$$

where $D=[2(1-\nu)/(1-2\nu)]Gk/\eta$ is the diffusivity describing the migration rate of solvent in the polymer network. This equation indicates that the time for response is dominated by diffusion and scales with the square of a characteristic length specified by the boundary value problem, e.g. the contact radius in the indentation problem.

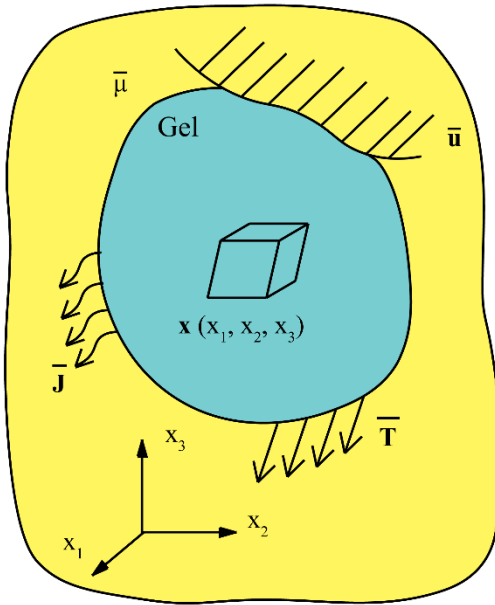


Figure 2.2 A gel body is in an inhomogeneous state. The mechanical boundary can be enforced by mechanical forces \bar{T} or displacement constraints \bar{u} . Chemical boundary can be enforced by the environment chemical potential $\bar{\mu}$ or the solvent flux \bar{J} . Each small piece of the gel is marked by the coordinate x . The gel evolves through a sequence of inhomogeneous states.

To solve for the equations above, two categories of boundary conditions need to be specified: the chemical potential $\bar{\mu}$ or the flux of solvent molecules \bar{J}_i , and the traction \bar{T}_i or displacement \bar{u}_i boundary conditions.

2.3 The Poroelastic Oscillation Indentation Method

2.3.1 Design of Experimental Procedure

The most widely used shapes of indenters for testing soft gels and biological tissues are spherical indenters, cylindrical punches, and high-angle conical indenters. The

schematics of these indenters pressing onto the gel samples are illustrated in Figure 2.3. The gels are first submerged in solvent until fully swollen, and then the indenters are pressed into the gels. During testing, both the gels and the indenters are submerged in the solvent. The method of poroelastic oscillation indentation is illustrated in Figure 2.4. An indenter is pressed into the gel to a certain depth h_0 and held for a period of time until a plateau in the measured relaxation force is reached. Right after the relaxation, an additional oscillation indentation of small depth $\delta h e^{i\omega t}$ is applied ($\delta h \ll h_0$) sweeping through a wide range of angular frequencies ω . The indenter's vertical displacement h and the force on the indenter F are recorded as functions of time. The phase lag Δ between the displacement and the force spectra can be obtained as a function of angular frequency ω , either by identifying the shift of periodicity between force and displacement signals as illustrated in Figure 2.4(a) or by calculating the energy dissipated through one cycle of loading and unloading using the following equation:

$$\Delta = \arcsin \left(\frac{\oint F dh}{\pi F_a \delta h} \right), \quad (2-10)$$

where F_a is the oscillation amplitude of the force on the indenter (Figure 2.4(b)).

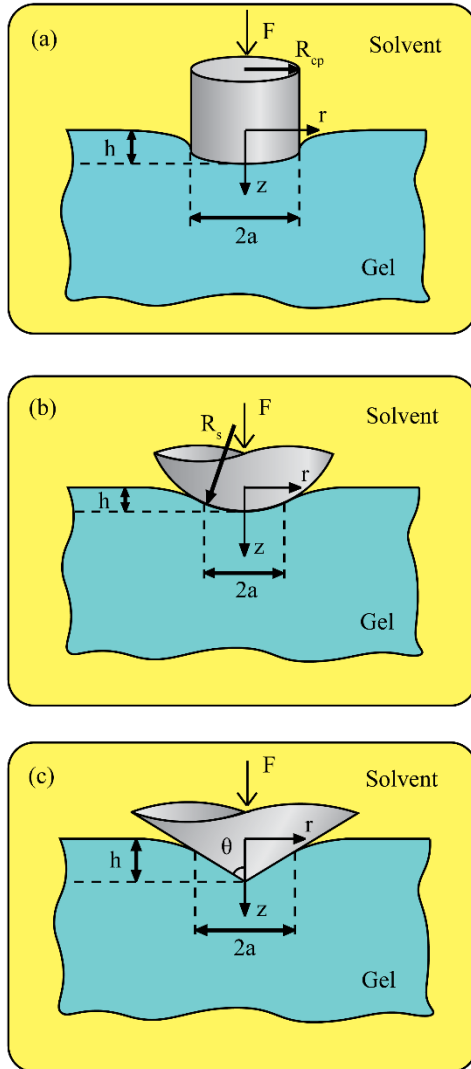


Figure 2.3 The schematics of poroelastic oscillation indentation experiment for three shapes of indenters: (a) cylindrical punch indenter, (b) spherical indenter, and (c) conical indenter.

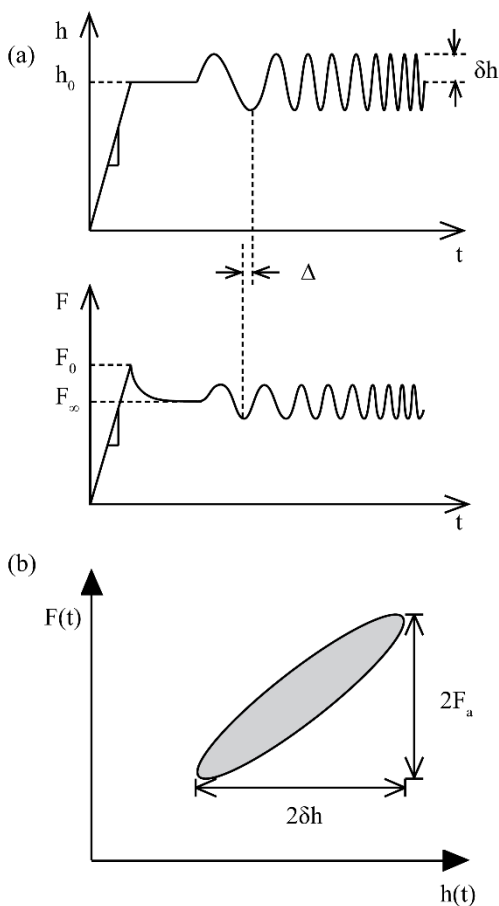


Figure 2.4 (a) Schematic of the testing procedure of the poroelastic oscillation: an indenter is pressed into the material to a fixed depth h_0 , which is held constant for a period of time until the force on the indenter reaches a constant value, and then an oscillation indentation of small magnitude δh is superimposed with a wide range of different frequencies. The phase lag can be obtained by comparing the shift between the displacement and force spectra. (b) The phase lag can also be calculated by quantifying the energy dissipated through one cycle of the loading and unloading process from Equation (2-10).

In the recorded $\Delta-\omega$ plot, a peak value of the phase lag Δ_c with respect to a particular angular frequency ω_c is expected, representing the characteristic diffusion behavior of the gel. The value of the peak phase lag Δ_c is related to the amount of solvent that can be squeezed out of the gel, and thus contains information that can be used to characterize the

Poisson's ratio of the gel, ν . The critical angular frequency is related to the rate of diffusion of the solvent in the network, and thus contains information that can be used to characterize the diffusivity of the gel, D . With a known value of the Poisson's ratio, the shear modulus of the gel can be calculated through classical solutions of elastic indentation. The detailed calculation and interpretations are described below.

2.3.2 Analytical Solution

The oscillation amplitude is kept small compared with the initial depth of indentation: $\delta h \ll h_0$. Under this condition, the contact radius can be assumed to be constant and equals the elastic solutions for the three shapes of indenters,

$$a_{cp} = R_{cp}, \quad (2-11a)$$

$$a_s \approx \sqrt{R_s h_0}, \quad (2-11b)$$

$$a_c \approx \frac{2h_0}{\pi} \tan(\theta). \quad (2-11c)$$

The subscripts “ cp ”, “ s ” and “ c ” denote cylindrical punch, spherical indenter, and conical indenter, respectively.^{58,106}

In oscillation indentation, the depth of indentation is a function of time. Within the radius of contact, the vertical displacements introduced by the three indenters for a depth of indentation $h(t)$ are⁵⁸

$$w_{cp}(r, t) = h(t), \quad (2-12a)$$

$$w_s(r, t) = h(t) - \left(R_s - \sqrt{R_s^2 - r^2} \right), \quad (2-12b)$$

$$w_c(r, t) = h(t) - \frac{r}{\tan(\theta)}, \quad (2-12c)$$

where r is the radial position with respect to the axisymmetric axis of the indenters (Figure 2.3). For oscillation indentation, the indentation depth is $h(t)=h_0+\delta h e^{i\omega t}$. Substituting it into Equation (2-12) leads to a unified expression for the displacement boundary within the contact radius

$$w(r, t) = w_0(r) + \delta h e^{i\omega t}. \quad (2-13)$$

Equation (2-13) is a universal expression for the three shapes of indenters with w_0 being different for different shapes, which can be obtained from Equation (2-12). The second term on the right-hand side of Equation (2-13) is independent of radial position r and is equivalent to a displacement field induced by a cylindrical indenter with an effective punch radius equal to the radius of contact a that can be obtained from Equation (2-11) corresponding to three shapes of indenters. Therefore, the overall displacement boundaries for the three indenters are all equivalent to the summation of an initial cylindrical, spherical, or conical indentation with a constant depth h_0 , and an oscillatory cylindrical indentation with a depth of $\delta h e^{i\omega t}$ that depends on time.

Under this condition, the force on the indenter can be written as¹⁰⁷

$$F_{cp}(t) = 8Gh_0a_{cp}(1 - \lambda_L) + 8Ga_{cp}(1 - \lambda_L)\delta h e^{i\omega t} \quad (2-14a)$$

$$+8Ga_{cp} \int_{-\infty}^t \lambda_L f \left(\frac{D(t-t')}{a_{cp}^2} \right) \delta h i \omega e^{i\omega t'} dt',$$

$$F_s(t) = \frac{16}{3} Gh_0 a_s (1 - \lambda_L) + 8Ga_s (1 - \lambda_L) \delta h e^{i\omega t} \quad (2-14b)$$

$$+8Ga_s \int_{-\infty}^t \lambda_L f \left(\frac{D(t-t')}{a_s^2} \right) \delta h i \omega e^{i\omega t'} dt',$$

$$F_c(t) = 4Gh_0 a_c (1 - \lambda_L) + 8Ga_c (1 - \lambda_L) \delta h e^{i\omega t} \quad (2-14c)$$

$$+8Ga_c \int_{-\infty}^t \lambda_L f \left(\frac{D(t-t')}{a_c^2} \right) \delta h i \omega e^{i\omega t'} dt'.$$

for cylindrical punch, spherical indenter and conical indenter respectively. The solutions for the three shapes of indenters share the same features: the overall force is the sum of three parts including a time-independent term that depends on indenter shape, a time-dependent term that is in phase with the displacement oscillation $\delta h e^{i\omega t}$ and another time-dependent term that is out of phase with the displacement oscillation. Both of the two time-dependent terms are independent of the indenter shape. It can be considered as an elastic indent of cylindrical, spherical, or conical shaped indenter plus an oscillation indent of a cylindrical shaped indenter. A unified expression for the three shapes of indenters can be written as

$$F(t) = F_0 + 8Ga\delta h \left[i\lambda_L \Omega \int_0^\infty f(\tau) e^{-i\Omega\tau} d\tau + (1 - \lambda_L) \right] e^{i\omega t}. \quad (2-15)$$

where F_0 is time-independent, $\lambda_L=(1-2\nu)/[2(1-\nu)]$, $\tau=Dt/a^2$ is the normalized time, and Ω is the normalized angular frequency

$$\Omega = \frac{a^2\omega}{D}, \quad (2-16)$$

with D being the diffusivity of the gel, and a the radius of contact induced by h_0 depth of indentation, which is different for the three indenters as shown in Equation (2-11a). The kernel function $f(\tau)$ is the normalized force relaxation function of a cylindrical punch indenting a half-space poroelastic material, which has been proved to be a master curve independent of material properties and has been derived by fitting a numerical result obtained from the finite element calculation with a continuous function, that is⁴⁰

$$f(\tau) = 1.304e^{-\sqrt{\tau}} - 0.304e^{-0.254\tau}. \quad (2-17a)$$

This original fitting function provided in Reference 40 contains two exponential terms. The numerical results from ABAQUS simulation and the fitting function are plotted in Figure 2.5. It is shown that the fitting function fits well with the simulation results to most of the extend. However, because the phase lag calculation in this study is very sensitive to the relaxation function, for more accurate fitting, a modified fitting function with four terms is introduced.

$$f(\tau) = 0.242 \exp(-3.13\tau) + 0.536 \exp(-1.71\sqrt{\tau}) \quad (2-17b)$$

$$-0.043 \exp\left(-12.8\tau^{\frac{1}{3}}\right) + 0.266 \exp\left(-0.892\tau^{\frac{1}{4}}\right),$$

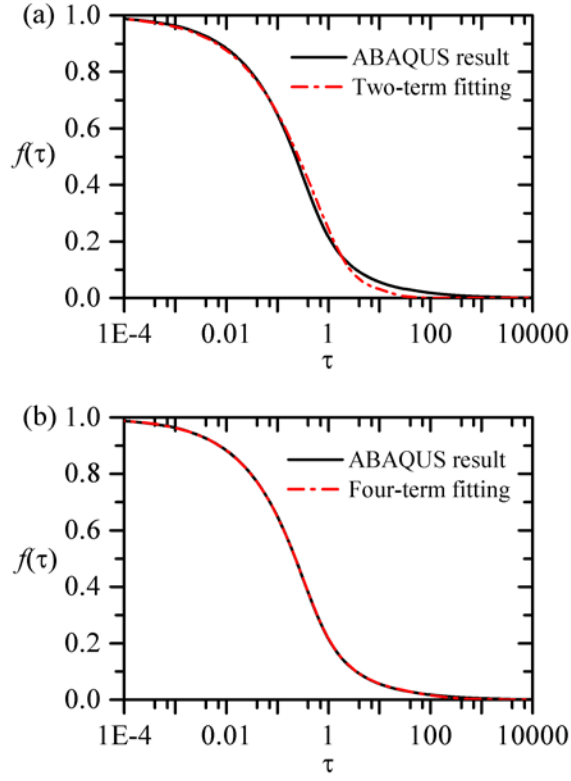


Figure 2.5 The master force relaxation function for cylindrical punch is plotted. (a) The Abaqus simulation result is plotted together with the original two-term fitting function. (b) The Abaqus simulation result is plotted together with the four-term fitting function used in this study.

Substituting Equation (2-17b) into Equation (2-15), the phase lag for the oscillation indentation can be obtained as,

$$\Delta = \arctan \left(\frac{\text{Im} \left(i\lambda_L \Omega \int_0^{\infty} f(\tau) e^{-i\Omega\tau} d\tau + (1 - \lambda_L) \right)}{\text{Re} \left(i\lambda_L \Omega \int_0^{\infty} f(\tau) e^{-i\Omega\tau} d\tau + (1 - \lambda_L) \right)} \right). \quad (2-18)$$

Equation (2-18) is a universal equation for the three shapes of indenters. It shows that the phase lag is a function of only two independent variables, the normalized angular frequency Ω and the Poisson's ratio ν , and most importantly the relation is independent of indenter shape.

2.3.3 Theoretical Results

The results for the analytical solution of the phase lag function $\Delta(\Omega, \nu)$ are shown in Figure 2.6. The phase lag degree is plotted against normalized angular frequency for several values of Poisson's ratio from 0.0 to 0.5 with an interval of 0.1. The results show that the phase lag approaches zero when the normalized angular frequency is close to either zero or infinity, and reaches a maximum value at a particular frequency. At small frequencies, the movement of the indenter is slow compared with the migration of the solvent molecules, and the chemical potential in the material is instantaneously in equilibrium, resulting in a small or no phase shift between force and displacement spectra. At large frequencies, the movement of the indenter is so fast that allows no time for the solvent to move, resulting in also a small or no shift between force and displacement spectra. At intermediate frequencies, over a cycle of loading and unloading, solvent flows in and out of the gel, resulting in energy dissipation, and thus a shift in the measured force spectrum with respect to the applied displacement spectrum. The magnitude of the phase lag value is related to the ability of the gel to lose or absorb solvent, which is reflected by the Poisson's ratio of the material. The phase lag at the peak is denoted as the critical phase lag Δ_c , and the corresponding normalized angular frequency as critical normalized angular frequency Ω_c , and they are plotted as functions of the material's Poisson's ratio, as shown in Figure 2.7(a) and Figure 2.7(b). It is shown that the peak value of phase lag Δ_c increases

from 0 to 12 as Poisson's ratio changes from 0.5 to 0, while the normalized angular frequency Ω_c only slightly depends on Poisson's ratio, which increases slightly from 2 to 2.8 as Poisson's ratio changes from 0 to 0.5.

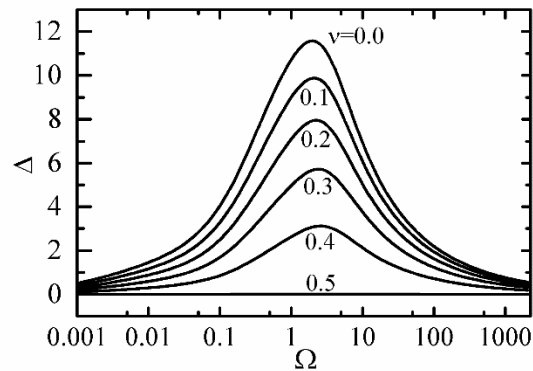


Figure 2.6 The analytical solution of the phase lag degree Δ , which is a universal plot for cylindrical punch, spherical indenter, and conical indenter. The phase lag degree is a function of two variables: the normalized angular frequency Ω and the Poisson's ratio ν .

Numerical simulation using ABAQUS was conducted to validate the analytical results. The indentation was modeled as an axisymmetric problem. The indenters were set as analytical rigid parts. The “Soil” type solver was used in the calculation. The dimensions of the gel in both radial and axial directions were set to be much larger than the radius of contact (i.e. 200 times of the contact radius). Forty elements were assigned along the radius of contact. The numerical results were checked insensitive to further increase in gel size or further decrease in mesh element size. The contact area between the indenter and the material was set to be impermeable and frictionless, while the surface

outside of the contact area was set to be traction free and zero chemical potential, which was to simulate local equilibrium condition with the external solvent. Two consecutive steps were carried out in the simulation. In the first step, the indenter was pressed into the poroelastic material into a depth of h_0 and was subsequently held constant for a period of time. After the first step, another small depth of indentation δh was applied in a form of sinusoidal oscillation. The same calculations were carried out for a wide range of oscillation frequencies. The reaction force acting on the indenter was solved, and the phase lag was calculated for each oscillation frequency using Equation (2-10).

The scaling relation in Equation (2-18) was verified by varying different parameters. The results confirm that the phase lag is a function of two parameters: the Poisson's ratio of the material and the normalized angular frequency. For each shape of the indenter, a group of simulations was conducted at different normalized angular frequencies ranging from 0.2 to 64, at Poisson's ratio of 0, 0.1, 0.2, 0.3, and 0.4. For each value of Poisson's ratio, the critical phase lag and normalized angular frequency were located and plotted as the square, triangle and spherical dots in Figure 2.7, for cylindrical punch, conical and spherical indenters respectively.

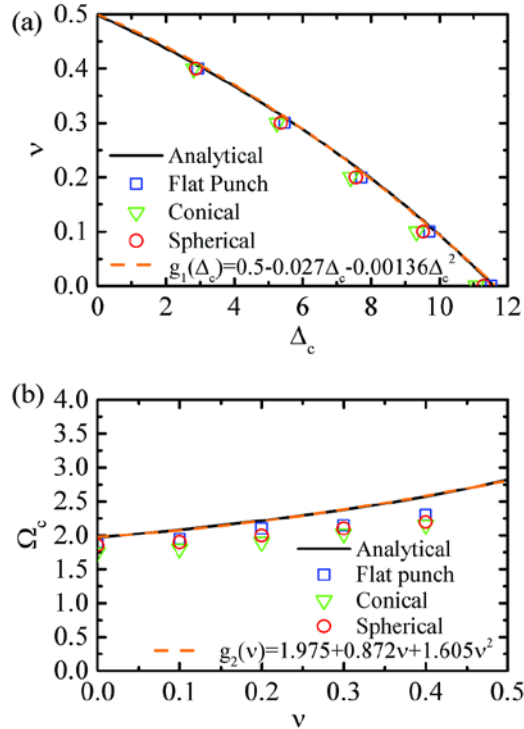


Figure 2.7 (a) The Poisson's ratio is plotted against the critical phase lag degree. (b) The critical normalized angular frequency is plotted against the Poisson's ratio. The black solid lines are the analytical solutions; the blue squares, green triangles and red circles are numerical results from finite element analysis for cylindrical punch, conical and spherical indenters respectively; and the orange dash lines are the fitting functions.

As is shown, the simulation results fit well with the analytical solutions for the three shapes of indenters with a numerical error of less than 5%. The slightly higher deviation between the analytical solution and the numerical results at the higher value of the Poisson's ratio is because when Poisson's ratio is close to 0.5, the amount of solvent that flows in and out of the material element through each cycle becomes small, causing less energy dissipation. As a result, the numerical error is more sensitive in the case of larger Poisson's ratio.

If the material shows predominantly poroelastic behavior, the solutions derived in this study can be used to extract material parameters including shear modulus G , Poisson's ratio ν , and diffusivity D . For ease to use, the solutions shown in Figure 2.7 are fitted with continuous functions as $\nu = g_1(\Delta_c)$, and $\Omega_c = g_2(\nu)$. The fitting functions are

$$\nu = g_1(\Delta_c) = 0.5 - 0.027\Delta_c - 0.00136\Delta_c^2, \quad (2-19)$$

$$\Omega_c = g_2(\nu) = 1.975 + 0.872\nu + 1.605\nu^2. \quad (2-20)$$

The two functions are plotted as dashed lines in Figure 2.7. Using these equations and the two values from experiments: the critical phase lag Δ_c and corresponding critical angular frequency ω_c , the Poisson's ratio ν and diffusivity D of the materials can be directly calculated. Firstly, substituting the value of Δ_c into Equation (2-19) gives Poisson's ratio as $\nu = g_1(\Delta_c)$. Then, substituting ν into Equation (2-20) gives a theoretical value of the normalized critical angular frequency from $\Omega_c = g_2(\nu)$, which is related to the diffusivity of the material as

$$D = \frac{a^2 \omega_c}{\Omega_c}. \quad (2-21)$$

Finally, the shear modulus is obtained from the reaction force at the end of the relaxation step when an equilibrium state is reached (Figure 2.4(b)). Denote the equilibrium force as $F(\infty)$, the shear modulus can be calculated from the classical linear elastic solutions as

$$G_{cp} = \frac{(1 - \nu)F(\infty)}{4h_0a}, \quad (2-22a)$$

$$G_s = \frac{3(1 - \nu)F(\infty)}{8h_0a}, \quad (2-22b)$$

$$G_c = \frac{(1 - \nu)F(\infty)}{2h_0a}. \quad (2-22c)$$

2.3.4 Differentiation between Viscoelasticity and Poroelasticity

Gels and many soft biological tissues are composed of both polymeric networks and solvent. Their time-dependent behavior could be both poroelastic due to the migration of solvent and viscoelastic due to the reconfiguration of polymer chains. Macroscopically, the two mechanisms will result in two different peaks in the spectrum of phase lag versus frequency in an oscillation indentation test if an appropriate range of contact radius is selected. Then the two effects can be potentially differentiated through a method of multi-depth oscillation indentation. In the experiment, the dynamic oscillation measurement is conducted repeatedly for two or more times, each time with a different depth of indentation, e.g. $h_{01} < h_{02} < h_{03}$. The radii of contact can be calculated from Equation (2-11) which gives $a_1 < a_2 < a_3$. In each test, the phase lag between displacement and force spectra can be reported as a function of actuation frequency.

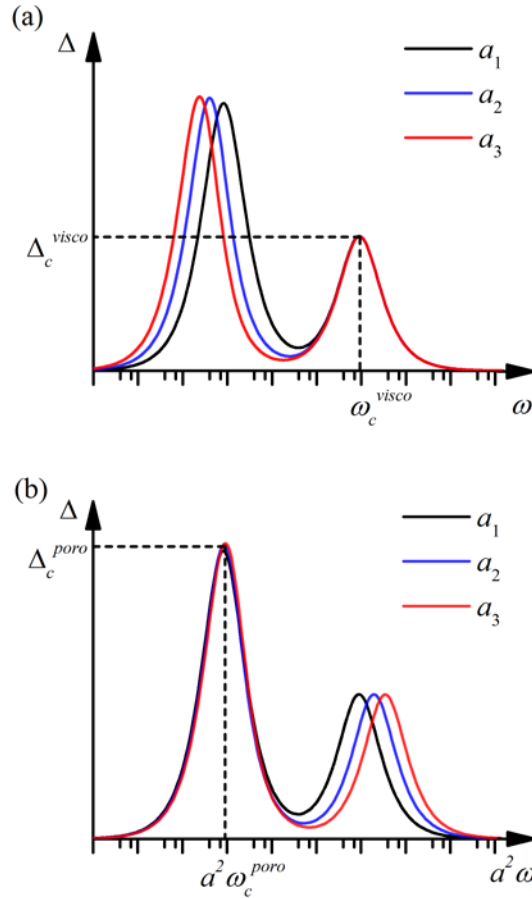


Figure 2.8 Schematics to illustrate the method of multi-depth oscillation indentation to differentiate poroelastic and viscoelastic behaviors of soft hydrated materials. Two peaks of the phase lag (Δ_c^{visco} and Δ_c^{poro}) are expected corresponding to viscoelastic and poroelastic effects respectively. The black, blue and red curves are from indentations with different radius of contact $a_1 < a_2 < a_3$. (a) The critical frequency corresponding to the viscoelastic peak is independent of contact size. (b) The critical frequency corresponding to the poroelastic peak inversely scales with contact radius squared.

The critical frequency corresponding to the peaks of phase lag resulting from viscoelasticity will not change when the contact radius changes, because viscoelastic time is a characteristic value of the material and independent of contact radius. On the other hand, the critical frequency corresponding to the peaks resulting from poroelasticity will

scale inversely with the square of the contact radius (Figure 2.8). Using two or more different depths of indentation, the two effects can be clearly differentiated. This multi-depth method will work for spherical indenter and conical indenter, for which the contact radius changes when the depth changes. For cylindrical punch, data have to be collected from several cylinders of different radii, because the contact radius does not change for the same cylindrical indenter when the depth of indentation is changed. At a certain range of contact radii, the viscoelastic peak and poroelastic peak may be coupled and hardly differentiated. To extract the coupled viscoelastic and poroelastic properties of the materials is beyond the scope of this work. However, since the poroelastic time scales with contact radius squared while the viscoelastic time is independent of length, it is always possible to single out the poroelastic characters of the material by using an appropriate size of indentation.

In previous literature, some size-dependent bulk properties of materials have been reported^{108,109}, which were obtained using the indentation technique. Indentation depth-dependent bulk properties were also reported in polymeric materials¹¹⁰. These polymeric materials do not contain solvent molecules, and the intrinsic cause for the depth-dependent properties is believed to be the nonlinear interaction between the molecules on the polymer chains. Hydrogels, not only the specific ones studied in this dissertation, contain a large amount of solvent, so that direct molecular interaction between polymer chains is unlikely to happen. The elasticity of hydrogels has been attributed to the entropy of polymer chains' deformation, the entropy and the enthalpy of mixing polymer and solvent molecules¹¹¹⁻¹¹⁴, so the direct molecular interaction is considered to have a negligible influence on the elastic response of the hydrogels, especially under shallow indentation. Therefore, it is still

expected that poroelasticity is the only length-dependent factor for the bulk response of hydrogels in the indentation tests.

2.4 Experiments

In order to demonstrate and verify the experimental procedure, oscillation indentation tests were carried out on polyacrylamide (PAAm) gel by atomic force microscopy. To prepare the stock solution, 250 μL of 40% (w/w) acrylamide solution, 150 μL of 2% (w/w) *N,N'*-Methylenebis(acrylamide) (bis-acrylamide) solution and 600 μL of deionized water were mixed. Then 5 μL of 10% (w/w) ammonium persulfate solution and 0.5 μL of *N,N,N',N'*-tetramethylethylenediamine (TEMED) were added as initiators. The mixed solution was cured in the 1 mm thick space between two parallel glass slides for 30 minutes. The synthesized gel was later submerged in deionized water for 24 hours to swell before the indentation measurements.

The oscillation indentation tests were conducted using the indentation function of the atomic force microscope (Asylum Research MFP-3D AFM). The tips (Novascan) with polystyrene probe of 25 μm diameter and cantilever of spring constant 0.58 N/m were used. Three groups of measurements were taken with indentation depth of 200 nm, 350 nm and 600 nm respectively. The actuation frequency was taken from 0.4 Hz to 32 Hz, and for each frequency value, the oscillation lasted for at least 20 cycles. The indentation depth and reaction force were recorded overtime at a sampling rate from 0.82 kHz to 1.92 kHz to ensure enough data for each cycle. The phase lag was calculated according to equation (2-10).

Figure 2.9(a) illustrates the experimental results of indentation depth and force for one frequency. Figure 2.9(b) plots force versus displacement for one cycle of loading and unloading. The ellipse-shaped curve in Figure 2.9(b) indicates that energy dissipation exists during the oscillation indentation test. Slight drift in the force measurement is observed, which could be due to thermal drift of the AFM system, or the feedback control loop for generating displacement-controlled loading. However, the oscillation frequency range was selected so that the amount of drift is small compared with the oscillation amplitude of the measured force. Multiple tests were performed which showed consistent results of phase lag against actuation frequencies measured at different times, despite the slight drift in the reaction force.

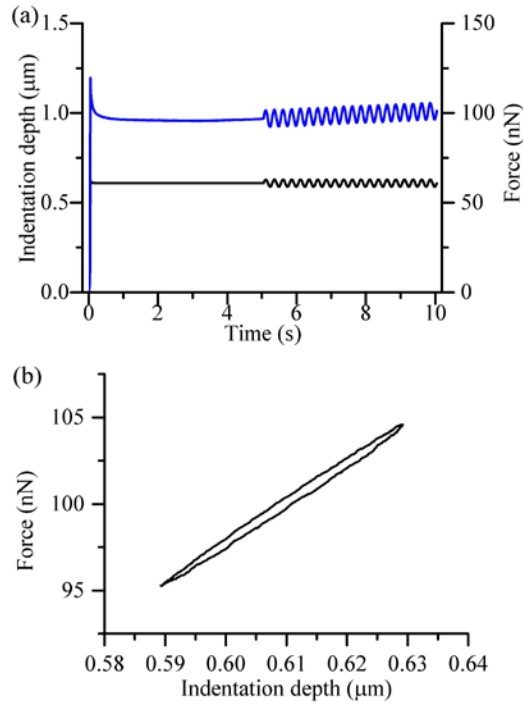


Figure 2.9 Experimental results of oscillation indentation on PAAm gel under one oscillation frequency using the atomic force microscope. (a) Indentation depth (black line) and indenting force (blue line) are recorded as functions of time. (b) The force-displacement curve recorded during one cycle of loading and unloading.

In Figure 2.10(a), the phase lag is plotted against the actuation angular frequency. The error bar for each data point represents the standard deviation of measurements from the multiple cycles at the same actuation frequency, and the dashed lines are fitting curves that assist in locating the phase lag peak. For each indentation depth, a single peak is observed within the frequency spectrum, while the corresponding angular frequencies clearly differ for different indentation depths. When the angular frequency is timed with the contact radius squared, ωa^2 , the three curves collapse into one single curve (Figure 2.10(b)), which confirms the poroelastic-dominant behavior of the sample. Following the

procedure in the theoretical results section, the poroelastic properties of the PAAM gel can be calculated.

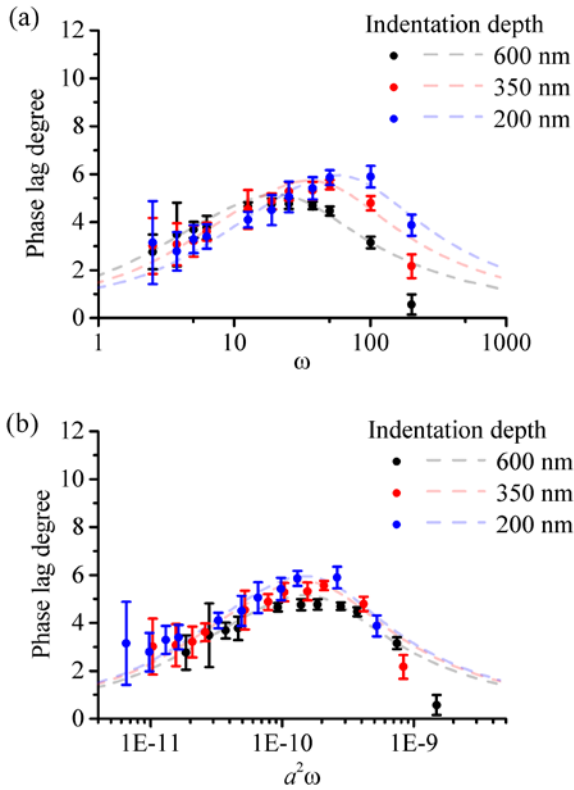


Figure 2.10 Experimental results of dynamic indentation on PAAM gel under a wide range of actuation frequencies. (a) Phase lag degree is plotted against the angular frequency for three different depths of indentations. (b) Phase lag degree is plotted against the product of angular frequency and contact radius squared for the three depths of indentations.

From Figure 2.10(a), the critical phase lag Δ_c and the corresponding critical actuation frequency ω_c were extracted separately from the three measurements for statistics analysis. Substituting Δ_c into Equation (2-19) gives the Poisson's ratio $\nu=0.32\pm 0.02$. Substituting

the extracted value of Poisson's ratio into Equation (2-20) gives the critical normalized angular frequency $\Omega_c=2.4\pm0.04$. The diffusivity can then be calculated from $D = a^2\omega_c/\Omega_c$ with $a^2 = Rh_0$, which gives $D=(6.7\pm0.8)\times10^{-11}$ m²/s. Substituting the relaxed force from the measurement to the classical elastic solution $G = 3(1-\nu)F(\infty)/8h_0a$, the value of the shear modulus can be obtained as $G=16.0\pm1.0$ kPa. These results are in the range of data previously reported for polyacrylamide gels^{71,77,95,96}.

It is noted that the bulk properties of the polyacrylamide hydrogels made for studies in this dissertation are in general repeatable, but with a slight difference across batches made at different times. Therefore, for each research purpose in each chapter, the hydrogels are prepared using the same batch of chemicals at the same time to reduce the possible factors causing the difference in forming the polymeric network. Another factor that may introduce error into the measurements is the calibration of the AFM probes. For all the studies in this dissertation, the thermal method was used for calibrating the spring constant of the AFM probes, which may introduce an error on the scale of 10% for the final force measurement. Multiple instruments of the atomic force microscope were used to complete studies in this dissertation, but they are from the same series of models (Asylum MFP-3D series). For each research purpose in each chapter, only one instrument was used. However, no systematic difference was observed from different instruments when using the same composition of hydrogels and the same type of AFM probes.

2.5 Conclusion

The poroelastic oscillation indentation method for spherical indenter, cylindrical punch and conical indenter is developed. The boundary value problem is solved both analytically and numerically. The results are in good agreement. A unified solution is obtained for the three different shapes of indenters. The phase lag between force and displacement spectra is proved to depend on only two variables: the Poisson's ratio of the material and the normalized actuation frequency. Remarkably simple forms are derived for the relationship between the Poisson's ratio and a critical phase lag, and the relationship between the critical normalized angular frequency and the Poisson's ratio, which can be easily used to extract material properties from experimental data. In the experiment, only two values are needed to be recorded: the peak value of the phase lag and the corresponding frequency. A multi-depth indentation method is also provided to simply differentiate the poroelastic behaviors from viscoelastic behaviors in gels. A group of oscillation indentation measurements was carried out on polyacrylamide gel using atomic force microscopy and confirmed the applicability of the method. The oscillation indentation method developed in this study has great potential to become a reliable and routine technique for characterizing the poroelasticity of biological tissues at a small scale.

CHAPTER 3. PROBING THE SWELLING-DEPENDENT MECHANICAL AND TRANSPORT PROPERTIES OF POLYACRYLAMIDE HYDROGELS

3.1 Introduction

The linear poroelasticity theory is phenomenological. Meanwhile, there have been several notable attempts to formulate a more physics-based theory for gels,^{70,115–120} in which the nonequilibrium thermodynamics frame^{121–124} has been formulated, leaving open the free-energy function and the kinetic laws, both of which are material specific. The thermodynamic part of the theory follows that of Flory and Rehner.^{111–114} The crosslink density of the network is described by the parameter N (number of chains per unit volume of dry polymers), and the mixing behavior by the Flory-Huggins parameter χ (enthalpy of mixing). In the kinetic part, the flux was modeled as linearly proportional to the gradient of chemical potential with a constant diffusion coefficient D .^{70,115–120,125} However, since most hydrogels can absorb a large amount of solvent and the solvent concentration in the hydrogels changes dramatically as they evolve from dry to swollen states, the widely used assumption of constant N , χ and D is questionable. It is also believed to be one of the main reasons for that the models calibrated by one set of experiments often cannot predict the behaviors of the same hydrogel under different loading conditions.^{70,116} Additionally, evidence has been seen in polymer solutions that both χ and D have a strong dependence on solvent concentration due to a concentration dependence of chain mobility, solvent mobility and polymer-solvent interactions.^{126–132}

The parameters' dependence on solvent concentration (or equivalently the swelling ratio) of crosslinked hydrogels has rarely been studied, but this topic is not trivial. First, the setup of the thermodynamic framework adopts a nonlinear description of the material deformation, therefore intrinsically convenient to be applied to cases of large strain deformation. Meanwhile, the thermodynamics model framework adopting the Flory-Rehner model has been served as a common start point for developing models for novel hydrogels with more components or multiple fields¹¹⁹. Therefore, developing an approach to examining the dependence of the thermodynamic and kinetic parameters on solvent concentration would be beneficial for a series of future applications of hydrogels.

In this chapter, the assumptions that parameters N , χ and D being constants are examined using the following approach. First, the linear poroelastic parameters of the hydrogels are measured at different swelling ratios using the dynamic indentation method developed in Chapter 2. Links are built between the linear poroelastic properties and the parameters N , χ and D by conducting linear perturbation of the free energy in the thermodynamics framework at a specific swelling ratio, and comparing it with the energy expression in the theory of linear poroelasticity. The parameters N , χ are then calculated from these linear poroelastic parameters and tentatively plotted against the swelling ratio. The results suggest that the commonly used assumption of constant N , χ and D for the same hydrogel in any swollen state is not valid. Further, all three parameters depend on the solvent concentration. In order to further study this observation, several assumptions of the polymer network and polymer-solvent interactions are suggested, and possible modifications to the Flory-Rehner model are suggested and evaluated.

3.2 Experiments

One composition of the polyacrylamide (PAAm) hydrogel was first prepared to study its swelling-dependent mechanical and transport properties. The stock solution of acrylamide (mass concentration 40%) and *N,N'*-Methylenebis(acrylamide) (mass concentration 2%) were mixed and further diluted by mixing with deionized water in the volume ratio of 3:3:14. The later steps of preparing the hydrogel sample follow the method described in Chapter 2. To reach different swelling ratios, the samples prepared with the same composition as described above were submerged into the high molecular weight polyethylene glycol (PEG) solutions of different concentrations. Four concentrations of the PEG solutions were prepared with mass fractions of 4.8%, 9.1%, 13.0%, and 16.7% respectively. Two groups of the hydrogel samples were submerged into each solution. One group was for swelling ratio measurement, and the other was for dynamic indentation measurement using the atomic force microscope. The volume of the PEG solution of each concentration was no less than 30 mL to ensure that the amount of water in the hydrogel samples had a negligible effect on the concentration of the PEG solutions. The hydrogel samples were kept in the solutions for two days before testing to ensure that an equilibrium swelling state had been reached. The containers for the PEG solutions with PAAm samples were sealed before the experiments to avoid water evaporation.

In order to quantify the swelling ratio of the PAAm samples, the mass of each swollen PAAm sample and the mass of its dry polymer network were measured. First, the hydrogel samples were taken out of the PEG solution and weighed by a digital balance as the mass of the hydrogel. A tissue was gently applied on the gel surface to absorb the extra solution before weighing. The samples were then separately put into wells of a culture

multiwall plate and lyophilized for two days. The mass of each sample was then measured by the digital balance again as the mass of the polymer network. The mass of the hydrogel at each swollen state is denoted as m_{hydrogel} , and its weight after dried is denoted as m_{polymer} . With the known polymer density $\rho_{\text{polymer}}=1.443 \text{ g/cm}^3$,¹³³ and water density $\rho_{\text{water}}=1.000 \text{ g/cm}^3$, the linear swelling ratio of the gel can be obtained as

$$\lambda_{\text{SR}} = \left(1 + \left(\frac{m_{\text{hydrogel}}}{m_{\text{polymer}}} - 1 \right) \cdot \frac{\rho_{\text{polymer}}}{\rho_{\text{water}}} \right)^{1/3}. \quad (3-1)$$

Figure 3.1(b) plots the linear swelling ratio of the PAAm hydrogel λ_{SR} as a function of the mass fraction of the external PEG solution. Its swelling ratio is around 2.8 in water and decreases as the mass fraction of PEG increases.

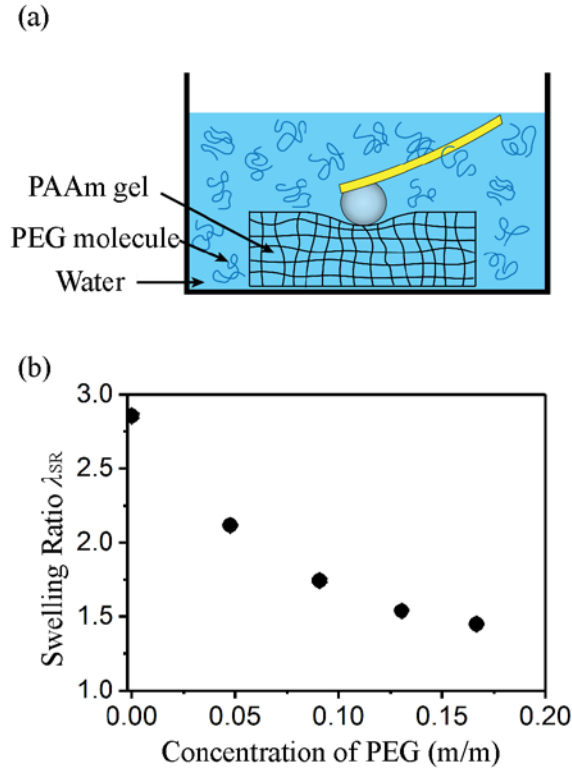


Figure 3.1 Mechanical characterization of gels in different swelling ratios. (a) Indentation of gels using AFM. (b) The swelling ratio of the PAAm gel against the concentration of the external PEG solution.

The linear mechanical and transport properties of the PAAm hydrogels at each swollen state were measured using the dynamic oscillation indentation method developed in Chapter 2 with an atomic force microscope. A schematic of the test is shown in Figure 3.1(a). Throughout the dynamic indentation test, the sample was submerged in the PEG solution with the same concentration for deswelling during preparation. Enough amount of PEG solution is added into the petri dish so that the evaporated water from the solution is negligible during the test. The AFM tips used in the experiments are made of polystyrene spheres with diameters of 4.5 μm or 25 μm , and the cantilevers have spring constant

ranging from 0.35 N/m to 1.00 N/m (Novascan). The applied displacement – time function is illustrated in Figure 3.2(a). For the dynamic indentation tests in the current chapter, a slight change is made in the oscillation part. To expedite the experiments and data processing, a sweeping frequency actuation is adopted: the frequency sweeps from 0.2 to 40 Hz continuously while maintaining the same oscillation amplitude. To check the validity of the sweeping frequency method, dynamic indentation measurement with constant frequency is also carried out on a piece of PAAm sample submerged in water. Figure 3.4 shows the results of the phase lag degree over oscillation cycles at the indentation depth of 500 nm for three fixed actuation frequencies, 0.6 Hz, 3.0 Hz, and 32.0 Hz, representing low, medium and high frequencies in the testing range. The phase lag degree for all three frequencies at the first cycle of oscillation is consistent with the values from subsequent cycles, and the phase lag values obtained from the constant frequency tests agree with those from the sweeping frequency tests at the equivalent frequencies. The dynamic oscillation tests are carried out on several different spots on multiple hydrogel samples to ensure statistical significance. On each sample, four different sizes of indentation are carried out, with the size of the contact area spanning two orders of magnitudes. The results on phase lag as functions of actuation frequencies for the gel swollen in water and various PEG solutions are shown in Figure 3.2 and Figure 3.3.

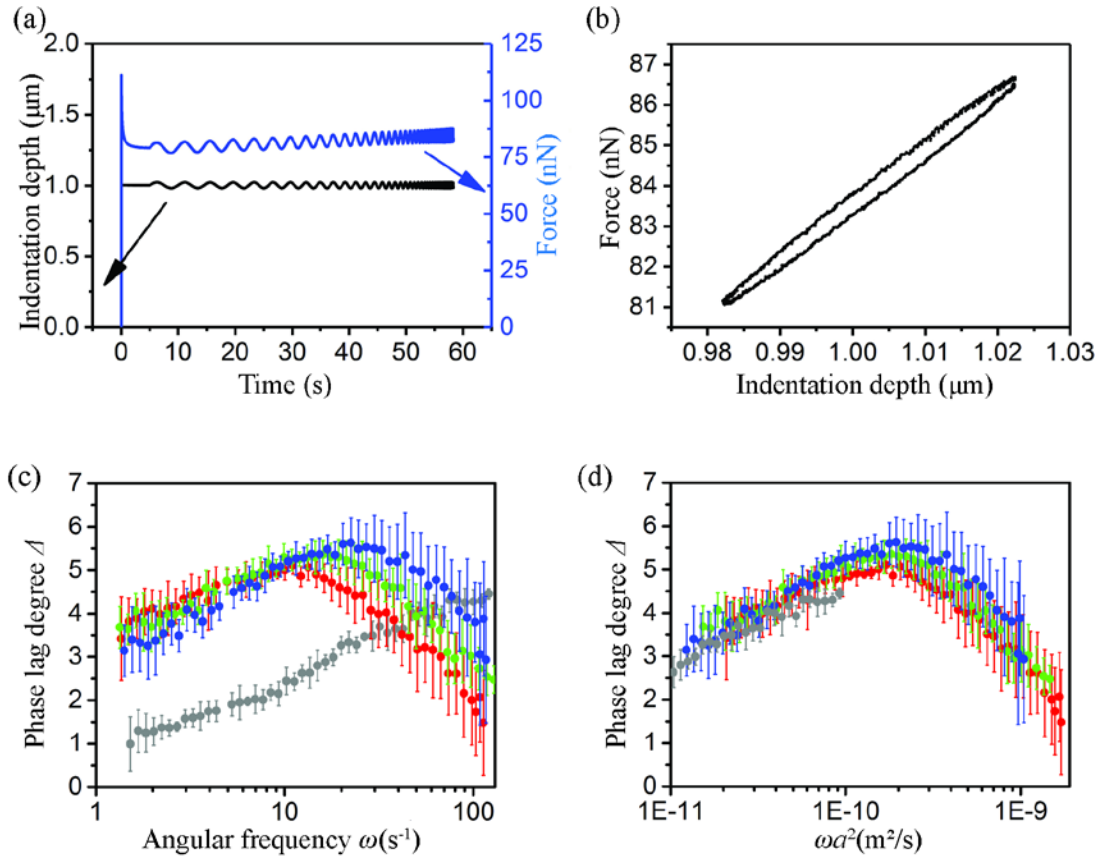


Figure 3.2 Dynamic indentation of PAAm gels swollen in pure water: (a) the displacement and force spectrums, (b) force response in one oscillation cycle at 1.22 Hz, (c) phase lag degree versus actuation angular frequency, (d) phase lag degree versus angular frequency times contact radius squared. The sphere radius and the indentation depth for each group of data are: red: $R=12.5 \mu\text{m}$, $h_0=1.0 \mu\text{m}$, green: $R=12.5 \mu\text{m}$, $h_0=0.5 \mu\text{m}$, blue: $R=12.5 \mu\text{m}$, $h_0=0.25 \mu\text{m}$, grey: $R=2.25 \mu\text{m}$, $h_0=0.25 \mu\text{m}$.

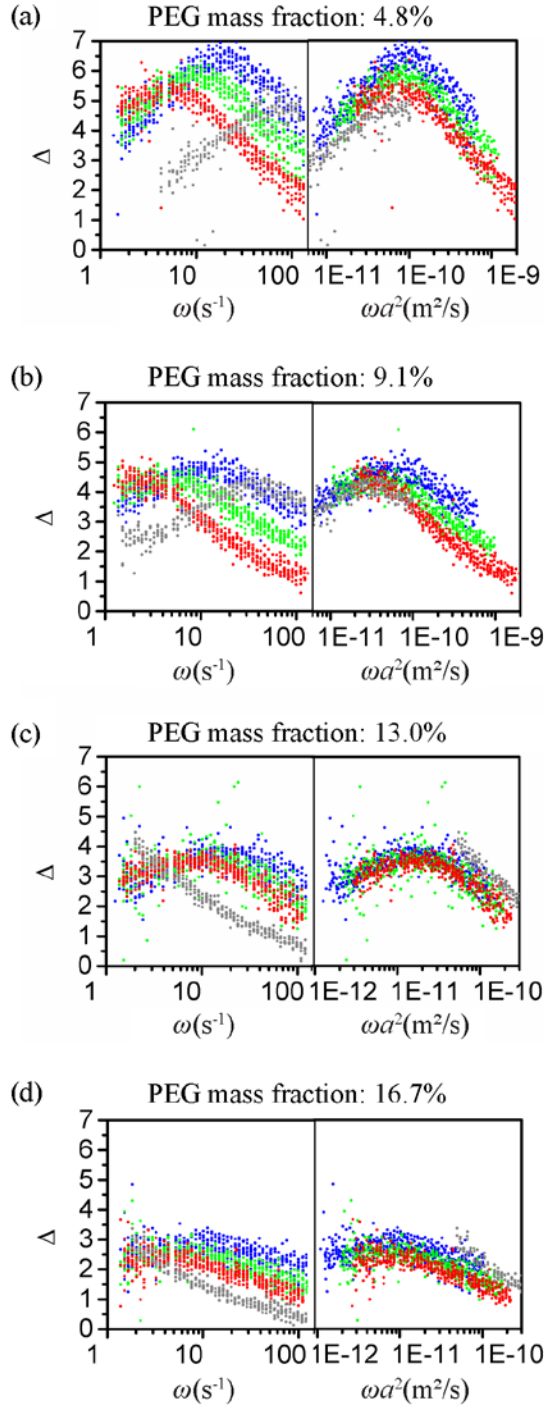


Figure 3.3 Dynamic indentation of PAAm gels in PEG solutions of different concentrations. Sphere size and indentation depth for (a) and (b) are: Blue: $R=12.5\ \mu\text{m}$, $h_0=0.25\ \mu\text{m}$; Green: $R=12.5\ \mu\text{m}$, $h_0=0.5\ \mu\text{m}$; Red: $R=12.5\ \mu\text{m}$, $h_0=1.0\ \mu\text{m}$; Grey: $R=2.25\ \mu\text{m}$, $h_0=0.25\ \mu\text{m}$. Sphere size and indentation depth for (c) and (d) are: Blue: $R=2.25\ \mu\text{m}$, $h_0=0.25\ \mu\text{m}$; Green: $R=2.25\ \mu\text{m}$, $h_0=0.5\ \mu\text{m}$; Red: $R=2.25\ \mu\text{m}$, $h_0=0.75\ \mu\text{m}$; Grey: $R=12.5\ \mu\text{m}$, $h_0=2.0\ \mu\text{m}$.

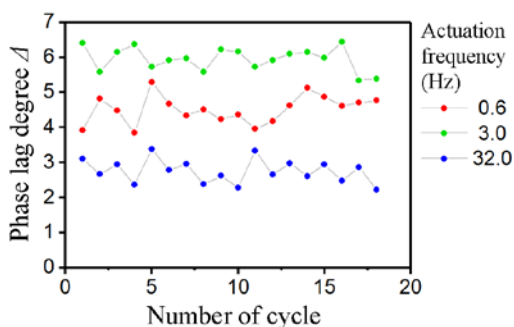


Figure 3.4 The phase lag degree measured in the dynamic indentation tests at three individual frequencies. The PAAm gel was swollen in water, and the indentation depth was around 500 nm.

To examine the possible adhesion between the tip and the PAAm hydrogel, an indenting-and-retracting test using the same tip was carried out on the hydrogel sample. The test is conducted on a PAAm hydrogel in water. In the loading process, the indenting speed is set to be 50 nm/s, which is slow enough to ensure that the solvent in the hydrogel is equilibrated with the environment at all time. As is shown in Figure 3.5, the force-displacement curve obtained during the loading process fits very well with Hertzian model prediction, indicating very little to no adhesion. Following the loading, the tip is retracted at the same speed. The force-displacement curve obtained during the retraction process overlaps with the loading curve for the most part (Figure 3.5), except when the AFM probe is close to leave the hydrogel surface, and a nonzero pull-off force is observed. This observation of zero adhesion during approaching but nonzero pullout force during separation has also been observed before in the literature of the nanoindentation of soft materials.^{100,134} The most possible reason is that for neutral hydrogels such as PAAm gels, the long-range interaction between the polymer chains and the sphere that could contribute

to the enlarged contact area is largely screened by water. As a result, in the experiment, no jump-to-contact was observed during the approaching process. Only short-range interaction is developed which only happens after the indenter is pressed into the sample. The short-range interaction does not induce the change of contact area but is responsible for the pull-out force after the indenter is retracted to leave the sample surface. In other words, the Hertzian contact model applies as long as the indenter does not retract. In the proposed dynamic oscillation, a deep indent ($h=0.25, 0.5, 1, 2\mu\text{m}$) is followed by a small amplitude oscillation ($\delta h=20\text{ nm}$), so the indenter is always in compression with the sample and the change of contact radius during oscillation is small enough to be neglected. Consequently, since it is the information in the oscillation stage that is used to extract the poroelastic properties, the effect of adhesion between the spherical indenter and the hydrogel surface can be neglected. In fact, the possible short-range adhesion between the very tip of the indenter and the sample may further stabilize the contact area to be a constant during oscillation.^{135,136} This effect supports the treatment of constant contact radius in the current method for the extraction of poroelastic properties. A more systematic study on hydrogel adhesion in indentation tests is carried out in Chapter 4, which also supports the above argument.

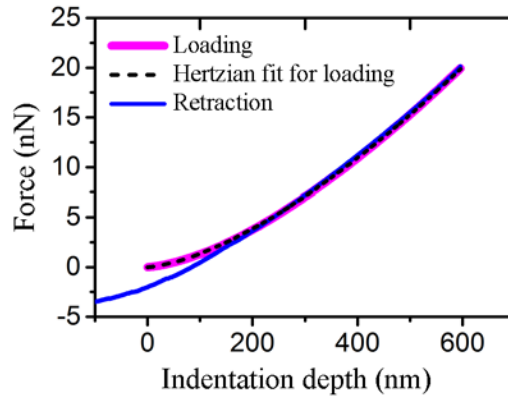


Figure 3.5 Loading and unloading curve from the AFM indentation test with a speed of 50 nm/s. The Hertzian model fits well to the loading curve and most of the unloading curve.

3.3 Results and Discussion

Figure 3.2 shows one set of measurements on the PAAm hydrogel swollen in pure water. The black and blue lines show the applied displacement and measured force spectrum respectively (Figure 3.2(a)). Energy is dissipated through each cycle of loading and unloading (Figure 3.2(b)), which is used to calculate the phase lag value. The phase lag degree Δ is plotted as a function of angular frequency ω in Figure 3.2(c), the error bars representing the standard deviation of results from multiple points on multiple samples. The red, green and blue lines are acquired from dynamic indentation using the sphere of radius 12.5 μm and indentation depth of 1, 0.5 and 0.25 μm , respectively. The curve shifts to the left as the indentation depth increases. When the angular frequency is normalized by the contact radius squared as ωa^2 , the three groups of data overlap each other (Figure 3.2(d)), which indicates that the time-dependent behavior of the swollen hydrogel is dominated by the flow of solvent.¹³⁷ These length scales are chosen because only in these

length scales that the entire peak of the curve can be captured within the testing frequencies (0.1-100Hz) feasible for AFM. To convey the poroelasticity-dominant effect with more convincing evidence, the probe length scale was further expanded by using a sphere of 2.25 μm radius and depth of indentation of 0.25 μm . The curve is shown as the grey line in Figure 3.2(c) and Figure 3.2(d). Under this length scale, the peak of the curve falls out of the measurable frequency range of commercial AFM. Although the additional curve does not capture the complete up-and-down of the phase lag over measured frequencies, they show an obvious shift of characteristic time from the previous phase lag data (Figure 3.2(c)). This length-dependent characteristic time is a signature of the poroelastic effect. It is further shown in Figure 3.2(d) that when all the curves are plotted against the normalized actuation frequency, they collapse much better. If it is a viscoelasticity-dominant effect, the curves should collapse in the phase-lag against the frequency plot without normalization because viscoelastic time is independent of any macroscopic length. With the complete data sets across two orders of magnitudes in terms of contact area, it is convincing that the time-dependent response here is dominated by the poroelastic effect.

Similar results are obtained for dynamic indentation of PAAm hydrogels in PEG solutions of 4.8%, 9.1%, 13% and 16.7% concentrations. Again, to capture the whole peak of phase lag, the sphere of 12.5 μm was used on the gels in 4.8% and 9.1% PEG solutions first and sphere of 2.25 μm on the gel in 13.0% and 16.7% PEG solutions. Three depths of indentation are carried out for each case. The results are shown in Figure 3.3 as the red, green and blue dots. The probe length scale for all the tests is also expanded in order to convey the poroelasticity-dominant effect with more convincing evidence. Specifically, data were added from 2.25 μm radius sphere on the gel in the 4.8% and 9.1% PEG solutions

and 12.5 μm radius sphere on the gel in 13.0% and 16.7% PEG solutions. The results are shown as the grey dots in Figure 3.3. For all the experiments, the curves of the phase lag degree are separated when plotted as functions of actuation frequency, and they overlap each other when plotted as functions of normalized angular frequency.

At higher frequencies, there is a slight deviation from a complete overlap of the phase lag curves when plotted against the normalized angular frequency. One possible reason is due to the hydrodynamic force on the AFM probe, the magnitude of which scales with the radius of the sphere and increases as the moving speed and the viscosity of the fluid.¹³⁸. Another possible factor is the viscoelastic effect of the hydrogel, which is independent of any macroscopic length scale. Since the literature reported viscoelastic relaxation time of PAAm gel is around 0.01s¹³⁹, the viscoelastic effect may emerge at higher frequencies (>60 Hz). Despite these factors, as the testing length scale changes one order of magnitude (4.5 μm to 25 μm sphere), the results from all the experiments in general collapse much better in the plot against normalized angular frequency comparing with the plot without normalization. Therefore, the conclusion can be drawn with confidence that the measured time-dependent responses here are dominated by poroelastic effects, and the steps developed in Chapter 2 are used here to extract the linear poroelastic parameters of the hydrogel sample at all the swelling ratios.

Figure 3.6 shows the result of the shear modulus G , Poisson's ratio ν and diffusivity D as functions of swelling ratio λ_{SR} with the error bars being the standard deviation from nine tests. Both the shear modulus and the Poisson's ratio decreases as the swelling ratio increases. Meanwhile, the diffusivity of the gel increases two orders of magnitude from the scale of 10^{-12} m^2/s to 10^{-10} m^2/s as its swelling ratio only changes two times from 1.4 to 2.8.

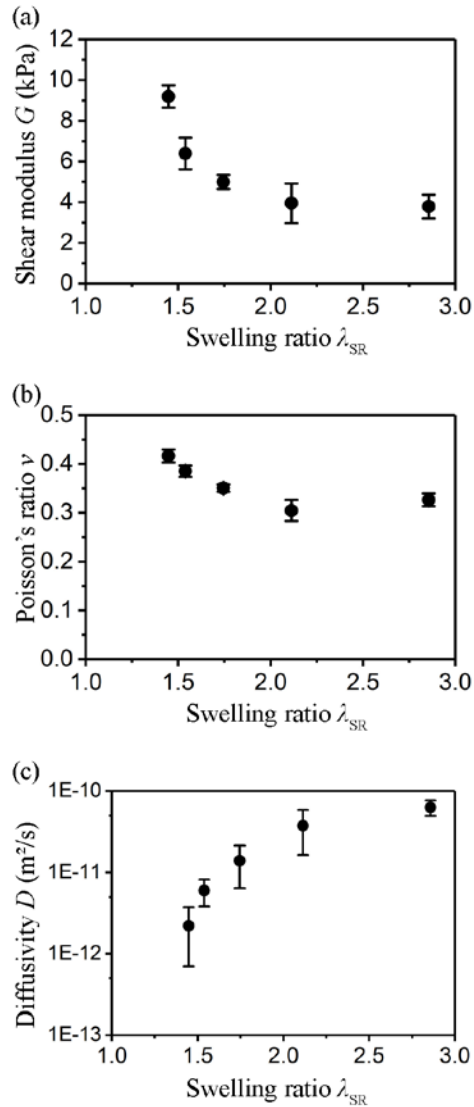


Figure 3.6 Linear poroelastic properties of the PAAm gels: (a) shear modulus, (b) Poisson's ratio, and (c) diffusivity against swelling ratios.

The nonlinear model that is supposed to describe the behaviors of gels all the way from dry to swollen states has been derived based on the Flory-Rehner theory,^{111,112,114,140,141} according to which the free energy of a gel is a summation of the stretching energy and mixing energy,

$$W = \frac{1}{2} N k_B T \{ \text{Tr}(\mathbf{F}^T \mathbf{F}) - 3 - \ln[\det(\mathbf{F})] \} - \frac{k_B T}{V_0} \left(V_0 C \ln \left(1 + \frac{1}{V_0 C} \right) + \frac{\chi}{1 + V_0 C} \right), \quad (3-2)$$

where $\mathbf{F}_{iK} = \partial x_i / \partial X_K$ is the deformation gradient with \mathbf{X} being the reference coordinates and $\mathbf{x}(\mathbf{X}, t)$ the current coordinates, N the number of polymer chains per unit volume of the dry polymer, k_B the Boltzmann constant, T the temperature, V_0 the volume of a solvent molecule, C the number of solvent molecules per unit volume of the dry polymer, and χ the Flory-Huggins interaction parameter. Assuming the individual polymer chains and solvent molecules are incompressible, there is $1 + V_0 C = \det(\mathbf{F})$.^{70,104,105} Here the stretching energy follows the incompressible Neo-Hookean model, in which the deformation of each polymer chain follows Gaussian statistics and the total free energy is the summation of the stretching energy of all the polymer chains. The mixing energy was derived by Flory and Huggins based on the similar statistics for binary solutions.¹¹²

Hydrogels can absorb a large amount of solvent and have huge volume change. The model in equation (3-2) has been used to describe the large deformation of gels evolving from the dry to swollen states. However, indentation is induced at a particular swollen state of the gel. The deformation induced by indentation is small. Therefore, the deformation of the gel under indentation at a particular swollen state can be modeled by linear poroelasticity. However, the linear poroelasticity only works for the gel's behavior in the vicinity of this particular swollen state, but would not work for the whole large volume change of the gel. The poroelastic properties measured at these particular swollen states of gels can be viewed as the incremental properties of the gels at each swollen state. Next, the mechanical and transport properties of a model hydrogel under different swelling ratios are

used to examine the applicability of the large deformation model based on the Flory-Rehner theory for a large range of deformations of the hydrogel.

To link the measured linear poroelastic properties of the gels to their thermodynamic properties in the nonlinear model, the nonlinear theory around a particular swollen state of the gel $\lambda_{SR} = \sqrt[3]{1 + CV_0}$ is linearized, and it is compared with linear poroelasticity, the free energy of which is expressed as

$$w = G \left[\varepsilon_{ij} \varepsilon_{ij} + \frac{\nu}{1 - 2\nu} (\varepsilon_{kk})^2 \right]. \quad (3-3)$$

The comparison leads to the following relations linking the shear modulus and Poisson's ratio to the thermodynamic parameters N and χ for this particular swelling ratio, λ_{SR} as:

$$\frac{Nk_B T}{2} \left(\frac{1}{\lambda_{SR}} + \frac{1}{\lambda_{SR}^3} \right) + \frac{k_B T}{2V_0} \left[\ln \left(\frac{\lambda_{SR}^3}{\lambda_{SR}^3 - 1} \right) - \frac{1}{\lambda_{SR}^3} - \frac{\chi}{\lambda_{SR}^6} \right] = G, \quad (3-4)$$

$$\frac{\lambda_{SR}^6 - \chi(\lambda_{SR}^3 - 1) - \lambda_{SR}^6(\lambda_{SR}^3 - 1) \ln \left(\frac{\lambda_{SR}^3}{\lambda_{SR}^3 - 1} \right)}{(\lambda_{SR}^3 - 1) \left[-\chi - \lambda_{SR}^3 + NV_0 \lambda_{SR}^3 (\lambda_{SR}^2 + 1) + \lambda_{SR}^6 \ln \left(\frac{\lambda_{SR}^3}{\lambda_{SR}^3 - 1} \right) \right]} = \frac{\nu}{1 - 2\nu}. \quad (3-5)$$

According to Equation (3-4), the shear modulus of the hydrogel at a particular swelling ratio is not only related to the stretching state of the polymer network (the first term in equation (3-4) with N) but also the mixing between the polymer network and the solvent (the second term in equation (3-4) with χ). This dual contribution from both

stretching and mixing to the gels' resistance to deformation may lead to an unexpected trend of the shear modulus of the gel as it swells or shrinks. As shown in Figure 3.6(a), the measured shear modulus of the gel decreases from 9.2 kPa to 3.9 kPa as the gel swells from 1.4 to 2.1 in linear swelling ratio but does not decrease much as the gel swells further from 2.1 to 2.8. According to Equation (3-4), from the swelling ratio of 2.1 to 2.8, the contribution of the polymer chains to the gel's resistance to deformation decreases while the contribution of the mixing term increases. Consequently, the hydrogels with significantly different swelling ratios have similar shear modulus.

Substituting the measured $G(\lambda_{SR})$ and $\nu(\lambda_{SR})$ of the PAAm hydrogel into Equation (3-4) and (3-5), $N(\lambda_{SR})$ and $\chi(\lambda_{SR})$ of the same gel can be calculated. As shown in Figure 3.7(a), N keeps increasing as the swelling ratio decreases, which possibly indicates that additional crosslinking mechanisms such as the entanglement of the polymers may also contribute to the effective crosslink of the hydrogel at lower swelling ratios. As shown in Figure 3.7(b), χ is close to 0.5 at the high swelling ratio, and increases as swelling ratio decreases. This result suggests that the Flory-Huggins interaction parameter χ strongly depends on the polymer concentration,^{130,132} which is a known phenomenon for polymer solutions. The result suggests that it is not just the free energy function being less than perfectly accurate or the systematic error from the experiment. If the free energy function from the Flory-Rehner model is still assumed to be correct, then the modification for N value has to change three orders of magnitude (1E24 - 1E27) and the modification of χ is from 0.9 to 0.4, which is also big.

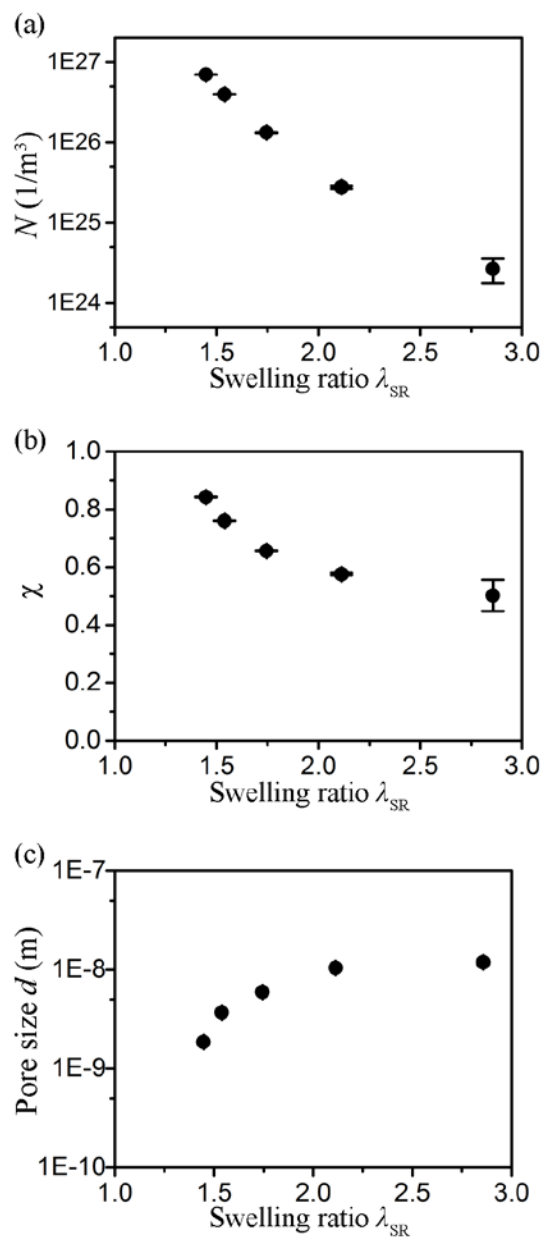


Figure 3.7 Thermodynamic properties of the PAAm gels: (a) the parameter N , (b) the Flory-Huggins interaction parameter χ , and (c) the effective pore size for solvent transport d , against swelling ratios.

The diffusivity of the solvent transporting through the network indicates a characteristic length of the polymeric network – the effective pore size. Considering the

polymeric network as a porous media, its flow kinetics can be modeled by Darcy's law⁶⁴ and the diffusivity of the solvent can be related to the permeability k of the porous skeleton as

$$k = \frac{(1 - 2\nu) D\eta}{2(1 - \nu) G}, \quad (3-6)$$

where η is the dynamic viscosity of the solvent. The permeability parameter has a unit of length squared. A micro-structural model is needed to link the permeability to the pore size. Adopting the simplest one that assumes the liquid transport pathways are in the form of a series of parallel cylindrical tubes,¹⁴² the diameter of the cylindrical tubes can be expressed as

$$d^2 = \frac{32k\tau_t^2}{\varphi}, \quad (3-7)$$

where φ is the porosity (i.e. the ratio between the pore volume to the overall volume), and τ_t the tortuosity. Assume the tortuosity depends on the porosity φ as $\tau_t = \varphi^{-\beta_t}$, where β_t is a parameter related to the pore geometry¹⁴³⁻¹⁴⁵. For the fully swollen gel, more than 95% content is water, so the tortuosity value is close to 1. When the network is dry with the porosity of 7.86%, the tortuosity is taken to be around 15 as for dry polymeric networks.¹⁴⁶ Substituting these data gives $\beta_t = 1.068$.

The magnitude of the effective pore size is plotted in Figure 3.7(c), the pore size of the hydrogel fully swollen in water is on the order of 10 nm, and the value decreases in small swelling ratio regions. In general, the result shows a nonlinear change in the pore size with respect to the swelling ratio.

3.4 Modifying the Flory-Rehner Model for Hydrogels

In the previous section, the applicability of the Flory-Rehner model on a hydrogel is examined by fixing the expression of terms in the model, while calculating the parameters N and χ as functions of the swelling ratio. The results show that both parameters change with the swelling ratio. In previous literature, it has been reported that χ may depend on the solvent concentration in polymer solutions^{130,132}. However, because N deviates significantly from being a constant, all the components in the Flory-Rehner model will be further examined for their applicability on hydrogels. In this section, several possible modifications are suggested. It is expected that in the modified model, the parameters for polymer elasticity depend on the composition but not on the swelling ratio, while the Flory-Huggins interaction parameter χ is the same for hydrogels with different compositions.

In order to better evaluate the applicability of the modified model, polyacrylamide hydrogels with four different compositions were prepared with the method introduced in the previous section. It is also expected that the measurements on more hydrogel compositions can prove that the difficulties of using the Flory-Rehner model are universal for a wider range of polyacrylamide hydrogels.

The compositions of the hydrogels are listed in Table 3.1. These compositions are chosen to cover a common range that is studied for polyacrylamide hydrogels^{52,101,147}. Following the method in the previous section, these hydrogels were maintained at different swelling ratios. The swelling ratios of gels of different compositions at each PEG mass concentration are plotted in Figure 3.8. The linear poroelastic properties of the hydrogel samples were measured using the dynamic indentation method. In the experiments, all the

hydrogel samples still exhibit the dominance of poroelasticity. The linear poroelastic parameters of the samples were extracted and shown in Figure 3.9, the error bars representing the standard deviation from the measurements on multiple points on the same sample. For all the hydrogel compositions, the values of the shear modulus and the Poisson's ratio decrease as the swelling ratio increases, while the values of diffusivity increase with the swelling ratio. The trends of the poroelastic parameters follow that in the previous subsection, which again indicates the necessity of modifying the Flory-Rehner model.

Table 3.1 Compositions of the polyacrylamide hydrogels for the study of swelling-dependent poroelastic properties.

Composition No.	Concentration of Acrylamide	Concentration of Bisacrylamide
1	10%	0.2%
2	8%	0.2%
3	6%	0.2%
4	6%	0.4%

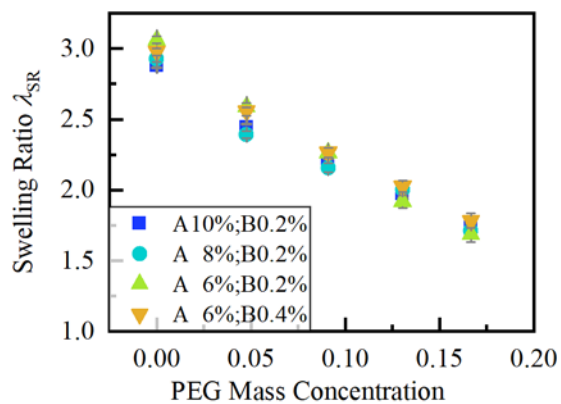


Figure 3.8 The swelling ratio of the polyacrylamide hydrogels against the mass concentration of the external PEG solution. In the legend, the letter A means the concentration of acrylamide, and the letter B means the concentration of *N,N'*-Methylenebis(acrylamide).

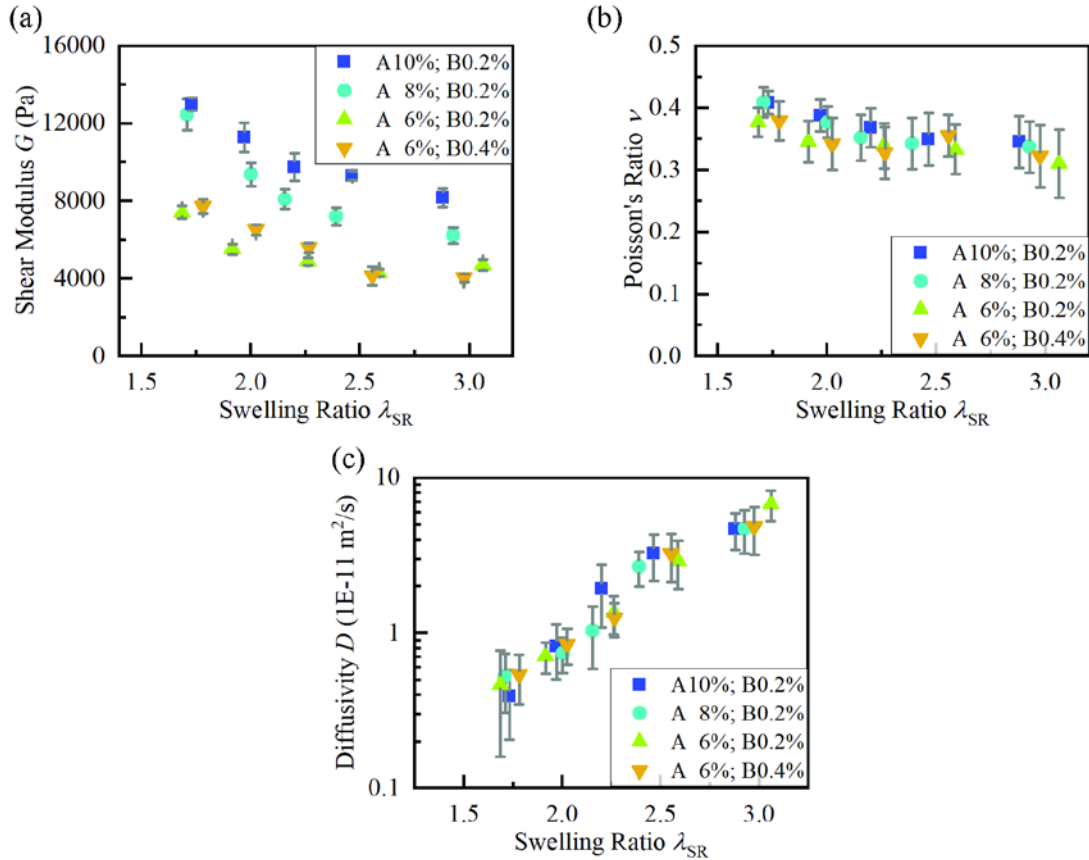


Figure 3.9 The experimental results for the four hydrogel compositions at different swelling ratios. (a) The shear modulus. (b) The Poisson's ratio. (c) The diffusivity.

In the previous section, that the calculated value of N increases significantly as the swelling ratio decreases suggests the necessity of considering polymer chain entanglement. Previously, several models have been proposed to describe the entanglement effect in the polymeric network for rubber elasticity^{63,148}. In these models, the deformation of each polymer chain is constrained by the entanglement of the surrounding polymer. The effect of this constraint is usually represented by an additional term in the expression for the free energy. Among these models, the Mooney-Rivlin model¹⁴⁹ is commonly used. It includes

a term the same as that in the Neo-Hookean model, and another term that phenomenologically describes the deviation of the real polymer network from the Neo-Hookean model. The latter term has often been related to the entanglement effect in the polymeric network¹⁴⁸. Considering that the polymer chains in hydrogels may be under similar topological constraints, the stretching energy of the hydrogel needs to be modified by replacing the term for stretching energy to the expression in the Mooney-Rivlin model.

The application of the Mooney-Rivlin model is mainly on rubber materials, and the material is usually assumed to be incompressible. There have been efforts on developing models similar to the Mooney-Rivlin model but with terms with clearer physics meaning¹⁴⁸. These models also assume material incompressibility. On the other hand, hydrogels can expand or shrink in all three directions significantly. Therefore, for each polymer chain, its surrounding environment might change more drastically, and there may be additional effects from polymer chain interactions that are not covered by the Mooney-Rivlin model. To account for the possible additional effects, another term from the Blatz-Ko model¹⁵⁰ is added into the free energy expression. For simplicity, the term has only one variable: the volume change of the hydrogel. This term is expected to capture the change of linear poroelastic properties in a larger range of swelling ratio.

Apart from the possible factors on the elasticity of polymer chains, the energy of mixing also needs modification. In the Flory-Huggins mixing model, the energy of mixing is composed of two parts, the entropy of mixing and the enthalpy of mixing. Based on a physics picture of binary mixing of molecules, both parts assume that a polymer chain can be divided into subunits with the same size of one solvent molecule, and that the bonds between the subunits can rotate completely freely in the space¹¹¹. The polyacrylamide

polymer chains have vinyl backbones, and each carbon-carbon bond in the backbones only have limited freedom of rotation. More factors may influence the estimation of the subunit size, too. For example, the amide groups on the polymer chains and the water molecules bond with the amide groups through hydrogen bonds should further increase the size of an effective subunit⁵⁶. Also, the shape of the subunit can be more complicated than a sphere, as assumed in the Flory-Huggins theory. For simplicity, in the current study, the energy of mixing is modified by increasing the volume of a subunit from V_0 to βV_0 , β being the factor indicating the number of solvent molecules that take up the volume of a polymer subunit.

Based on the above analysis, the modified model is proposed as follows,

$$\begin{aligned}
 W = & G_1(\text{Tr}(\mathbf{F}^T \mathbf{F}) - 3) + G_2(I_2 - 3) - (G_1 + 2G_2) \ln(\det(\mathbf{F})) \quad (3-8) \\
 & + K_e \{[\det(\mathbf{F})]^{-2} - 1\} \\
 & + \frac{k_B T}{\beta V_0} \left[V_0 C \log \left(\frac{V_0 C}{1 + V_0 C} \right) + \chi \frac{V_0 C}{1 + V_0 C} \right],
 \end{aligned}$$

where $I_2 = \frac{1}{2} \{[\text{Tr}(\mathbf{F}^T \mathbf{F})]^2 - \text{Tr}[(\mathbf{F}^T \mathbf{F})^2]\}$. Compared with the model in section 3.3, Equation (3-8) has additional parameters G_1 , G_2 , K_e and β . The parameters G_1 and G_2 correspond to the parameters in the Mooney-Rivlin model¹⁴⁹. The parameter G_1 is related to chemical crosslinkers present in the hydrogel. The parameter G_2 corresponds to the additional polymer chain interactions assumed in the Mooney-Rivlin model. The term with the parameter K_e is chosen from the Blatz-Ko model¹⁵⁰ to describe the additional polymer interactions not covered by the Mooney-Rivlin model. The original term of the energy of mixing is modified following the theory proposed by Flory¹¹¹, the parameter β representing the ratio of the volume of a freely-rotating subunit on the polymer chain to that of a solvent

molecule. In this modified model, because β and χ are both parameters for the energy of mixing, it is assumed that the value of these two parameters are the same for polyacrylamide hydrogels across different compositions, although χ can change with the swelling ratio. Parameters G_1 , G_2 and K_e are expected to depend on details of the polymer chain structure, thus depending on the exact hydrogel composition. The physics reason and the necessity of choosing these specific terms and parameters will be discussed after the fitting results are presented.

Following the same method of linear perturbation at a specific swelling ratio λ_{SR} , the expressions for the shear modulus and Poisson's ratio in the theory of linear poroelasticity can be written as follows. Here, the expression for the Poisson's ratio is written in a form that equals half of the Lamé's first parameter for the ease of parameter fitting.

$$G = \frac{K_e}{\lambda_{SR}^9} + \frac{G_1}{2\lambda_{SR}^3} + \frac{G_2}{\lambda_{SR}^3} + \frac{G_1}{\lambda_{SR}} - \frac{k_B T}{2\lambda_{SR}^3 \beta V_0} - \frac{k_B T \chi}{2\lambda_{SR}^6 \beta V_0} - \frac{k_B T \ln(1 - 1/\lambda_{SR}^3)}{2\beta V_0}, \quad (3-9)$$

$$G \frac{\nu}{1 - 2\nu} = \frac{2K_e}{\lambda_{SR}^9} + 2G_2 \lambda_{SR} + \frac{k_B T}{2(-1 + \lambda_{SR}^3) \beta V_0} - \frac{k_B T \chi}{2\lambda_{SR}^6 \beta V_0} + \frac{k_B T \ln(1 - 1/\lambda_{SR}^3)}{2\beta V_0}, \quad (3-10)$$

The procedure of the parameter fitting for the modified model is as follows. Because β is expected to be universal for all hydrogel compositions, all the other parameters are

first fitted by assuming β is a known parameter, with a series of values ranging from 1 to 100. This series of preliminary trials show that the value around $\beta = 20$ gives satisfying fitting results for all the hydrogel compositions, and values significantly different from $\beta = 20$ could not lead to satisfying fitting, an example will be shown later.

With a fixed value of β , the rest of the parameters are fitted. First, parameter χ is eliminated by combining equation (3-9) and equation (3-10). For each composition, the corresponding G_1 , G_2 , K_e are then fitted using the measurements of linear poroelastic parameters G , ν at different swelling ratios. Figure 3.10 plots the fitting curves of the modified models together with the experimental results of G and ν for all the hydrogel compositions. The curves from the modified model fit well to the shear modulus and the Poisson's ratio at all the swelling ratios. The fitting results for each hydrogel composition are summarized in Table 3.2.

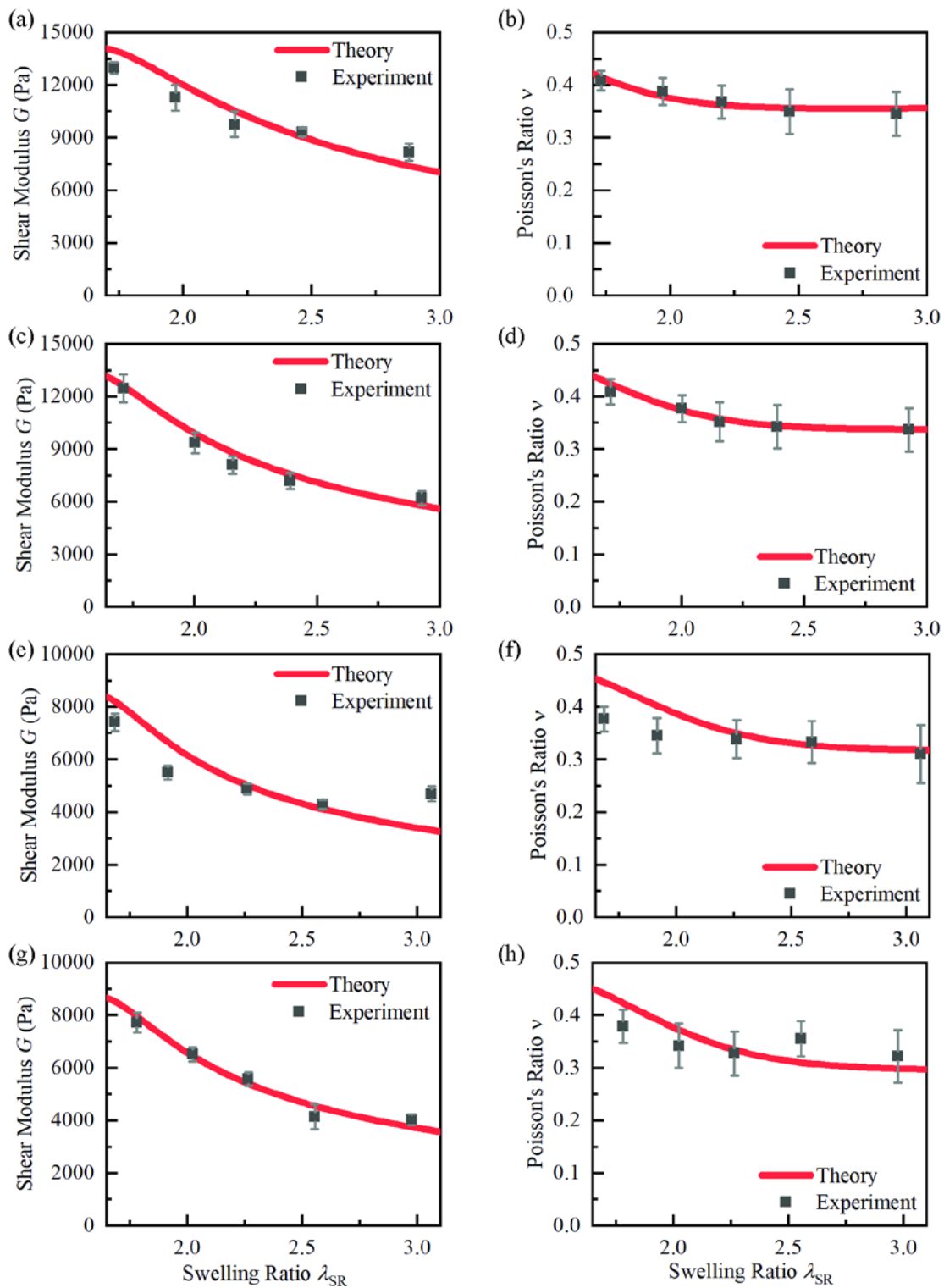


Figure 3.10 Experimental results and the fitting curves of the shear modulus and Poisson's ratio as functions of the swelling ratio. (a) (b): acrylamide 10%, bisacrylamide 0.2%. (c) (d): acrylamide 8%, bisacrylamide 0.2%. (e) (f): acrylamide 6%, bisacrylamide 0.2%. (g) (h) acrylamide 6%, bisacrylamide 0.4%.

Table 3.2 Fitting results of parameters G_1 , G_2 and K_e .

No.	Concentration of Acrylamide	Concentration of Bisacrylamide	G_1 (kPa)	G_2 (kPa)	K_e (kPa)
1	10%	0.2%	18.59	12.81	1350
2	8%	0.2%	14.99	8.53	1584
3	6%	0.2%	9.16	4.23	1624
4	6%	0.4%	10.08	3.87	1596

With the fitted values of G_1 , G_2 , K_e , the value of χ at different swelling ratios can be calculated for each composition, as plotted in Figure 3.11. Results in Figure 3.11 show that the values of χ at different swelling ratios obtained from different compositions roughly fall onto the same curve, which indicates that the fitting results agree with the assumption, that χ is uniform across different compositions. The results of χ are fitted using the Koningsveld and Kleintjens (KK) expression^{151,152}: $\chi(\lambda_{SR}) = p_a + p_c(1 - p_b)/(1 - p_b/\lambda_{SR}^3)^2$, where p_a , p_b and p_c are all parameters. The fitted values for p_a , p_b and p_c are $p_a = -3.25$, $p_b = 0.141$, $p_c = 4.34$. Most of the data points of χ fall onto this fitting curve. Only one data point of χ (the highest swelling ratio of composition No.3) deviates more from the fitting curve, which should be affected by the higher measured value of the shear stress at this specific swelling ratio (Figure 3.10). Overall, the satisfying fitting in both Figure 3.10 and Figure 3.11 indicates that the modified model can describe the swelling-dependent properties of a wider range of hydrogel compositions, and meanwhile holds two parameters (β and χ) whose values are universal across different compositions.

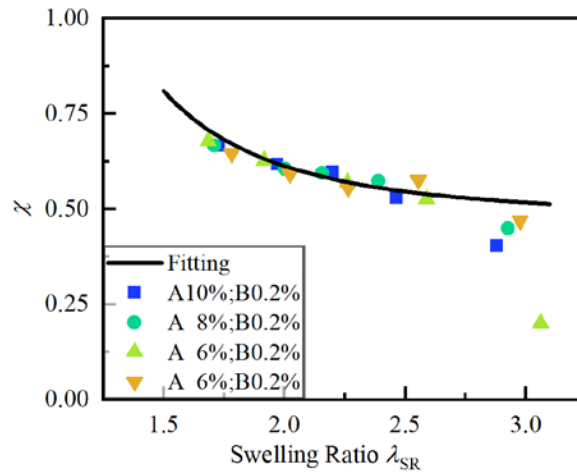


Figure 3.11 Fitting curve for the Flory-Huggins interaction parameter χ as a function of the swelling ratio.

In order to prove that all the modifications are needed to describe the swelling - dependent linear poroelastic parameters, some trials of fittings using the modified model with one term deleted are conducted. Measurements on one hydrogel composition (acrylamide concentration 8%, bisacrylamide concentration 0.2%) are used as the example. With reduced terms, it is difficult to fit both the shear modulus and the Poisson's ratio. Figure 3.12 and Figure 3.13 show the results when trying to fit at least one linear poroelastic parameter while forcing G_2 , K_e to be zero (Figure 3.12 and Figure 3.13, respectively). Figure 3.14 shows the best fitting curve when forcing β to be 1. As shown in these plots, reducing terms of modification leads to less satisfying fittings, at least for one of the linear poroelastic parameters.

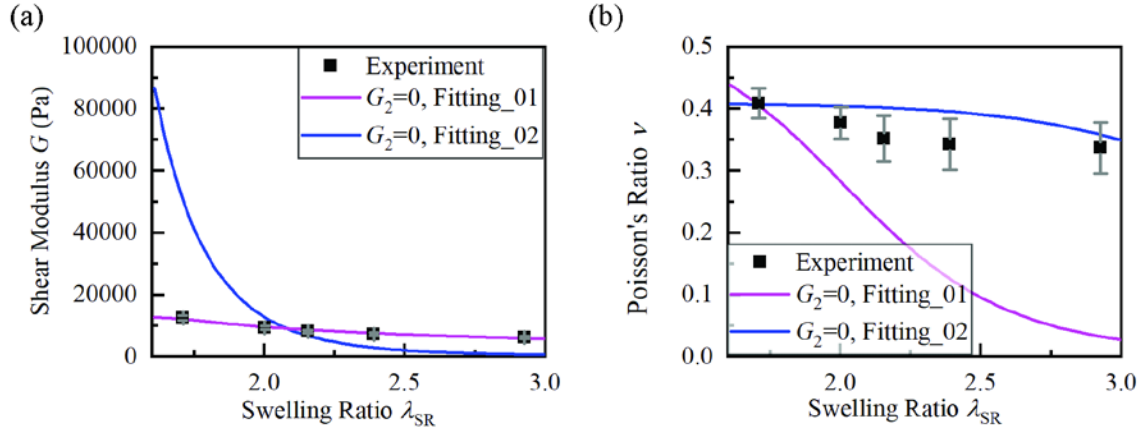


Figure 3.12 Fitting of the modified model when forcing $G_2 = 0$. (a) shows the results on the shear modulus. (b) shows the results on the Poisson's ratio. The purple curves represent a set of fitting parameters that only fits the shear modulus better ($G_1 = 1.631E4$ Pa, $K_e = 1.612E6$ Pa, $\beta = 20$). The blue curves represent another set of fitting parameters that only fit the Poisson's ratio better ($G_1 = 0.820E4$ Pa, $K_e = 6.953E6$ Pa, $\beta = 50$).

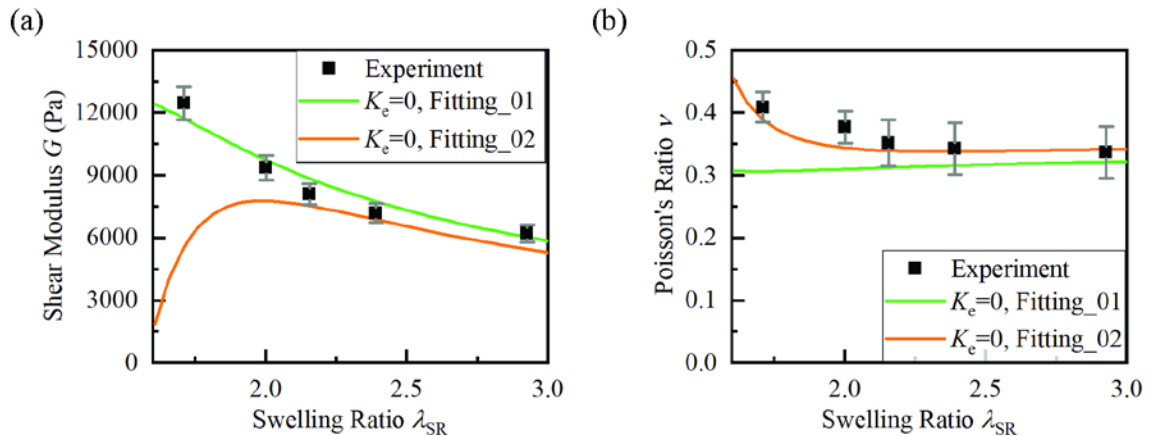


Figure 3.13 Fitting of the modified model when forcing $K_e = 0$. (a) shows the results on the shear modulus. (b) shows the results on the Poisson's ratio. The green curves represent a set of fitting parameters that only fits the shear modulus better ($G_1 = 1.582E4$ Pa, $G_2 = 0.793E4$ Pa, $\beta = 350$). The orange curves represent another set of fitting parameters that only fit the Poisson's ratio better ($G_1 = 1.419E4$ Pa, $G_2 = 0.905E4$ Pa, $\beta = 40$).

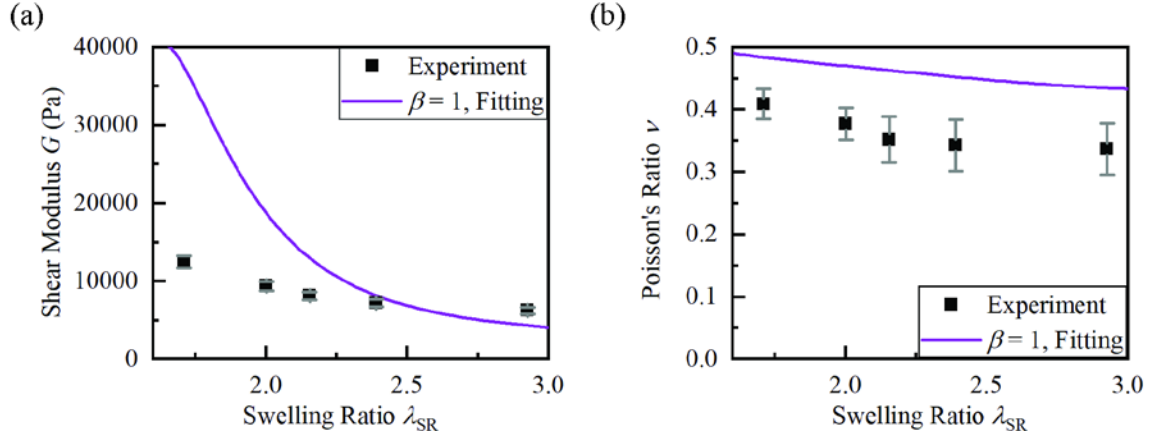


Figure 3.14 Best fitting results of the modified model when forcing $\beta = 1$ ($G_1 = 0.868E4$ Pa, $G_2 = 1.462E4$ Pa, $K_e = 3.068E6$ Pa). (a) shows the results on the shear modulus. (b) shows results on the Poisson's ratio.

The fitting curves in Figure 3.12, Figure 3.13 and Figure 3.14 prove that all the terms in the modified model are necessary. Using the fitting results in Table 3.2, the meaning of the fitting parameters can be further discussed. First, the values for G_1 and G_2 are on the same scale with the shear modulus of the hydrogels, and their values increase with the mass concentration of the monomer during preparation, while their dependence on the mass concentration of the crosslinker is not clear at the current concentration of acrylamide (6%). In the Mooney-Rivlin model, the physics meanings of G_1 and G_2 are constantly explained as the chemical crosslink density and an effective crosslink density caused by polymer entanglement¹⁴⁸. The results of compositions No.1, No.2 and No.3 show that with the same initial concentration of crosslinker, both the chemical crosslink density and the effect of polymer entanglement increase with the initial monomer concentration. The former effect may be caused by a higher crosslinking efficiency at a higher initial monomer concentration, meaning that more crosslinkers effectively connect to polymer chains

during the formation of hydrogel¹⁵³. The latter effect may be explained as the constraint of the deformation of a polymer chain increases with polymer concentration. For polyacrylamide hydrogels with lower initial monomer concentration and relatively higher crosslinker concentration, as in the current study, it has been reported that the crosslinking process becomes more inhomogeneous with the increase of initial crosslinker concentration, which might explain the little correlation between the G_1 , G_2 and the crosslinker concentration^{153,154}.

According to the fitting results in Table 3.2, the value of K_e is several orders higher than that for G_1 and G_2 for all the hydrogel compositions. To further understand this parameter, the Equation (3-9) and Equation (3-10) are rewritten as the following equations.

$$G = G_1\phi^{1/3} + \left(\frac{G_1}{2} + G_2\right)\phi - \frac{\{k_B T[-1 + 2p_a + 2p_c(1 - p_b)]\}\phi^2}{4\beta V_0} \quad (3-11)$$

$$+ \frac{\{[k_B T - 6p_b k_B T p_c(1 - p_b)] + 6K_e \beta V_0\}\phi^3}{6\beta V_0}$$

$$+ O[\phi]^{10/3},$$

$$G \frac{\nu}{1 - 2\nu} = \frac{2G_2}{\phi^{1/3}} - \frac{\{k_B T[-1 + 2p_a + 2p_c(1 - p_b)]\}\phi^2}{4\beta V_0} \quad (3-12)$$

$$+ \frac{[k_B T + 6K_e \beta V_0 - 3p_b k_B T p_c(1 - p_b)]\phi^3}{3\beta V_0}$$

$$+ O[\phi]^{10/3},$$

where $\phi = 1/\lambda_{SR}^3$ is the polymer concentration. In Equation (3-11), when the polymer concentration is higher, the magnitudes of the third and fourth term increase. In the fourth term, the value of K_e needs to be on the scale of $k_B T/\beta V_0$ to effectively influence the value

of shear modulus. With this value of K_e , when the polymer concentration is low, only G_1 and G_2 are related to the shear modulus. For hydrogels in the current study, when the swelling ratio is between 2.5 and 3.0, the contribution from either the term with K_e or the term of mixing energy to the shear modulus is below 5%. Equation (3-12) shows that the compressibility of the material can be influenced by several parameters at a wide range of swelling ratio, but the contribution from G_2 is more significant. It also indicates that G_2 is a necessary parameter to fit the measurements of the Poisson's ratio.

The term with K_e is initially assumed to count for the additional effect of polymer chain entanglements. According to Equation (3-11), this term effectively contributes to the shear modulus together with parameters from the mixing energy. This outcome is due to the mathematical expression of this term corresponding to K_e , not necessarily the physics source of this term. However, it is possible that the physics source for this term being complex. Due to the multiple types of interaction between the water molecules and the polymer chains, which contains both hydrophobic backbones and hydrophilic side groups, the possibility of the spatial distribution of the water molecules and polymer subunits may still deviate from the modified energy of mixing developed by Flory¹¹¹, and it may also depend on solvent concentration, as suggested by a previous study on polyacrylamide hydrogels using molecular dynamics simulation¹⁵⁵. Nevertheless, these effects should be minimized at higher solvent concentration. At higher solvent concentration, there are fewer complex interactions between the polymer chains, and the possibility of the spatial distribution of both the polymer chains and solvent molecules should be closer to the prediction of the classical Flory-Rehner model. Therefore, only for hydrogels at high water

concentration, their shear moduli are almost only related to G_1 and G_2 , the parameters related to the crosslink density and polymer chain entanglement.

The above discussion illustrates the details of a modified model that can describe the swelling-dependent shear modulus and Poisson's ratio of polyacrylamide hydrogels. The discussion also suggests more complex polymer interactions possibly happening at a lower swelling ratio, which could be one of the reasons for the nonlinear decrease of diffusivity with a decreasing swelling ratio. Figure 3.9(c) plots the diffusivity as a function of the swelling ratio for the four compositions together. The results show that both the trend and the magnitude are close for the four compositions. To compare the geometric factors contributing to the diffusivity, the permeabilities as functions of the swelling ratio are calculated and plotted in Figure 3.15. The results show that permeability also increases with the swelling ratio with the same trend. However, the compositions with less initial monomer concentrations, in general, have larger values of permeability at each swelling ratio. A possible explanation is that with the same initial concentration of the crosslinker, the compositions with less monomer concentration form networks that are less homogeneous. As a result, the possibility of locally generating some larger pores becomes higher, which in the end brings up the value of permeability¹⁵³. The exact reason for this phenomenon would need a detailed study of the formation of the polymer network and interaction between molecules, and is beyond the scope of this study. However, these data on solvent diffusion are expected to provide guidance when calculating or simulating the nonlinear poroelastic deformation of hydrogels in future research.

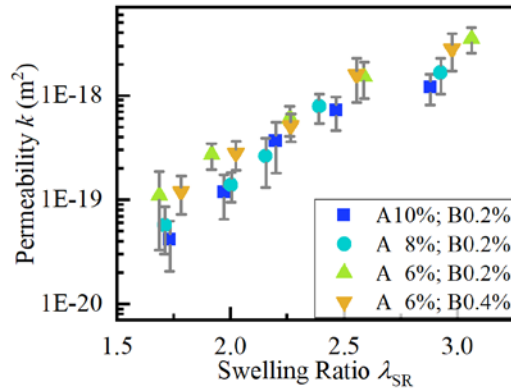


Figure 3.15 Permeability of the polyacrylamide hydrogels at different swelling ratios.

3.5 Conclusion

In this chapter, the polyacrylamide hydrogel is chosen as a model material, and its property dependence on the swelling ratio (or equivalently the solvent concentration) is experimentally examined. The results indicate that the deformation mechanism of the hydrogel goes beyond the original Flory-Rehner theory. This chapter also suggests a simple modified model in which all the parameters are constants over different swelling ratios, except for the Flory-Huggins parameter χ . The modified model has three constant parameters that are related to hydrogel composition, and two other parameters universal for polyacrylamide hydrogels regardless of the initial composition. The modified model can better describe the swelling ratio-dependent linear poroelastic parameters. The results of diffusivity for different hydrogel compositions suggest that the pore size in general increases with swelling ratio nonlinearly, and the exact values might be further related to the details of the microstructures in the polymeric network.

CHAPTER 4. STUDY OF ADHESION PROPERTIES OF HYDROGELS USING INDENTATION OVER A WIDE RANGE OF LENGTH AND TIME SCALES

4.1 Introduction

Adhesion of hydrogels can play important roles in both nature and engineering fields. The adhesion properties of hydrogels are important to quantify, but it is questionable whether the existing indentation methods and contact mechanics models can be readily applied on hydrogels. Apart from this issue, a more fundamental question regarding hydrogel adhesion is that whether the adhesion behavior of hydrogels is also time-dependent and length-dependent, which has been observed on the bulk mechanical properties of hydrogels. Therefore, this chapter first examines the adhesion behavior of hydrogels using indentation over a wide range of length and time scales. Based on the experimental observation, the possible contributions from several mechanisms unique for hydrogels are discussed, including the poroelastic solvent flow and the dangling polymer chains on the material surface, which are not covered in the existing contact mechanics models.

The applicability of the common contact mechanics models with adhesion, such as the JKR model, the DMT model and the Maugis-Dugdale model, is then examined by comparing experimental results with the model prediction. It is found out that the existing models need further modification to describe the adhesion hysteresis phenomenon and the length-dependent adhesion of hydrogels. Driven by this motivation, a modified contact

mechanics model is developed, which includes a cohesive zone for describing adhesion and assumes adhesion hysteresis for the hydrogel surface. The modified model can describe the length-dependent pull-off force and energy of separation in the indentation experiments using a single set of adhesion parameters, indicating it to be a more robust model.

4.2 Experiments

4.2.1 Fabrication of Hydrogel Samples

The model material used in this study was polyacrylamide hydrogel, with acrylamide as the monomer and *N,N'*-Methylenebis(acrylamide) as the cross-linker. To prepare the hydrogel sample, acrylamide stock solution of 40% mass concentration and *N,N'*-Methylenebis(acrylamide) stock solution of 2% mass concentration were made. The two solutions were then mixed with DI water to make a mixture of 6% acrylamide and 0.3% *N,N'*-Methylenebis(acrylamide) in mass concentration. Then an initiator solution composed of 10% ammonium persulfate and 90% DI water, and the catalyst tetramethylethylenediamine were added into the mixture with the volume fraction of 0.5% and 0.05%, respectively. The mixed solution was stirred thoroughly using a mixer and wicked into a gap space of 1 mm thickness between two glass slides. The mixture was then kept at room temperature for 1 hour for full curing. The cured hydrogel was cut into pieces of 1x1 cm² and stored in DI water for one week to assure fully swollen before the indentation experiments.

4.2.2 Indentation Adhesion Tests using Atomic Force Microscope

Before testing, the hydrogel samples were taken out of the DI water and glued to a coverslip, which was then fixed on the bottom of a petri dish. After the glue was dried, the petri dish was filled with DI water with the surface of the hydrogel fully covered by water. Then the sample was placed on the AFM (Asylum MFP-3D Bio). An AFM probe with a polystyrene sphere glued at the end of the cantilever (Novascan) was used as the indenter. The sphere radius was 12.5 μm . The spring constant of the AFM probe was pre-calibrated using the thermal method. Before conducting the indentation measurements, the AFM head had been put above the sample, and the AFM probe had been immersed in the DI water in the petri dish for more than six hours to minimize the effect of drifting of the AFM system.

The indentation panel in the Asylum AFM software was used so that displacement control could be achieved through closed-loop feedback control. Before indentation, the tip was driven to approach the hydrogel surface at a slow speed of 2 $\mu\text{m/s}$. As is shown in Figure 4.1(a), when the sample surface was detected, the probe was driven to press into the sample at a speed of 50 $\mu\text{m/s}$ and then held at a certain indentation depth for a different amount of time. Then the probe was retracted at a speed of 25 $\mu\text{m/s}$ until it reached a position of 4 μm above the detected hydrogel surface to ensure complete detachment. Two groups of experiments were conducted using the AFM. In the first group of experiments, three indentation depths were used: 0.30 μm , 0.50 μm and 0.75 μm , with a series of different contact time ranging from 0.05 s to 180 s. In the second group of experiments, six contact times were selected between 1s and 120s, with a series of different indentation depths ranging from 0.30 μm to 3.00 μm . The retraction speed in all the experiments was 25 $\mu\text{m/s}$. The force on the indenter and the indentation depth were simultaneously recorded as functions of time. The data were recorded at a frequency higher than 500 Hz. For each

set of indentation depth and contact time, the tests were repeated on at least three points on the hydrogel.

4.2.3 Indentation Adhesion Tests using Microindenter

The preparation of the hydrogel sample was the same as that in the AFM indentation experiment. The microindenter (Femtools, FT-MTA03 Micromechanical Testing and Assembly System) had a force probe of 2000 μN force range. A polystyrene sphere (radius 190 μm , Polysciences) was glued to the end of the force probe by epoxy glue.

During the experiment, the probe was driven to approach and indent into the hydrogel sample at the speed of 25 μm . Two groups of experiments were conducted on the microindenter. In the first group of experiments, three indentation depths were used: 10 μm , 20 μm and 30 μm , with a series of different contact time ranging from 0.1 s to 800 s. In the second group of experiments, six contact time between 1 s and 120 s were selected with a series of different indentation depths ranging from 1 μm to 30 μm . The retraction speed in all the measurement is 25 $\mu\text{m}/\text{s}$. The contact force and probe displacement were recorded as functions of time at a recording frequency of 100 Hz. The experiments were carried out on at least three different points on the hydrogel sample.

The force probe on the microindenter had a structure of long shaft with the polystyrene sphere glued at its end. During testing, the sphere was already submerged in water, but the shaft was driven into the water deeper as the indentation depth increases. Therefore, the DI water exerted a capillary force on the shaft. Within the indentation depth adopted in the current study, the capillary force exerted on the shaft had a linear relationship with the shaft displacement, because the liquid surface was pinned on the shaft surface.

Therefore, the force data from the experiments were calibrated using the force-displacement data before the sphere got into contact with the hydrogel.

4.3 Results and Discussion

4.3.1 Time-Dependent Adhesion of Hydrogels

Figure 4.1 shows one representative result of the indentation measurements obtained from AFM with a polystyrene sphere of 12.5 μm radius (Figure 4.1 (a) (b) and (c)) and the microindenter with a polystyrene sphere of 190 μm radius (Figure 4.1(d) (e) and (f)). The compressive force is set to be positive, and the tensile force is set to be negative. The loading part of the force curve is colored in black, the holding part of the curve is colored in green, and the unloading part is colored in blue. The material's behavior in the loading, holding and unloading periods will be discussed individually in the following sections.

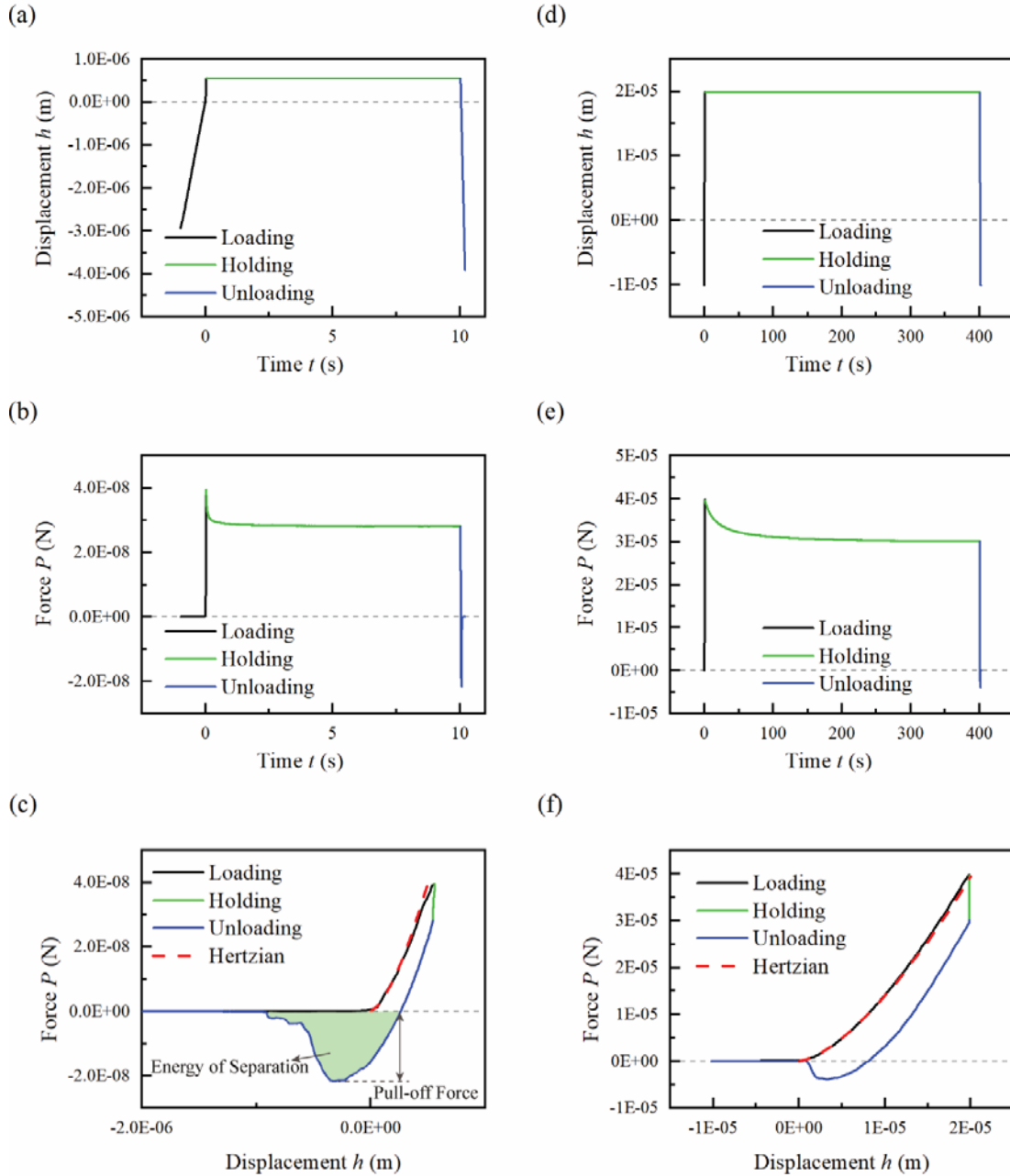


Figure 4.1 Testing method. (a) Displacement-controlled indentation testing procedure on AFM. (b) The measured force-time curve on AFM. (c) The force-displacement plot from AFM test. (d) Displacement controlled indentation testing procedure on microindenter. (e) The measured force-time curve on microindenter. (f) The force-displacement plot from the microindenter test.

In the loading period, as the indenter is pressed into the gel, the force on the indenter increases. No jump-in contact (i.e. no negative force) is observed as the indenter approaches the hydrogel surface, which means no long-range interaction between the two surfaces is developed. The loading curves in both AFM and microindenter results are fitted with Hertzian's solution, $P = 16/3Ghc_0$, where P is the force on the indenter, G is the shear modulus of the material, and $c_0 = \sqrt{Rh}$ is the contact radius with R being the radius of the indenter and h the indentation depth⁴⁰. As shown in Figure 4.1(c) and (f), the dash red lines are the plots of Hertzian solution with fitting parameter $G= 6.0$ kPa. The Hertzian theory is based on linear elasticity without the consideration of surface adhesion. The perfect fitting between the Hertzian solution and the loading portion of the experimental curves from both AFM and microindenter further confirms that no or little adhesion has been developed as the indenter approaches and compresses into the hydrogel. It also indicates that the surface tension and surface stress effects that might play a role in the indentation of soft materials as reported in previous literature^{156–159} are negligible in the current material system.

In the holding period, as the indentation depth is held constant, the force on the indenter relaxes until a plateau is reached (Figure 4.1 (b) and (e)). The relaxation time depends on the size of the indentation. For the AFM test, the relaxation time is around 1 s, while for the microindenter test, the relaxation time is around 100 s. To further quantify the time-dependent behavior, Figure 4.2 plots the force relaxation curves under three depths of indentations in both AFM (black, red, and blue solid lines for $h=0.3, 0.5$ and 0.75 μm respectively) and microindenter (black, red and blue dash lines for $h=10, 20$ and 30 μm respectively). Here, $P(0)$ and $P(\infty)$ are used to represent the initial force and relaxed force

from each relaxation measurement. In Figure 4.2(a), the result is plotted in the form of normalized force $[P(t)-P(\infty)]/[P(0)-P(\infty)]$ against contact time t , and it shows that the six curves are clearly apart for different contact radius. In Figure 4.2(b), the result is replotted in the form of normalized force $[P(t)-P(\infty)]/[P(0)-P(\infty)]$ against normalized time t/c_0^2 , and it shows the six curves collapse. This scaling of relaxation time with contact radius squared indicates that the time-dependent behavior of the hydrogel is dominated by poroelasticity^{64,65}.

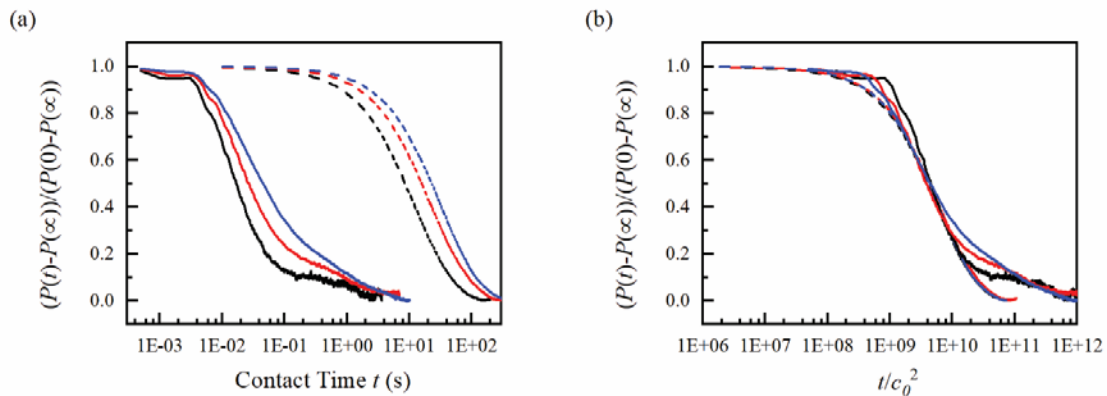


Figure 4.2 Time-dependent poroelastic behaviors of gels. The force relaxation curves from AFM and microindenters are plotted as (a) normalized force $(P(t)-P(\infty))/(P(0)-P(\infty))$ against time t , and (b) normalized force $(P(t)-P(\infty))/(P(0)-P(\infty))$ against normalized time t/c_0^2 . The black, red, and blue solid lines are from AFM measurements with a contact radius of 1.94, 2.50, and 3.06 μm respectively. The black, red and blue dash lines are from microindenter measurements with contact radius of 43.6, 61.6 and 75.5 μm respectively.

In the unloading period after a period of holding, the indenter is retracted from the hydrogel. As the indenter moves up, the compressive force on the indenter decreases, and

when the force reaches zero, the indenter is still below the hydrogel surface. As the indenter is further retracted, a tensile force is developed on the indenter until a maximum value is reached. The maximum tensile force during retraction is called “pull-off force”. After that, the hydrogel starts to separate from the indenter, and the force on the indenter decreases until the two surfaces are completely separated and the indenter force becomes zero (Figure 4.1(c) and (f)). This result indicates that significant adhesion has been developed during the time the indenter and the hydrogel are in contact.

Then the effect of contact time on adhesion is examined. The indentation adhesion tests with a series of different contact times are conducted on both AFM and microindenter (Figure 4.3). The results are plotted in Figure 4.3(a) and Figure 4.3(b) for AFM and microindenter, respectively. Each curve represents one loading, holding and retraction measurement. The overlap of the curves shows very good repeatability of the measurements in the loading and holding period. It is observed that in the AFM test with the contact radius of 2.50 μm (estimated from Hertzian solution), the poroelastic force relaxation ends at around 1 second, but the pull-off force keeps increasing as the holding time increases. A similar result is observed in microindenter measurements, in which the contact radius is 61.6 μm (estimated from Hertzian solution) and the poroelastic force relaxation ends at around 100 seconds, but the pull-off force keeps increasing even after 800 seconds of contact. The longest holding time is 180 s for AFM test and 800 s for microindenter test. These parameters are chosen based on experience to guarantee minimal or no influence of system drift. During the force relaxation period, the liquid inside the gel underneath the indenter is squeezed out of the gel. The loss of solvent increases local polymer concentration and could potentially increase the possibility for the polymer chains

to form contact with the indenter. However, unlike expected, the poroelastic relaxation or solvent diffusion has little or no influence on the adhesion. After the poroelastic relaxation is finished, the adhesion keeps increasing over a much longer time scale. This time scale for the adhesion to build up is independent of macroscopic indentation size. The mechanism controlling this time scale is intrinsic to the material, which might be related to the chemical bond dynamics between the polymer in the gel and the polystyrene indenter surface. As the poroelastic relaxation has little influence on the adhesion, the adhesion is also observed to have little effect on the poroelastic relaxation process. As shown in Figure 4.3, although the pull-off force keeps increasing with the contact time, the contact forces on the indenter during the whole holding period after the poroelastic relaxation are kept at a constant value. This result indicates that the adhesion is mostly attributed to the increase of adhesion sites within the initial contact area. The formation of adhesion sites outside of the initial contact area, if there is any, is not large enough to exert noticeable traction force on the indenter before the indenter is retracted. Consequently, the Hertzian solution $c_0 = \sqrt{Rh}$ provides a good estimation of the contact radius throughout the whole loading and holding processes, and in later description, the initial contact radius is referred to as the Hertzian contact radius for simplicity. The total decoupling of the time-dependent bulk properties of the hydrogel with its time-dependent adhesion properties allows a simple model to be built to extract the adhesion properties, which will be discussed in the next section.

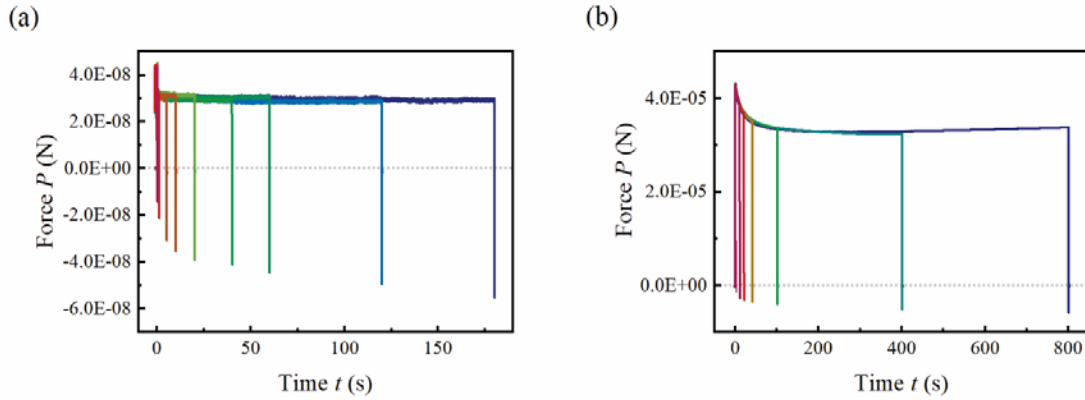


Figure 4.3 Measurements at different contact times. (a) The force-time plot of AFM tests with a series of different contact times before retraction. The sphere is of $12.5 \mu\text{m}$ radius, and indentation depth is $0.5 \mu\text{m}$ during holding. (b) The force-time plot of microindenter tests with a series of different contact times before retraction. The sphere is of $190 \mu\text{m}$ radius, and indentation depth is $20 \mu\text{m}$ during holding. In both AFM and microindenter tests, the unloading rate is $25 \mu\text{m/s}$.

To quantify the time-dependent adhesion of gels, two values are first extracted from the measurements: one is the pull-off force P_{pf} , and the other is the energy of separation W_s that is calculated by integrating the force over displacement for the tensile force part – the area below $P = 0$ in the force-displacement plot (Figure 4.1(c)). The experimental data are expanded by repeating the measurements in Figure 4.3 with three different indentation depths in both AFM and microindenter. The pull-off force and energy of separation are plotted against contact time in Figure 4.4 for the three depths of indentation measurements from AFM and microindenter, respectively. The error bars represent the standard deviation of the results obtained on three points on the sample. In the AFM tests, the radius of the sphere is $R = 12.5 \mu\text{m}$, and the indentation depths are $h = 0.3, 0.5$ and $0.75 \mu\text{m}$. Using the Hertzian solution, the radii of contact are $c_0 = 1.94, 2.50,$ and $3.06 \mu\text{m}$. Under these contact sizes, the poroelastic relaxation time is around 0.5 to 1.0 seconds. In the microindenter

tests, the radius of the sphere is $R = 190 \mu\text{m}$, and the indentation depths are $h = 10, 20$ and $30 \mu\text{m}$. Using the Hertzian solution, the radii of contact are $c_0 = 43.6, 61.6,$ and $75.5 \mu\text{m}$. Under these contact sizes, the poroelastic relaxation time is around 60 to 200 seconds. As shown in Figure 4.4, as the contact time increases, the pull-off force and energy of separation increase in both small scale testing from AFM and larger scale testing from microindenter. Before and after the poroelastic relaxation, the time dependency does not have clear change. Each group of data can be fitted with one single straight line rather than two lines of different slopes for the portions before and after the poroelastic relaxation respectively. It also indicates that the water flow related to poroelasticity has a negligible influence on the formation of adhesion sites. For the hydrogel tested in this study, it can be concluded that poroelasticity has a negligible influence on the time for the adhesion to build up between the indenter and the hydrogel surface. The slope of each fitted line is listed in Table 4.1. The average slope of the pull-off force against the contact time curve combining both AFM and microindenter tests is 0.20 ± 0.03 , and the average slope of the energy of separation against the contact time curve combining both AFM and microindenter tests are 0.30 ± 0.06 . Here, a clear conclusion that can be drawn from the current result is that the time for the hydrogel to build adhesion is related to a time scale that is intrinsic to the polymer bonding dynamics and is independent of any macroscopic length scales. Based on the surface chemistry of the material system in this study (polyacrylamide hydrogel surface and polystyrene surface under water), the adhesion is mainly due to hydrophobic interaction.

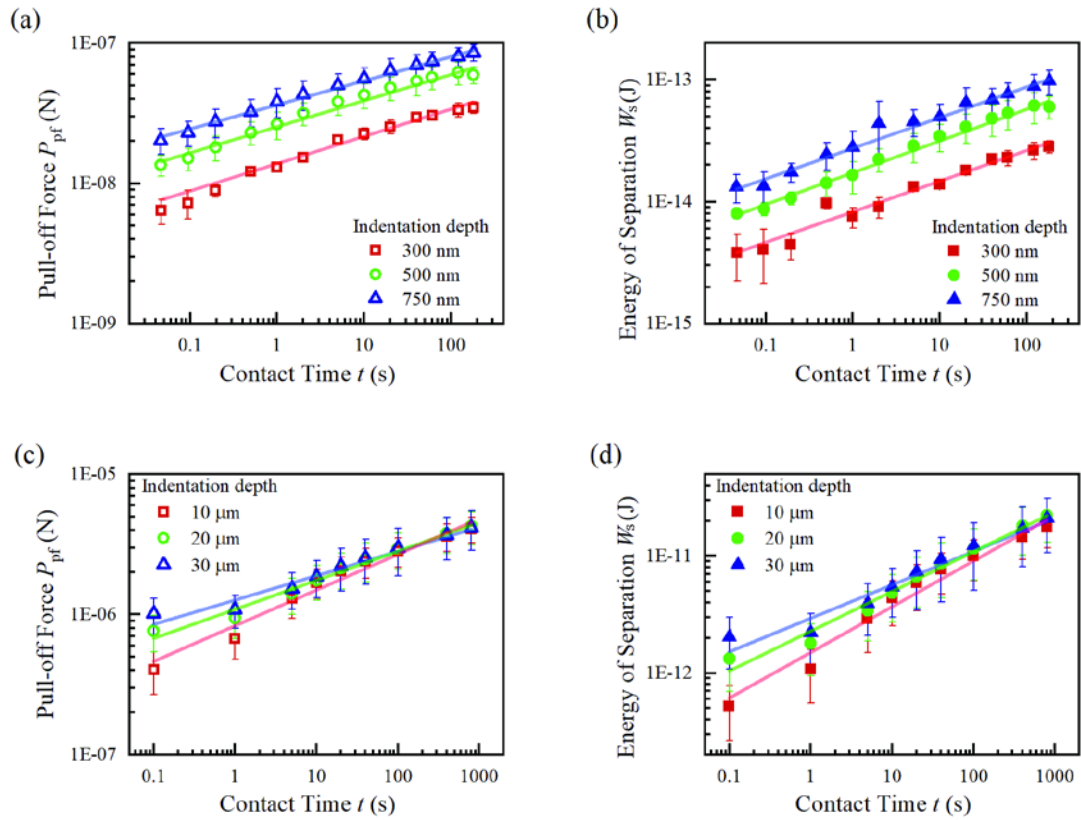


Figure 4.4 Time-dependent adhesion. (a) Pull-off force and (b) energy of separation are plotted as a function of contact time at different indentation depths in AFM experiments (indenter radius 12.5 μm). (c) Pull-off force and (d) energy of separation are plotted as a function of contact time at different indentation depths in microindenter experiments (indenter radius 190 μm).

Table 4.1 List of the fitting slope of the pull-off force and energy of separation against contact time results from AFM and microindenter tests under different indentation depths in Figure 4.4.

	Radius of indenter	Indentation depth	Fitting slope of pull-off force – contact time curve	Fitting slope of energy of separation – contact time curve
AFM	12.5 μm	300 nm	0.19	0.25
	12.5 μm	500 nm	0.19	0.26
	12.5 μm	750 nm	0.17	0.25
Microindenter	190 μm	10 μm	0.25	0.39
	190 μm	20 μm	0.21	0.34
	190 μm	30 μm	0.17	0.29

4.3.2 Length-Dependent Pull-Off Force and Energy of Separation

Besides time-dependent adhesion, the results in Figure 4.4 also indicate length dependence. The magnitude of adhesion increases as the indentation depth increases in the AFM tests (Figure 4.4(a) (b)) but does not change much as the indentation depth increases in the microindenter tests (Figure 4.4(c) (d)). To better present the length-dependent adhesion, the tests are expanded to include more indentation depths, but still confine the choice to maintain small deformation. In Figure 4.5, the pull-off force and energy of separation are plotted as a function of contact radius with 10s and 120s holding time, respectively. The yellow rhombuses represent the data from AFM of eight different indentation depths, and the blue circle from microindenter of twelve different indentation depths. As the contact radius increases, the pull-off force and energy of separation increase, and gradually reach a plateau when the contact radius approaches a certain value (about 40 μm in the current material system). First, this length-dependent adhesion is not likely due to the surface roughness effect. In that case, when the indentation depth is small, the indenter is only partially in contact with the sample surface, and as the indentation depth increases, the bumpy features on the surface are significantly deformed and the real contact area increases until full contact is reached. However, the surface roughness of the hydrogel in the current study is in the order of 10nm⁸⁰, and even the smallest indentation depth and contact radius used in this study are more than one order of magnitude larger than the surface roughness scale of the gels. Another factor that has been related to the length-dependent adhesion in literature is the surface stress of the material^{157,158,160}. Because both the indenter and the hydrogel are submerged in water throughout the experiment, and the hydrogel sample in the current study has water concentration as high as 94%, it is expected

that the polymer chains on the hydrogel surface respond to elastic deformation the same as those inside the polymer network, and the surface stress effect is negligible. This argument is also supported by the fact that the force-displacement curve in the loading part of the experiments can be fitted very well with the Hertzian model. If the surface stress plays a role, it would also alter the loading curve to deviate from the Hertzian solution. As a result, the length dependence observed in this study is also not material intrinsic, but is due to mechanical effect.

A rough assumption for this mechanical effect is as follows. In small contact size, the pull-off force is primarily controlled by the more uniform bond ruptures between the hydrogel and the indenter surface, while in large contact size, the pull-off force is more likely to be the Griffith type of fracture.^{161,162} This length-dependent adhesion cannot be directly modeled by either JKR or DMT theory, in which the pull-off force P_{pf} is predicted only related to the adhesion energy γ and radius of the sphere R as $P_{pf} \sim \gamma R$. Even if they are applicable, they will be only for the plateau region in Figure 4.5. Before having a pre-knowledge of the adhesion energy of the hydrogel, it is not clear that JKR or DMT model is even applicable for the plateau region. Therefore, a more general theory is used based on the cohesive zone model proposed by Maugis⁸⁸, to analyze the data. Because significant hysteresis of adhesion exists between loading and unloading, the original Maugis-Dugdale model needs to be modified to be useful. The details of the theory are discussed in the next section.

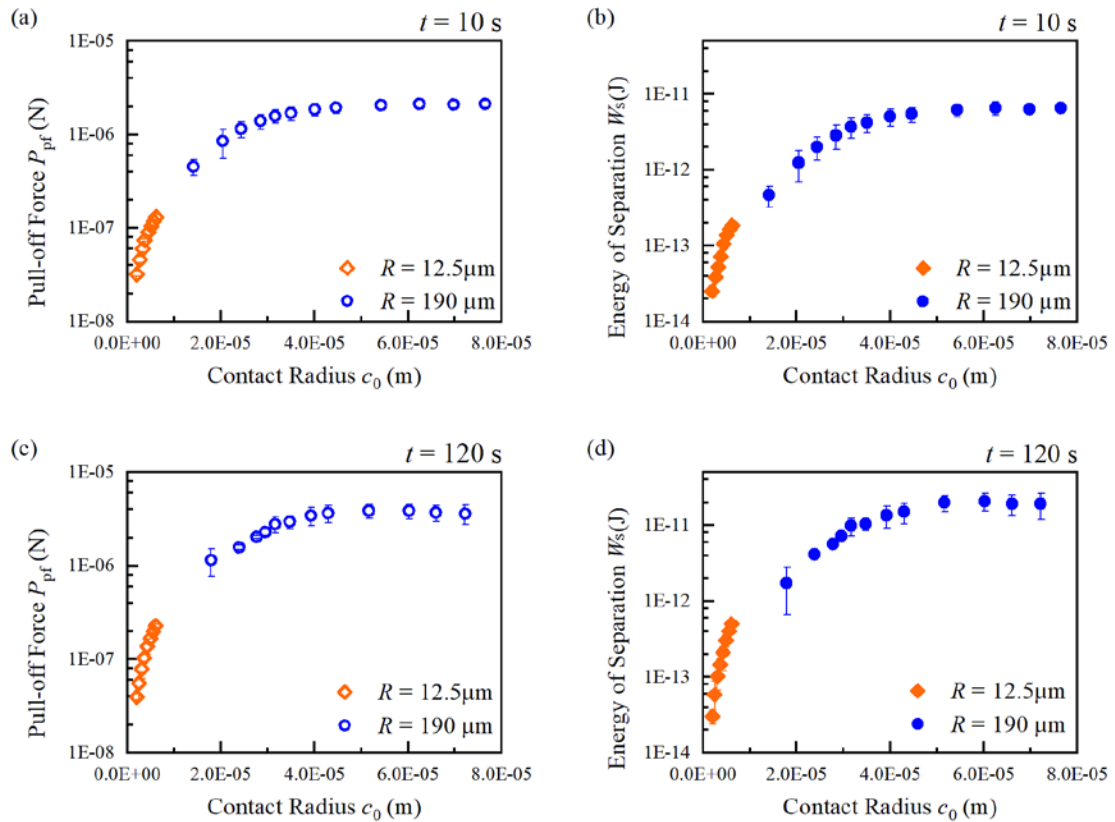


Figure 4.5 Length-dependent pull-off force and energy of separation. (a) Pull-off force and (b) energy of separation are plotted as functions of contact radius under 10 seconds contact time. (c) Pull-off force and (d) energy of separation are plotted as functions of contact radius for 120 seconds contact time.

4.3.3 Modified Maugis-Dugdale Model

As discussed earlier, the force-displacement curve during the loading period fits the Hertzian solution very well, indicating that little or no adhesion is built between the indenter and the hydrogel surface, but after a period of holding, adhesion is developed and it increases over time. At this stage, when the indenter is retracted from the hydrogel, significant hysteresis due to adhesion is observed between the loading and unloading

curves (Figure 4.1(c) and (f)). Therefore, there exists a transition stage from the non-adhesive loading to the adhesive unloading. In this section, the path of this transition stage on the force-displacement plot is modeled, and its effect is discussed.

For generality, the adhesion formed between the indenter and the hydrogel is assumed to follow a Dugdale traction-separation law with a constant cohesive strength σ_0 over a finite separation distance l_0 . As illustrated in Figure 4.6(a), the contact between the spherical indenter and the hydrogel is assumed to follow the Hertzian contact model until the end of loading, and the contact radius is $c_0 = \sqrt{Rh}$. At the beginning of unloading, the radius of contact does not decrease, as the energy release rate is still less than the enhanced adhesion energy. As a result, an annular region of the cohesive zone is developed along the edge of the contact. As the indenter is retracted further, the cohesive zone size increases but keeping the outer edge of the contact unchanged until the energy release rate in the system reaches the value of adhesion energy. Then the two surfaces start to separate from the outer edge of contact and propagate inwards.

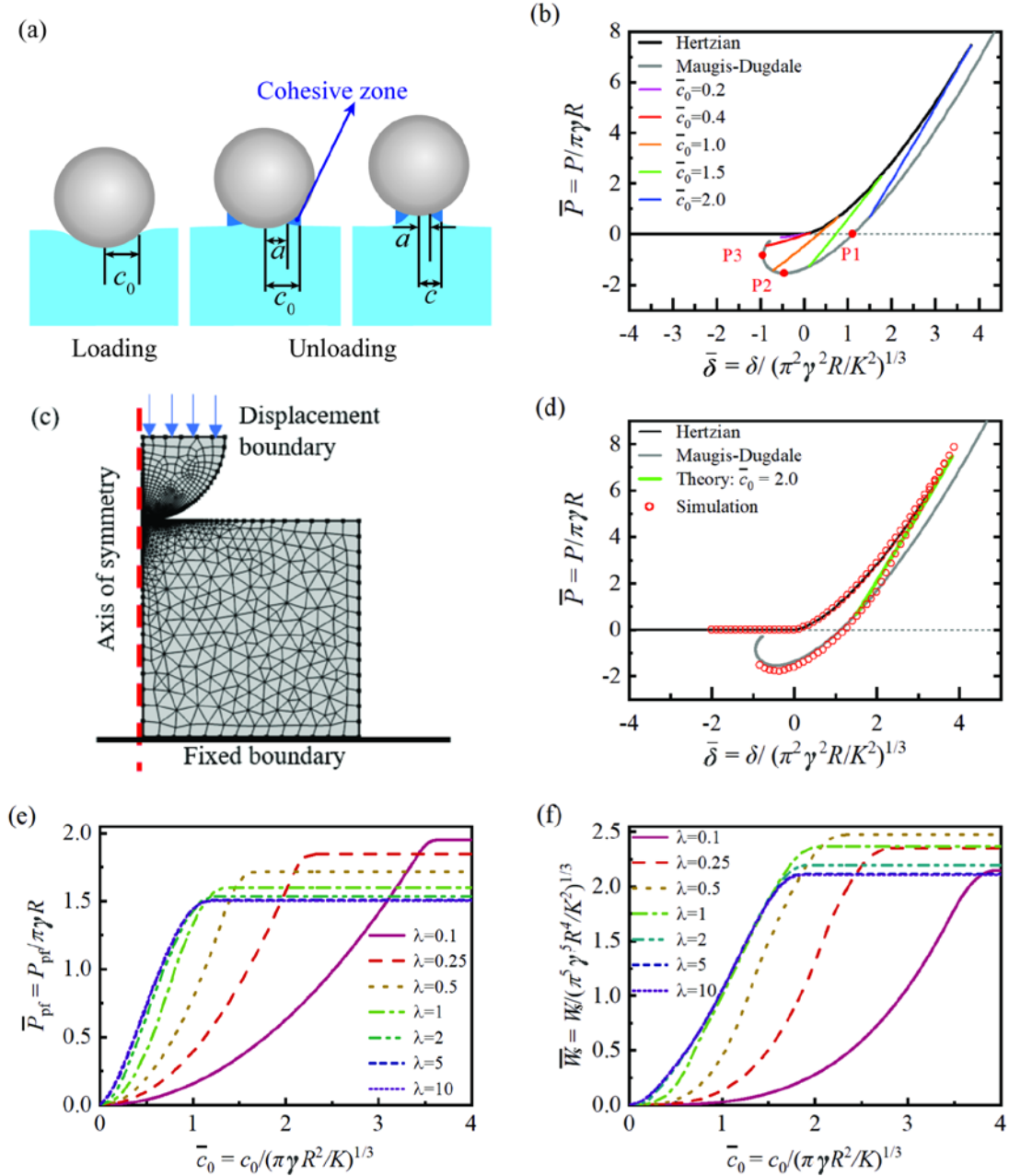


Figure 4.6 Modified Maugis-Dugdale model. (a) Schematics of the cohesive model and illustration of the retraction process. (b) Analytical result of the normalized force-displacement curve at a few different values of the normalized initial contact radius \bar{c}_0 , for $\lambda=2$. (c) The setup of the numerical simulation in Comsol. (d) Comparison of the numerical and theoretical results for the case of $\bar{c}_0 = 2$ and $\lambda=2$ for verification of the analytical result. (e) The normalized pull-off force and (f) the normalized energy of separation against normalized initial contact radius \bar{c}_0 , at different values of parameter λ .

The indenter and the material do not separate during the transition stage, and the stress concentration at $r = a$ is always eliminated by the cohesive zone within $a < r < c$, where a is the real contact radius excluding the cohesive zone, and c is the apparent contact radius including the cohesive zone (Figure 4.6(a)). To satisfy this requirement, the force on the indenter and the indentation depth has the following relations with a and c , which were derived by Maugis by solving the boundary value problem and eliminating the stress concentration⁸⁸. Following the notation in Maugis' work:

$$\bar{P} = A^3 - \lambda A(\sqrt{(c/a)^2 - 1} + (c/a)^2 \arctan \sqrt{(c/a)^2 - 1}), \quad (4-1)$$

$$\bar{\delta} = A^2 - (4/3)A\lambda\sqrt{(c/a)^2 - 1}, \quad (4-2)$$

where $A = a/(\pi\gamma R^2/K)^{1/3}$ is the normalized contact radius, $\bar{P} = P/\pi\gamma R$ is the normalized contact force, $\bar{\delta} = \delta/(\pi^2\gamma^2 R/K^2)^{1/3}$ is the normalized indentation depth, and $\lambda = 2\sigma_0/(\pi\gamma K^2/R)^{1/3}$ is a dimensionless parameter. Here, γ is the adhesion energy, and K is the reduced modulus with $K = 4E/[3(1 - \nu^2)]$, where E is material's Young's modulus and ν is Poisson's ratio.

Until now, the Force-displacement relation cannot be readily obtained since both a and c are unknown in Equations (4-1) and (4-2). In the Maugis-Dugdale model, the relation between the parameters is further restricted to satisfy the energy balance of elastic deformation, external loading and the creation of the new surface, which gives

$$\frac{\lambda A^2}{2} \left[\sqrt{m^2 - 1} + (m^2 - 2) \arctan \sqrt{m^2 - 1} \right] \quad (4-3)$$

$$+ \frac{4\lambda^2 A}{3} \left[\sqrt{m^2 - 1} \arctan \sqrt{m^2 - 1} - m + 1 \right] = 1$$

where $m = c/a$.

During the transition stage, the energy release rate is still smaller than the adhesion energy, Equation (4-3) is not applicable yet. During this period, the apparent contact radius c remains constant c_0 . Substituting $c = c_0$ into Equation (4-1) and (4-2), the expressions for \bar{P} and $\bar{\delta}$, yields a force-displacement curve for the transition stage during unloading. In this stage, the apparent contact radius remains a constant value, but as the indenter is further retracted, the cohesive zone becomes bigger and the real contact area becomes smaller, until the cohesive zone fully develops and the energy release rate equals the adhesion energy. At this point, the behavior transits to follow the Maugis-Dugdale model, which satisfies all Equations (4-1)-(4-3).

The results of the analytical solutions are shown in Figure 4.6(b) for $\lambda = 2$. The normalized force-displacement curves for the Hertzian model and the Maugis-Dugdale model are plotted as black and grey lines. The proposed transition curves from Hertzian to Maugis-Dugdale are shown in different colors for a few different values of the initial contact radius ($\bar{c}_0 = c_0/(\pi\gamma R^2/K)^{1/3}$). The force-displacement curve for the whole indenting and retracting process first follows the Hertzian model, then follows the transition curve at the beginning of unloading, and finally follows the Maugis-Dugdale model. The transition point to the Maugis-Dugdale model differs depending on the value of the initial contact radius \bar{c}_0 . For most of the cases, the transition curve intersects with

the Maugis-Dugdale curve. At this intersection point, the contact switches from the transition stage to the Maugis-Dugdale model. The final adhesion behavior, e.g. the pull-off force and the energy of separation, depends on the location of the intersection point on the Maugis-Dugdale force curve. If \bar{c}_0 is large enough (e.g. $\bar{c}_0 = 2.0$, the blue curve in Figure 4.6(b)), the intersection point is above the zero force point 1 . The pull-off force is the minimum value on the Maugis-Dugdale force curve. Under the displacement-controlled condition, the material detaches from the indenter surface at point 3 . Therefore, both the pull-off force and energy of separation are constants. When \bar{c}_0 is smaller and the intersection point is between point 1 and point 2 (e.g. $\bar{c}_0 = 1.5$, the green curve in Figure 4.6(b)), the calculated pull-off force is still the minimum force predicted by the Maugis-Dugdale model, but the energy of separation decreases for lower initial contact radius. When the intersection point is between point 2 and point 3 (e.g. $\bar{c}_0 = 1.0$, the orange curve in Figure 4.6(b)), the pull-off force is the force at the intersection point. Under displacement-control, the unloading force still follows the Maugis-Dugdale model until it reaches point 3 . Therefore, both the pull-off force and energy of separation decrease with decreasing initial contact radius. When \bar{c}_0 further decreases, the intersection point is above point 3 (e.g. $\bar{c}_0 = 0.4$, the red curve in Figure 4.6(b)), the material surface detaches from the indenter immediately when it reaches the intersection point. If \bar{c}_0 is small enough (e.g. $\bar{c}_0 = 0.2$, the pink curve in Figure 4.6(b)), it is possible that the transition curve does not intersect with the Maugis-Dugdale force curve. At the end of the transition stage, the real contact radius decreases to zero, and the material surface detaches from the indenter immediately. In these latter two cases, the pull-off force and energy of separation decrease with decreasing initial contact radius.

To verify the analytical solution, numerical simulation is carried out. A finite element model of the indentation problem is implemented in the commercial finite element software COMSOL Multiphysics v. 5.4 through the *Solid Mechanics* module. An axisymmetric boundary value problem is created, as is shown in Figure 4.6(c). The hydrogel is modeled as a linear elastic material with a shear modulus of 6 kPa and Poisson's of 0.49. The unloading process is fast, and the solvent does not have enough time to migrate, so the gel is assumed to be close to incompressible. The spherical indenter is deformable but with a shear modulus ten times larger than the soft hydrogel. Following the geometry of the experimental setup in the microindenter, the radius of the spherical indenter is set to be 190 μm . Initially, the indenter is above the hydrogel surface. The indenter is first compressed to a certain depth into the hydrogel and then retracted to the original location. The adhesion is activated after the indenter and the hydrogel are in full contact. The cohesive model is described by specifying a trapezoid traction-separation law with a very steep slope at both ends to simulate the ideal Dugdale cohesive model. In the simulation, the cohesive strength is set to be $\sigma_0 = 3.24$ kPa, and the adhesion energy $\gamma = 0.002$ J/m². The indentation depth is 7.77 μm , corresponding to the case of $\lambda = 2$ and $\bar{c}_0 = 2$. The reaction force is calculated by integrating the normal traction on the hydrogel surface. The model consists of 21228 domain elements and 2220 boundary elements. The direct linear solver MUMPS is used. In Figure 4.6(d), the simulation result is plotted together with the analytical result for the case of $\lambda = 2$ and $\bar{c}_0 = 2$. Good agreement is achieved, which verifies the analytical model.

For the parametric study, the analytical results of the normalized pull-off force and energy of separation are plotted as functions of the normalized initial contact radius for a

series values of λ from 0.1 to 10, representing conditions from that close to the DMT model to that close to the JKR model. Both the pull-off force and the energy of separation continue to increase with the initial contact radius until a critical value is reached. The critical initial contact radius for the energy of separation is always higher than that for the pull-off force. Notice the normalized pull-off force for $\lambda=10$ is close to 1.5 when reaching constant, which agrees with the JKR model. Also, the normalized pull-off force for $\lambda=0.1$ is close to 2.0 upon reaching constant, which agrees with the DMT model.

Using this analytical model, the adhesion properties of the hydrogels in contact with the polystyrene sphere are extracted from the experiments. Fitting the theoretical curves with the experimental data gives the adhesion energy γ as 0.0019 J/m^2 and cohesive strength σ_0 as 2.5 kPa, which in turn gives a $0.76 \text{ }\mu\text{m}$ separation distance, for the 10 s holding time experiment. As is shown in Figure 4.7(a) and Figure 4.7(b), the model well captures the overall trend of the experimental results. If the polyacrylamide polymer chains have an extended length of $0.76 \text{ }\mu\text{m}$ as the separation distance extracted from the cohesive zone model, the number of monomers per chain can be estimated as $n=2533$ ⁶³. A coiled polymer chain of this extended length has a radius of about 15 nm in the unstressed state, which is close to the mesh size of the gel network. Using this model, the adhesion energy and cohesive strength values for different contact time at retraction speed of $25 \text{ }\mu\text{m/s}$ are also extracted. The result is shown in Figure 4.7(c), and Figure 4.7(d). The adhesion energy, cohesive strength and separation distance all increase over time.

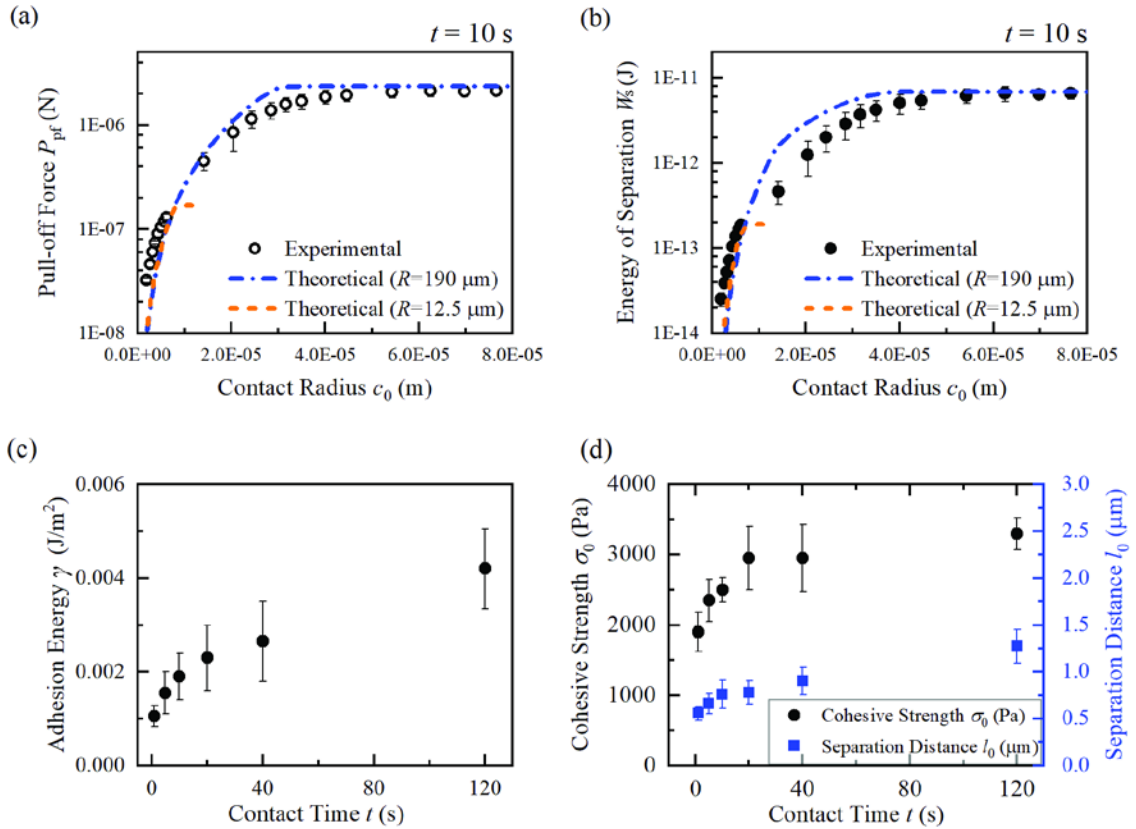


Figure 4.7 (a) Pull-off force as a function of initial contact radius for both experimental and theoretical fitting; (b) Energy of separation as a function of initial contact radius for both experimental and theoretical fitting. (c) Fitting results of adhesion energy as a function of contact time. (d) Fitting results of adhesion strength and separation distance as a function of contact time.

4.4 Conclusion

In this work, indentation adhesion experiments are conducted on a polyacrylamide hydrogel under a wide range of contact length and contact time. It is observed that the poroelasticity of the hydrogel leads to contact force relaxation, but the solvent migration under the contact area has little influence on the adhesion in the current hydrogel-indenter system. The pull-off force and energy of separation increase with contact time. The time

scale is independent of any macroscopic length scale and is most likely related to the molecular mobility of the polymer chains and the chemical bonding dynamics between the gel surface and the polystyrene sphere. Additionally, the pull-off force and energy of separation are also observed to increase with contact radius initially but become constants when the contact radius reaches certain values. To model the length-dependent behavior and extract intrinsic adhesion properties of the interface, an analytical solution is developed based on the Maugis-Dugdale model. The results from this chapter suggest a method of measuring the adhesion of soft hydrated materials at multiple time and length scales for a more accurate understanding of the interfacial properties.

CHAPTER 5. STUDY OF ADHESION PROPERTIES OF HYDROGELS WITH DIFFERENT COMPOSITIONS

5.1 Introduction

When a hydrogel is in contact with another material under water, it is the polymer chains on the hydrogel surface that form adhesion with the surface of the material³¹. Tuning the chemistry of the polymer chains has been explored as an effective approach in altering the adhesion properties of hydrogels in the previous studies^{10,30,60}. However, whether or how the structural properties of the polymer chains, e.g., polymer density or polymer chain length, influence hydrogels' adhesion properties has rarely been studied. Systematic experimental studies of the adhesion of hydrogels with different compositions will be the first step towards a more comprehensive understanding of the mechanism.

In this chapter, the indentation adhesion method developed in Chapter 4 is applied on polyacrylamide hydrogels with different compositions, i.e. different amounts of monomers and crosslinkers when preparing the hydrogels. The hydrogel samples are prepared in a way that the properties of the surface polymer chains follow that in the bulk hydrogel. The indentation adhesion tests are carried out over a wide range of contact radius to apply the modified Maugis-Dugdale model. Measurements are also conducted at a series of holding time to study the time dependence of adhesion parameters. By analyzing the possible relation between the adhesion parameters of hydrogels and the structural parameters of the polymer chains, more detailed information on hydrogel adhesion is revealed.

5.2 Experiments

5.2.1 Preparation of Hydrogel Samples

A series of polyacrylamide hydrogels were prepared. The compositions can be put into two groups, as shown in Table 5.1. In the first group, the initial mass concentrations of the monomer are fixed, while the initial mass concentrations of the crosslinker are different. In the second group, the initial mass concentrations of the monomer are different, but the ratio of mass concentrations between the monomer and the crosslinker is fixed.

To make the hydrogel samples, the stock solution of acrylamide solution of 40% mass concentration and *N,N'*-Methylenebis(acrylamide) solution of 2% mass concentration were first prepared. For each hydrogel composition, the two stock solutions were mixed with DI water to attain the initial mass concentration as listed in Table 5.1. The mixed solution was then added with ammonium persulfate solution (10% mass concentration) and catalyst tetramethylethylenediamine, with a volume concentration of 0.5% and 0.05%, respectively. The mixed solution was stirred on a mixer and poured into a closed mold of 1 mm thickness. The upper and lower sides of the mold were made of clean glass to ensure the maximum similarity of polymer chains on the hydrogel surface and in the bulk^{163,164}. The solution was cured in the mold for an hour, and the formed hydrogel was taken out of the mold and put into DI water for a week to ensure full saturation. The mass of each hydrogel sample before and after swollen was measured separately. The swelling ratio of the hydrogel was calculated as $\lambda_{SR} = \left(1 + \left(\frac{m_{gel}}{m_{polymer}} - 1\right) \cdot \frac{\rho_{polymer}}{\rho_{water}}\right)^{1/3}$, where $\rho_{polymer}=1.443 \text{ g/cm}^3$ and $\rho_{water}=1.0 \text{ g/cm}^3$. The value $m_{polymer}$ was estimated by the mass of

the hydrogel immediately after prepared ($m_{\text{prepared-gel}}$) and the mass concentration of the monomer (c_m) and crosslinker (c_c): $m_{\text{polymer}} = m_{\text{prepared-gel}}(c_m + c_c)$.

Table 5.1 Compositions of the polyacrylamide hydrogel samples.

No.	Initial Mass Concentration of Acrylamide	Initial Mass Concentration of <i>N,N'</i> -Methylenebis(acrylamide)	Group
1	10%	0.1%	Group 1
2	10%	0.2%	Group 1
3	10%	0.3%	Group 1
4	10%	0.4%	Group 1
5	10%	0.5%	Group 1 Group 2
6	5%	0.25%	Group 2
7	7.5%	0.375%	Group 2

5.2.2 Indentation Adhesion Experiment on AFM

The indentation adhesion tests were conducted on both the AFM and the microindenter, with spherical indenters of the same material but different sphere radii (polystyrene beads, Polyscience, Inc). The testing procedures in general follow the experimental section in Chapter 4. They are described in this section as steps for an established method.

For tests on the AFM (Asylum MFP3D-Bio AFM), a polystyrene sphere of radius $12.5\ \mu\text{m}$ was glued to the end of an AFM cantilever using a micromanipulator. The spring constant of the cantilever was calibrated by the thermal method. A fully swollen hydrogel sample was glued to a coverslip, which was then glued to the center of a petri dish. Before the experiment, both the hydrogel sample and the AFM probe had been submerged in DI water for more than six hours for the whole system to reach thermal equilibrium. The sample and the AFM probe were still submerged in DI water throughout the test.

As is illustrated in Figure 5.1(a), in the indentation adhesion test, the indenter was first driven to approach the hydrogel surface at a speed of $2\ \mu\text{m/s}$. After the surface was detected, the indenter was driven to press into the sample at a speed of $50\ \mu\text{m/s}$ until a preset indentation depth was reached. Then the indentation depth was fixed for a preset amount of holding time using the closed-loop feedback built in the AFM controlling software. After the holding, the indenter was retracted at the speed of $25\ \mu\text{m/s}$. Both the indentation depth and the contact force throughout the test were recorded. Examples of the force-time curve and the force-displacement curve are illustrated in Figure 5.1(c) and Figure 5.1(e). The indentation depth used in the AFM tests spanned from $0.25\ \mu\text{m}$ to $2.0\ \mu\text{m}$, and the holding time was chosen to span from 1 s to 180 s. For each combination, three points on the same hydrogel surface were tested. The data acquisition rate was above 500 Hz.

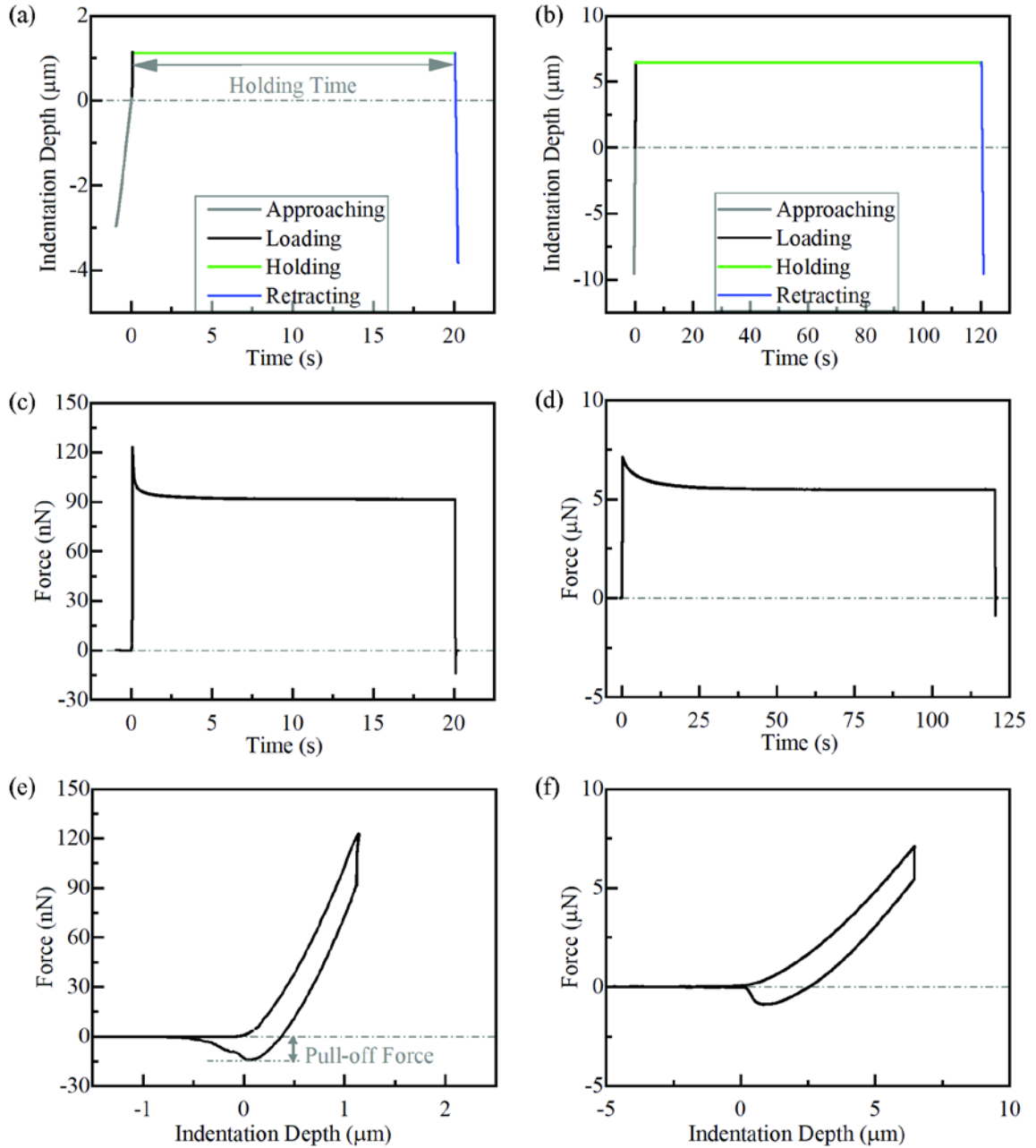


Figure 5.1 Illustration of the indentation depth-time relation in (a) an AFM test and (b) a microindenter test. Result of the contact force-time relation from (c) an AFM test and (d) a microindenter test. Result of the force-indentation depth relation from (e) an AFM test and (f) a microindenter test.

5.2.3 *Indentation Adhesion Experiment on Microindenter*

Indentation adhesion tests with the indenter of the larger radius were conducted on a microindenter (Femtools, FT-MTA03 Micromechanical Testing and Assembly System). A polystyrene sphere with a radius of 200 μm was glued to the end of the force probe with a force range of 2000 μN using epoxy glue. The hydrogel sample was prepared following the same method as that for the AFM test. Throughout the test, both the hydrogel and the indenter sphere were entirely submerged in water. The effect of the capillary force acting on the shaft of the force probe was calibrated and eliminated from the measurements. The details of the method follow the description in Chapter 4.

The experimental process is illustrated in Figure 5.1(b) as the displacement-time curve. During the test, the indenter was driven to approach the hydrogel surface at a speed of 25 $\mu\text{m/s}$, then held at a constant indentation depth for a preset amount of holding time, and then retracted at 25 $\mu\text{m/s}$. The contact force was measured throughout the test as functions of displacement and time, at a frequency of 3000 Hz. Examples of force data from the microindenter are illustrated in Figure 5.1(d) and Figure 5.1(f). On the microindenter, the indentation depth was chosen to span from 2 μm to 30 μm , and the holding time chosen as a series of values from 1 s to 180 s, which was the same with that for the AFM tests. Three points on the hydrogel surface were tested for each combination of holding time and indentation depth.

5.3 **Results and Discussion**

5.3.1 Force Response of Hydrogels in Indentation Adhesion Tests

Typical force curves from the indentation adhesion tests are shown in Figure 5.1, Figure 5.1(c) and Figure 5.1(e) for an AFM test, and Figure 5.1(d) and Figure 5.1(f) for a microindenter test, respectively. All the plots in Figure 5.1 are from hydrogel sample No.1. In general, the force curves observed for all the samples in this chapter have similar characteristics as the sample in Chapter 4. Figure 5.1(c) and Figure 5.1(d) show that immediately after loading, the contact force relaxes while the indentation depth was held constant. Comparing the force curve from the AFM test (Figure 5.1(c)) and from the microindenter test (Figure 5.1(d)), the time required for the contact force to reach constant is much longer with a larger indenter radius, i.e. a larger contact radius. This length dependence of the relaxation time indicates that poroelasticity is dominating the time-dependent bulk property of the hydrogels, which is expected for polyacrylamide hydrogels with high water concentration. Figure 5.1(e) and Figure 5.1(f) show that significant hysteresis exists between the loading and unloading force curve. During loading, no jump-in effect is observed, i.e. the contact force immediately increases upon contact without first jumping to a negative value, meaning that negligible adhesion exists before surface contact. During unloading, the contact force first decreases to zero, and then a pulling force appears.

For hydrogel samples studied in this chapter, the increase of adhesion over holding time is also observed from the increasing pull-off forces over the holding time. The pull-off forces as a function of holding time for the hydrogel samples are shown in detail in Figure 5.2, the error bars representing the standard deviation of the measurements from at least three points on the same sample. Also, the contact forces during holding maintain constant as predicted by the poroelasticity theory without including adhesion, as is shown

in Figure 5.1. The above observation holds for all the tests in this chapter, regardless of holding time, indentation depth, indenter radius, or hydrogel composition. These phenomena have been explained in Chapter 4: during the holding period, more monomers on the polymer chains adhere to the indenter, but only within the initial contact area, which does not affect the boundary condition of indentation during holding. Therefore, the contact force during holding is not affected by the increased adhesion, and the contact radius maintains the initial value predicted by the contact model without adhesion, i.e., the Hertzian contact model.

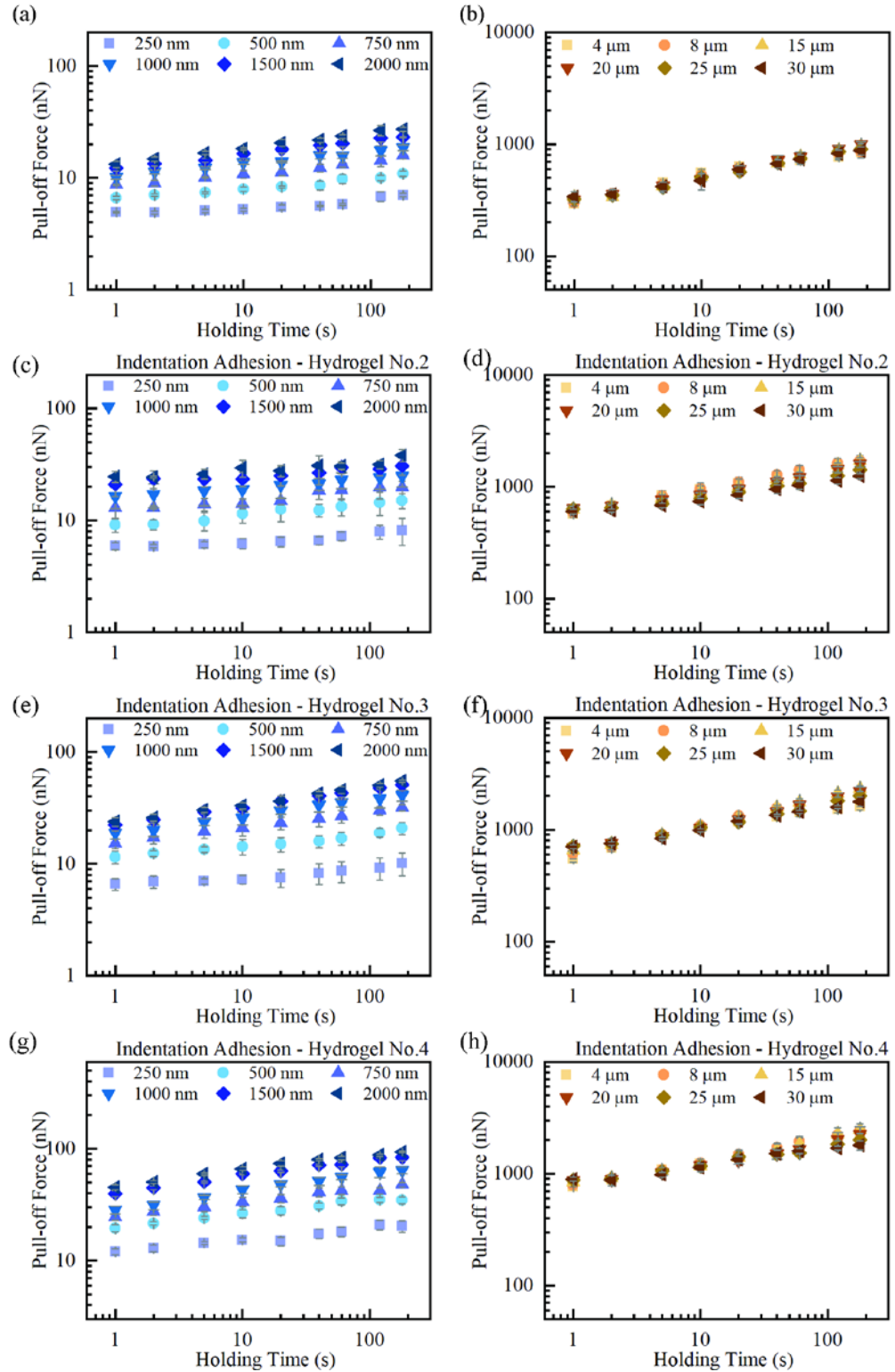


Figure 5.2 Illustration of the pull-off forces as functions of holding time at different indentation depths. (a) Results from the AFM tests. (b) Results from the microindenter tests.

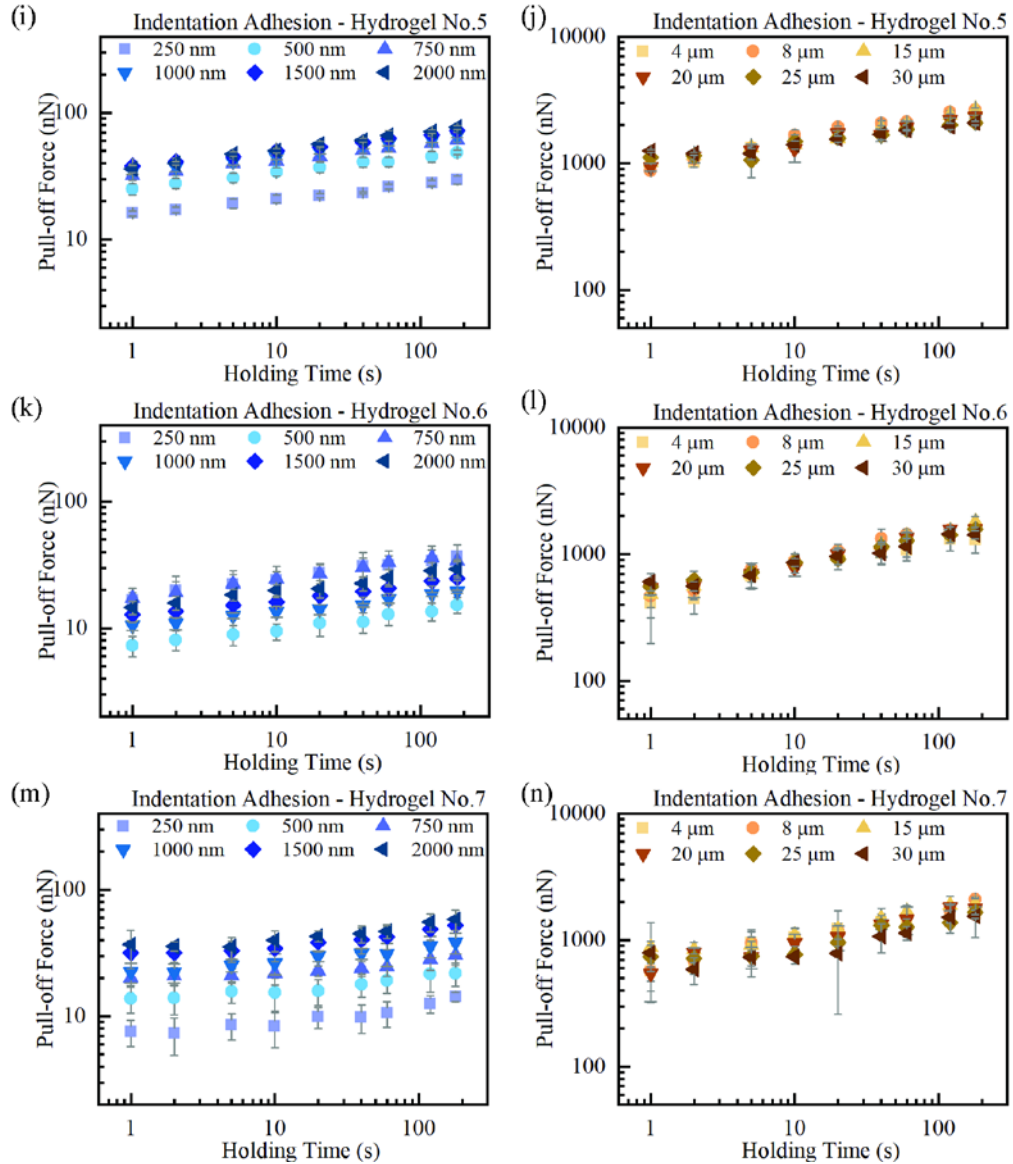


Figure 5.2 (Continued) Illustration of the pull-off forces as functions of holding time at different indentation depths. (a) Results from the AFM tests. (b) Results from the microindenter tests.

Figure 5.3 shows the results of pull-off forces for all the hydrogel samples as functions of the initial contact radius at different holding time, and colors from red to purple indicate data obtained from holding time of 1 s to 180 s. The data points with empty signs

are from the AFM tests, with relatively small initial contact radii. In this region, the pull-off force mostly increases both with the initial contact radius and with the holding time. The data points with filled signs are from the microindenter tests, with relatively large initial contact radii. In this region, most pull-off forces show a small range of increase first and mainly a plateau at larger contact radii. Hence, the trends of the pull-off force for all the hydrogel samples in the current chapter are the same as the observation in Chapter 4, thus also agree with the prediction of the modified Maugis-Dugdale model.

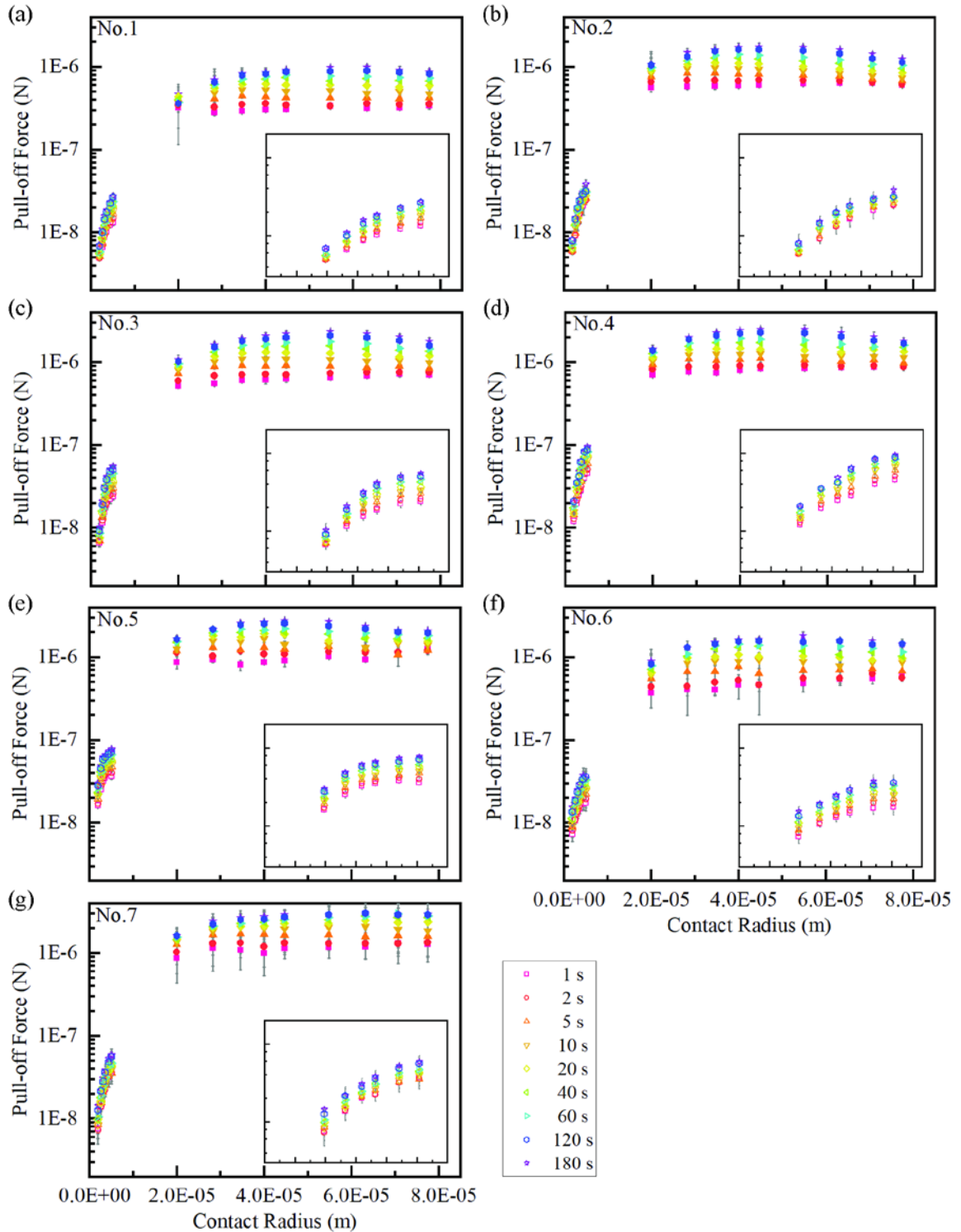


Figure 5.3 Illustration of the pull-off forces across different initial contact radii for the hydrogel samples. The empty signs are results from the AFM tests, and the full signs are results from the microindenter tests. Inserted figures show the results from the AFM tests with the zoomed-in x-axis.

The adhesion energy, cohesive strength and separation distance for each holding time can be obtained by comparing the pull-off forces across different initial contact radii with the theoretical prediction from the modified Maugis-Dugdale model. Figure 5.4 illustrates the experimental data and the fitting curves for hydrogel sample No.1 for three holding time: 2 s, 20 s and 120 s, using red, yellow, and blue color, respectively. In the modified Maugis-Dugdale model, the pull-off force still depends on the indenter radius. Therefore, two fitting curves are generated for the two indenter radii (the AFM and the microindenter), but with only one set of adhesion parameters for each holding time. Figure 5.4 shows that the modified Maugis-Dugdale model satisfyingly fit the experimental results. The adhesion parameters of other hydrogel samples and for different holding time are obtained through the same approach.

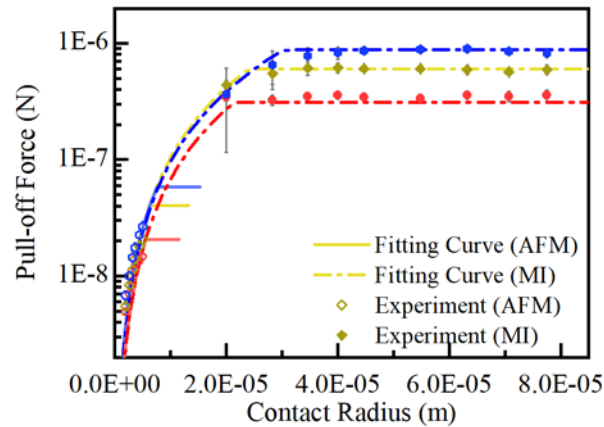


Figure 5.4 Illustration of curve fitting for holding time of 2 s (red), 20 s (yellow) and 120 s (blue) for hydrogel sample No.1.

5.3.2 Adhesion Parameters Obtained from the Modified Maugis-Dugdale Model

By fitting the modified Maugis-Dugdale model to the experimental data, the adhesion energy, cohesive strength, and separation distance of each hydrogel composition at each holding time are obtained. The adhesion parameters are illustrated in Figure 5.5 as functions of the holding time in log-log plots. The results for the two groups of hydrogels are plotted in two figures for clarity. For all the hydrogel samples, the values of the adhesion parameters increase with the holding time, and the increasing slopes, in the log-log plot, remain almost constant within the time range in the current study (180 s). Because the adhesion parameters are defined for a cohesive zone, they were assumed as independent of the bulk hydrogel properties when the modified model was developed. According to the time-dependence of these parameters, the possible influence from the hydrogel poroelasticity is also small: for the tests in the present study, the poroelastic force relaxation during holding is finished or almost finished within a contact time of 180 s. Therefore, the constant slopes indicate that adhesion keeps increasing even when the poroelastic force relaxation has finished, and there should exist an intrinsic time dependence for the increase of adhesion, which is independent of poroelasticity (e.g., the increase of polymer concentration due to solvent loss). The increasing slopes are also close across different hydrogel compositions, which suggests that the mechanism of the increasing adhesion over time may not be affected by the hydrogel composition.

Despite the similar time dependence for the increase of adhesion parameters, for hydrogels with different compositions, the magnitudes of the adhesion parameters differ. The relative magnitude of all the adhesion parameters between different compositions remains almost unchanged, which is briefly summarized as follows. For polyacrylamide

hydrogels prepared with the same initial monomer concentration (Figure 5.5(a), Figure 5.5(c), Figure 5.5(e)), both the adhesion energy and the cohesive strength increase with the initial mass concentration of the crosslinker, but the dependence of the separation distance on the initial mass concentration of the crosslinker is not very significant. For hydrogels with the fixed ratio of initial monomer concentration to the initial crosslinker concentration (Figure 5.5(b), Figure 5.5(d), Figure 5.5(f)), both the adhesion energy and the cohesive strength increase with the initial polymer concentration (monomer and crosslinker), but the separation distance decreases with the initial polymer concentration. Therefore, a primary conclusion from Figure 5.5 is that the adhesion parameters obtained through a more rigorous method still show dependence on the hydrogel composition, and the relative magnitude between different compositions does not change significantly with the same holding time.

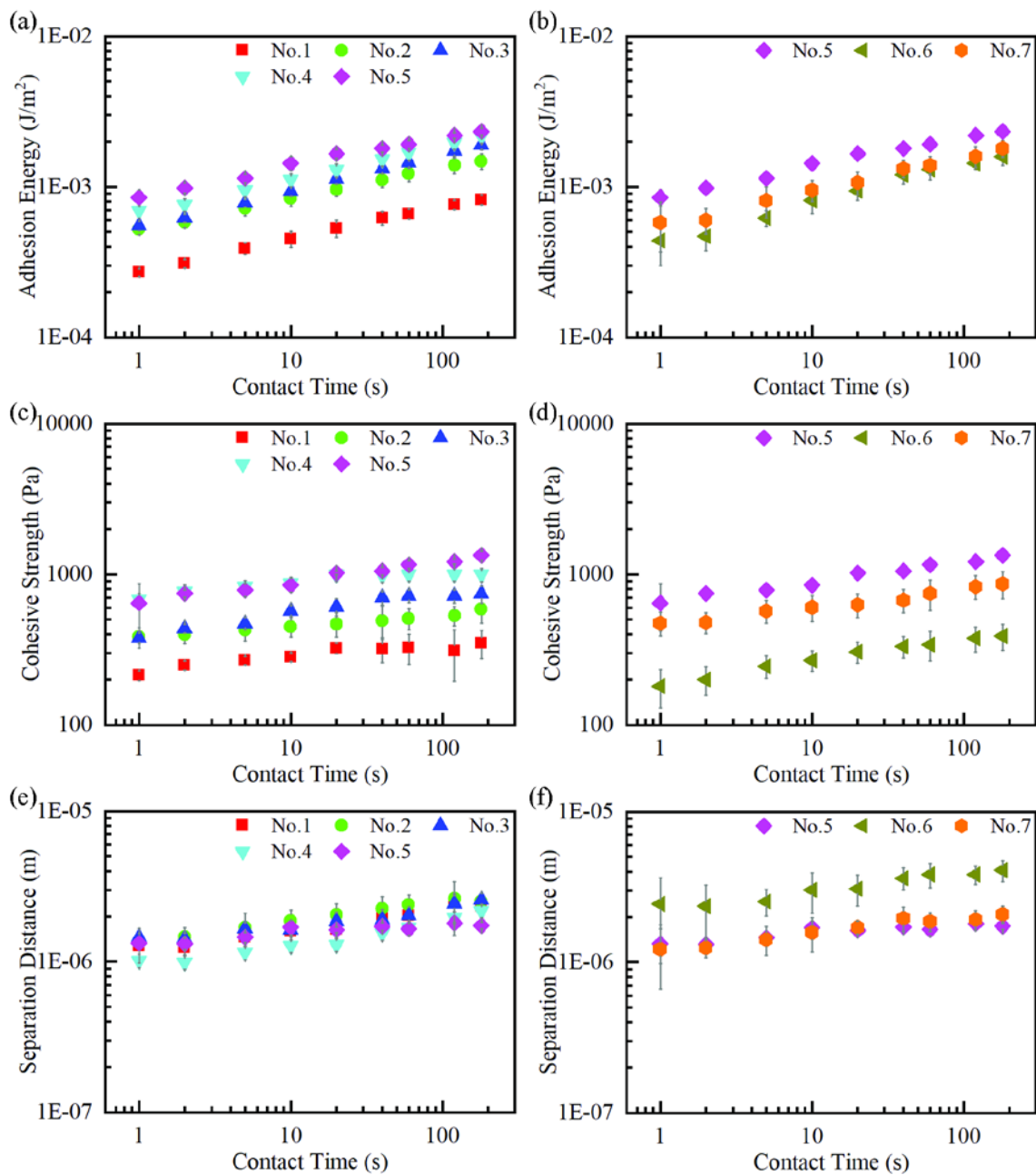


Figure 5.5 Adhesion energy versus holding time for (a) the first group of hydrogel samples and (b) the second group of hydrogel samples. Cohesive strength versus holding time for (c) the first group of hydrogel samples and (d) the second group of hydrogel samples. Separation distance versus holding time for (e) the first group of hydrogel samples and (f) the second group of hydrogel samples.

In previous studies, the polymer chains adhered to the opposite surface have been considered as the source of adhesion³¹, yet the study on the relation between the structural parameters of polymer chains and the adhesion properties has been limited by the interpretation of the experimental results. One of the goals of this Chapter is to revisit this problem. In the following, the possible relations between the three adhesion parameters and several structural parameters of the polymer chains will be discussed, including the polymer mass concentration at swelling equilibrium (equilibrium polymer concentration), the average surface chain density, and the average polymer chain length. The first two polymer chain parameters have been considered to influence the adhesion energy in the previous studies^{52,80,165,166}. The third parameter, the polymer chain length, will be compared with the separation distance, the adhesion parameter with a length unit. The relation of these two parameters has not been studied in previous literature.

The polymer mass concentration at equilibrium is obtained by dividing the mass of polymer in a sample by the mass of the sample in swelling equilibrium. The results are shown in Figure 5.6. In the first group (No.1 to No.5), the initial monomer mass concentration was fixed at 10%, and the initial crosslinker mass concentration increased from 0.1% to 0.5% for samples from No.1 to No.5. When reaching swelling equilibrium, the gels with less initial crosslinker concentration swell more, thus having a smaller polymer concentration. In the second group (No.6, No.7 and No.5), the ratio between the initial monomer mass concentration and the initial crosslinker mass concentration was fixed, and the initial monomer mass concentrations were 5%, 7.5% and 10% for sample No.6, No.7 and No.5, respectively. The three hydrogels in the second group swelled a similar amount from the prepared state to the equilibrium state, possibly because of the

lower crosslinking efficiency at lower initial polymer concentration^{153,167}. Therefore, the equilibrium polymer concentration for the second group covers a range close to that for the first group.

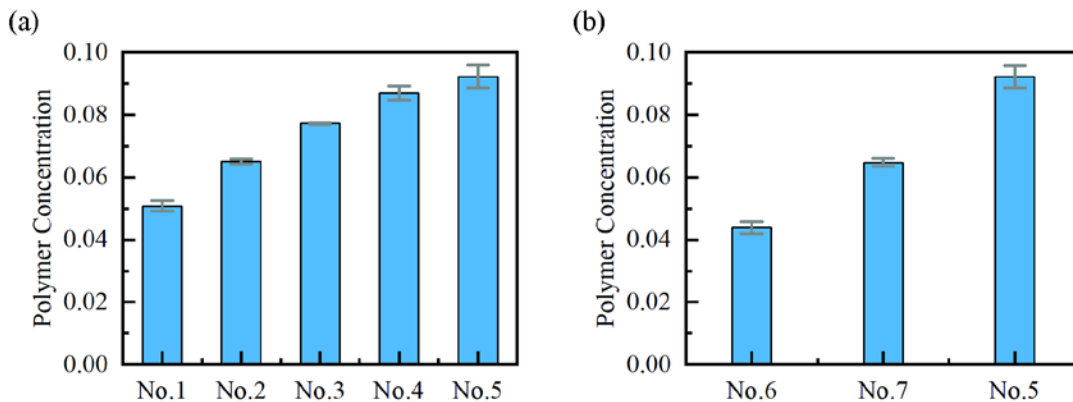


Figure 5.6 Mass concentration of polymer in the hydrogels after reaching swelling equilibrium in water. (a) The first group of hydrogels. (b) The second group of hydrogels.

The other structural parameters of the polymer chains, including the average surface chain density and the average length of the polymer chains, are not directly calculated from the hydrogel composition, i.e., by assuming all the monomers and crosslinkers form into an ideal and uniform network. This decision was made due to the consideration that polyacrylamide hydrogels are generated through the free-radical polymerization, during which a part of the crosslinker molecules does not participate in forming the cross-linked network^{153,154}. Therefore, in this study, the structural parameters of the polymer chains are estimated from the bulk mechanical properties measured from indentation by applying the

Flory-Rehner model^{111,168}. As has been discussed in Chapter 3, the shear modulus of the hydrogel with high water concentration can still be simply related to the polymer chain density in the material. Although the Flory-Rehner model cannot describe the linear poroelastic parameters in a large range of swelling ratio, the analysis of the modified model proves that the shear modulus of hydrogels with high solvent concentration is only related to the crosslinker density and topological constraints, the latter is treated as a type of effective crosslinkers in the previous studies^{148,169}. The calculation of the structural parameters will be introduced along with the discussion on the adhesion parameters. In the following subsections, the possible relation between the adhesion parameters and the structural parameters of the polymer chains will be discussed based on the results for holding time of 180 s. According to the time dependence of the adhesion parameters presented before, the results from the other holding time should lead to the same conclusion.

5.3.2.1 Adhesion Energy

Hydrogel adhesion is considered to result from the adhesive interaction between the polymer chains on a hydrogel surface and the opposite surface. Therefore, measurements of hydrogel adhesion have been related to several parameters of the polymer chains, including the equilibrium polymer concentration and the surface chain density^{52,80,165,166}. However, it was still not clear whether one of these parameters alone can determine the adhesion energy. It was also not clear whether any one of these parameters is related to the increase of adhesion over time. In the current work, the first question can be answered by studying the adhesion of hydrogels with different combinations of monomers and

crosslinkers, but with a similar range of polymer concentration or surface chain density at equilibrium.

In Figure 5.7(a), the results of the adhesion energy of the two groups of hydrogel samples for holding time of 180 s are plotted against their polymer concentration at equilibrium, the first group of hydrogels represented by blue squares and second group represented by orange circles. As is shown in Figure 5.7(a), the adhesion energy increases with the equilibrium polymer concentration for each group of hydrogels. However, for the first group of hydrogels, the increasing slope is larger. For the second group of hydrogels, the slope is smaller. The two groups of hydrogels combined do not show a consistent dependence on the equilibrium polymer concentration, suggesting that the equilibrium polymer concentration alone could not determine the adhesion energy at a specific holding time.

The surface chain density of a hydrogel under swelling equilibrium is estimated from the bulk polymer chain density using the relation $s = N^{2/3}/\lambda_{SR}^2$, where N is the bulk polymer chain density and is estimated following the Flory-Rehner model^{63,112}, $N = G\lambda_{SR}/k_B T$, where G is the shear modulus of the swollen gel calculated by fitting the loading force curve with the Hertzian contact model, λ_{SR} is the linear swelling ratio of the hydrogel, k_B is the Boltzmann constant and T is the absolute temperature. Here it is assumed that the structural parameters of the polymer chains on the hydrogel surface, e.g. the polymer chain density, are close to that in the bulk when using the method described in the experimental section. It has been reported in previous literature that hydrogels formed in a

closed cell with surfaces made by flat hydrophilic materials (e.g. glass) tend to have uniform polymer chain parameters from the bulk to the surface^{163,164}.

In Figure 5.7(b), the results of the adhesion energy of all the hydrogel samples for holding time of 180 s are plotted against the surface chain density. Similar to the relation with the equilibrium polymer concentration, the adhesion energy increases with the surface chain density for each group of hydrogels, but the dependence does not hold for the two groups of results combined. Therefore, the surface chain density alone could not determine the adhesion energy at a specific holding time either. The adhesion energy, as defined in the modified model, is the product of the cohesive strength and the separation distance, each of them may be related to different aspects of the surface polymer chains. Therefore, in the following section, the possible relation between these two adhesion parameters and the structural parameters of the polymer chains will be discussed separately.

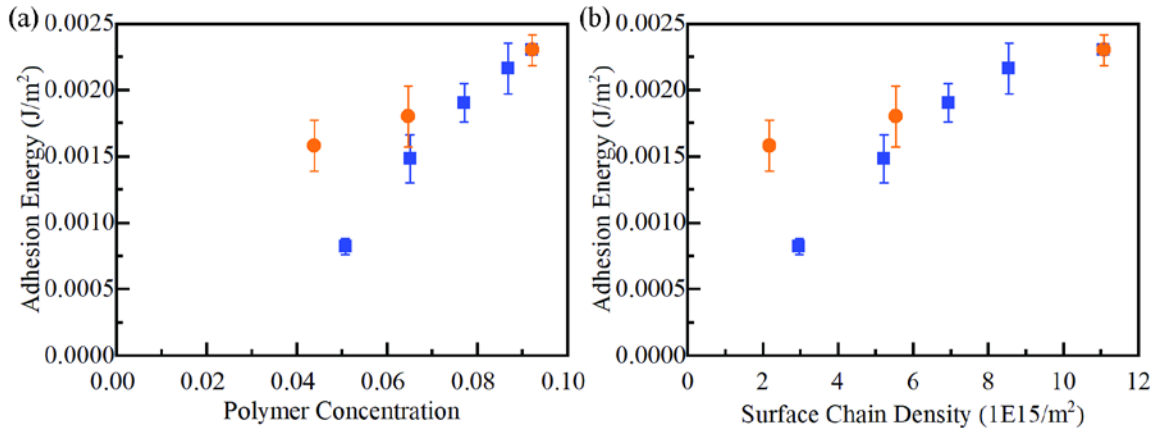


Figure 5.7 (a) Adhesion energy versus polymer concentration at equilibrium. (b) Adhesion energy versus surface chain density. Results are from the holding time of 180s.

5.3.2.2 Cohesive Strength

The cohesive strength obtained from the modified Maugis-Dugdale model refers to the force required to separate two adhered surfaces per unit area, i.e., the force needed to detach the adhered polymer chains per unit area. The relations between the cohesive strength and the two structural parameters of polymer chains, the equilibrium polymer concentration and the surface chain density, are also examined, using the two plots in Figure 5.8. In Figure 5.8(a), the cohesive strength increases with the polymer concentration for both groups of data. Different from the trend for the adhesion energy, the data of the two groups of hydrogels roughly fall onto the same curve. In Figure 5.8(b), the results of cohesive strength also roughly fall onto the same curve as a function of the surface chain density. Figure 5.8(b) further shows that the cohesive strength is almost proportional to the surface chain density. For all the hydrogel samples in the current study, their equilibrium polymer concentrations all increase with their surface chain density, which might explain the overlapping of the two groups of data in both Figure 5.8(a) and Figure 5.8(b). Still, the proportional relation in Figure 5.8(b) suggests that each surface polymer chain, on average, may require the same amount of pulling force to detach from the indenter surface, at the same amount of holding time.

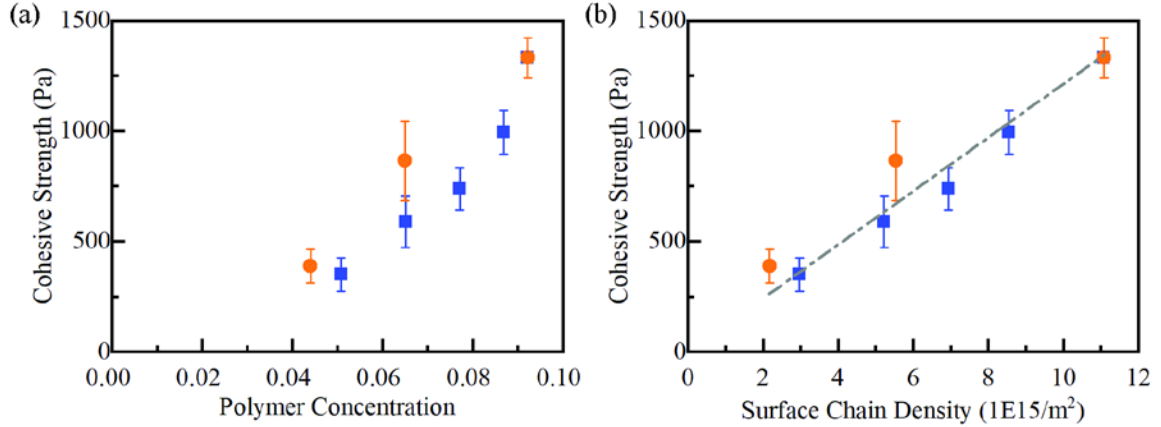


Figure 5.8 (a) Cohesive strength versus polymer concentration at equilibrium. (b) Cohesive strength versus surface chain density. Results are from the holding time of 180s.

5.3.2.3 Separation Distance

In the modified model, the separation distance refers to the length within which the two surfaces still have adhesive interaction. In the case of hydrogel adhesion, it was assumed that a finite separation distance exists because the surface polymer chains can extend to a longer distance. Therefore, it is expected that the separation distance is related to the deformed length of a polymer chain upon surface separation. To examine this assumption, in this subsection, the separation distance calculated using the modified model is compared with two estimated lengths of the surface polymer chain: the average polymer chain size and the straightened chain length.

The average polymer chain size refers to the size of a polymer chain without pulling force on its two ends. It is estimated using the equation $l_f = \sqrt{C_\infty \cdot 2 \cdot n} l_{cb}$, where $C_\infty = 8.5$ is the Flory's characteristic ratio of polyacrylamide chains¹⁷⁰, $l_{cb} = 0.154$ nm is the

length of the carbon-carbon bond in the polymer chain, and n is the average number of monomers per polymer chain estimated as $n = N_A \rho_{polymer} M / N$.⁶³ Here $\rho_{polymer}$ is the density of dry polymer, M is the molar mass of the monomer acrylamide, N is the bulk polymer chain density and N_A is the Avogadro constant. The estimation of n assumes that all the monomers participates in forming the polymer network¹⁶⁷. When a polymer chain is pulled using a small force, the deformation is also on the scale of l_f . The straightened chain length, on the other hand, refers to the length of a polymer chain when it is pulled using a large force so that the polymer chain is nearly fully straightened. It is estimated as $l_s = n l_{cb} \cos(\theta/2)$, where $\theta = 68^\circ$ is the angle between neighboring carbon bonds⁶³. Both the average chain size and the straightened chain length are measures of the length of a polymer chain, but it is expected that comparing the separation distance with both parameters could further evaluate the physics picture proposed for the separation distance.

In Figure 5.9, the separation distances of the hydrogels are plotted against the average chain size (Figure 5.9(a)) and the straightened chain length (Figure 5.9(b)). The two plots show that the separation distance obtained roughly increases with the average chain size or the straightened chain length, suggesting that the separation distance is related to the polymer chain length. However, the magnitude of the separation distance is larger than both of the chain length parameters. Because polyacrylamide hydrogels are prepared through free-radical polymerization, there is a distribution of the polymer chain lengths¹⁷¹⁻¹⁷³. In the adhesion tests, the longer polymer chains on the surface may be extended further and contribute more to the results of the separation distance. Another possible reason is that more complex energy dissipation mechanisms exist in the cohesive zone, which is reflected in the larger value of the separation distance. A further discussion on the

mechanism of the additional energy dissipation is beyond the scope of the current study. However, the discussion on the cohesive strength and the separation distance provides more information on explaining why the surface chain density (or equilibrium polymer concentration) alone does not predict the adhesion energy of a hydrogel. The adhesion energy may be related to not only the surface chain density but also other factors.

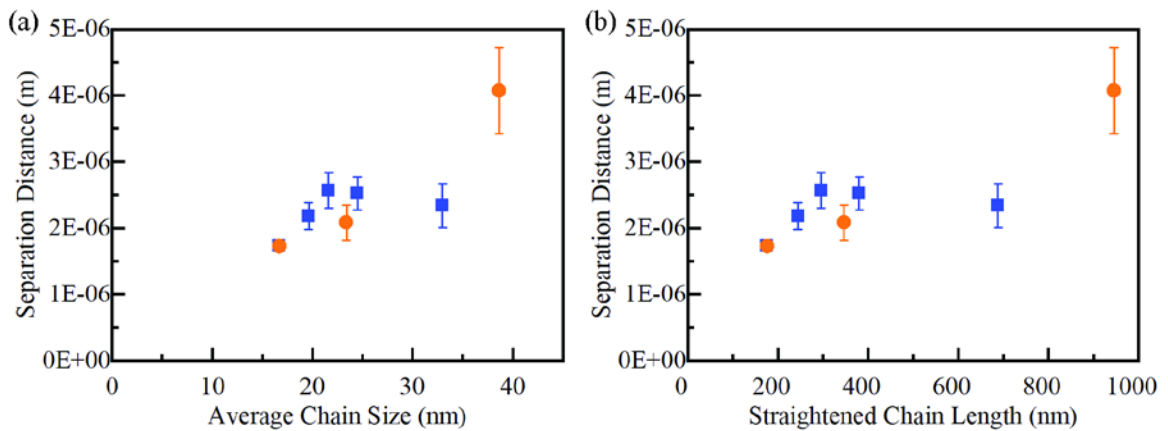


Figure 5.9 (a) Separation distance versus the average chain size. (b) Separation distance versus the straightened chain length. Results are from the holding time of 180 s.

5.3.2.4 Time Dependence of Hydrogel Adhesion

According to Figure 5.5, both the cohesive strength and the separation distance increase with the holding time with an almost constant slope in the log-log plots for all the hydrogel samples, and the value for the slope is similar across different hydrogel compositions. This subsection proposes an explanation of the time-dependence of the adhesion parameters based on the general theory of polymer physics⁶³. The corresponding

schematics are illustrated in Figure 5.10. For simplicity, Figure 5.10 only focuses on the adhering and detaching of one surface polymer chain, i.e., the mechanism on the microscale. The deformation process of the entire polymer network should follow the discussion on the contact mechanics problem on the macroscale in Chapter 4.

Before contact, the surface polymer chains are in the stress-free state. Figure 5.10(a) plots the condition of a polymer chain before contact with the yellow, dashed circle illustrating the shape. Upon loading, the indenter is pressed onto the hydrogel surface. As is shown by Figure 5.10(b), surface polymer chains are not highly compressed but roughly deforms with a similar scale with the bulk deformation, i.e., with a relatively small compressive strain caused by shallow indentation. Therefore, only a few monomers on a polymer chain form adhesive contact with the indenter immediately after loading, each monomer adhered onto the indenter surface referred to as an adhesive site in the following text. On the other hand, a long polyacrylamide polymer chain may have many monomers adhered to the indenter gradually over time. Because the surface polymer chains have one end attached to the polymer network, the monomers closer to the indenter surface tends to form the adhesive sites first upon contact. The monomers closer to the initially adhered monomers are also more likely to further adhere to the indenter (Figure 5.10(c)). When the holding time increases, more monomers adhere to the indenter surface, but all near the initial monomers forming the adhesive sites (Figure 5.10(e)).

The same process is expected for all the polymer chains on the hydrogel surface. In previous literature, the process of a free polymer chain forming attachments with a flat surface in solution has been studied. It has been reported that monomers gradually adhere to the flat surface over time, and the time of reaching equilibrium is related to the material

chemistry as well as the polymer chain length^{174–176}. However, similar research has not been conducted on hydrogels. For hydrogels in the current study, the average number of monomers per polymer chain is as high as around 1000. Therefore, the initial increasing rate of the adhered monomers may not be sensitive to the entire polymer chain length. In the current study, the values of the adhesion parameters do not reach a plateau within the first 180 s for any hydrogel compositions.

As has been discussed in the previous subsection, to relate the increase of adhered monomers to the increase of adhesion parameters over time, a detailed mechanism is needed. However, some discussion on the relative magnitude of the adhesion parameters between different hydrogel compositions can be carried out using some simple assumptions on the deformation of the surface polymer chains. For a polymer chain, the average number of monomers that can immediately form contact with the indenter can be estimated using the equation⁶³: $m_c = \left[\frac{n}{(4/3)\pi R_p^3} \right] \cdot \left[b_0 \cdot \pi \left(R_p^2 - (R_p - b_0)^2 \right) \right]$. This estimation assumes that the surface polymer chain is spherical with a radius of R_p , so that R_p scales with \sqrt{n} . The first part in the equation refers to the number density of monomers per unit volume in this polymer chain sphere. Assuming a monomer can only form adhesive contact with the indenter when its distance with the indenter surface is less than a small value b_0 , the second term in the expression of m_c gives an estimation of the volume of the space in which the monomers can form adhesive sites after contact. Considering $b_0 \ll R_p$, the second term would scale with R_p . As a result, m_c is independent of n , the average number of monomers per chain. This estimation still holds when the polymer chain is compressed slightly due to shallow indentation. According to this estimation, each surface polymer chain on average

would form almost the same number of adhesive sites immediately after contact, regardless of the polymer chain length.

Upon unloading, the polymer chain in direct contact with the indenter is stretched until the force in the polymer chain is large enough to overcome the adhesion between the attached monomers and the indenter. If the monomers attached to the indenter are all located closely on a surface polymer chain, these monomers may separate from the indenter surface almost simultaneously at an unloading speed as high as 25 $\mu\text{m/s}$ in the current study¹⁷⁷. With this assumption, the same polymer chain needs to extend longer to pull more monomers away from the indenter surface. See the difference between Figure 5.10(c) (d) and Figure 5.10(e) (f). For polymer chains with different chain lengths, the same amount of force is needed to detach the same number of adhered monomers in average, but different amount of chain deformation is needed to achieve this pulling force depending on the chain length, i.e., depending on the chain elasticity. As a result, the magnitude of cohesive strength only depends on the surface chain density apart from the holding time, and its increasing rate over time is almost independent of the polymer chain parameters. This explanation also agrees with the similar increasing rate of the separation distance and the cohesive strength over time. Nevertheless, more studies are needed to examine the assumptions made in this subsection, so that the detailed physics picture of the hydrogel adhesion can be determined on the microscale.

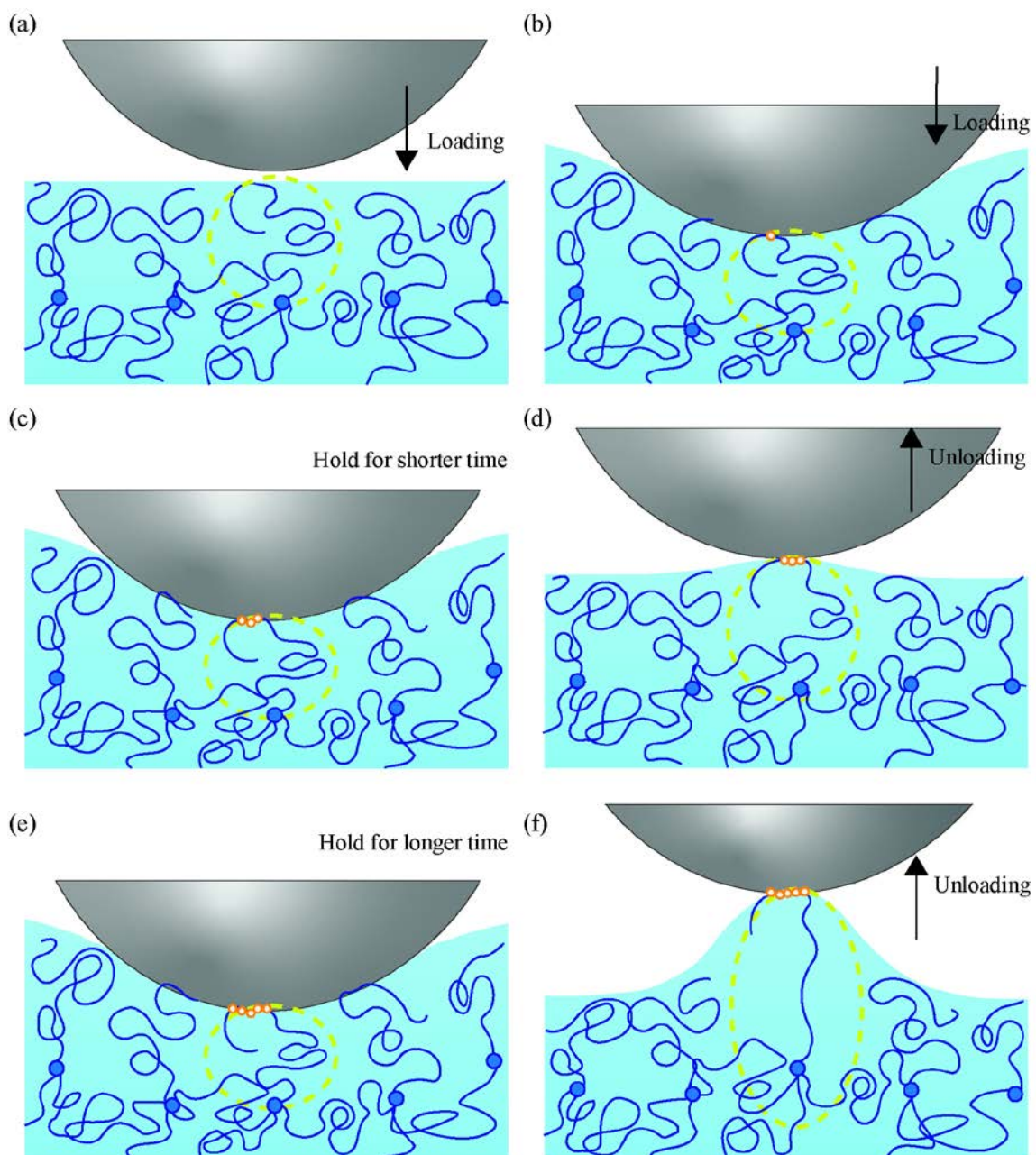


Figure 5.10 Mechanism of hydrogel adhesion at the length scale of a single polymer chain. The gray semi-sphere represents the indenter surface. The dark blue chains are polymer chains, the dark blue circles are crosslinkers, the orange circles represent monomers that are in adhesive contact with the indenter surface. The yellow dashed circles illustrate the deformation of the surface polymer chain. (a) Before contact, the polymer chain on the hydrogel surface is in a stress-free state. (b) Upon contact, the entire polymer chain deforms following the bulk compressive strain, only a few monomers in close contact with the indenter can form adhesive sites. (c) After relatively short holding time, some monomers close to the initial adhesive sites form

adhesive contact with the indenter. (d) Upon unloading, the polymer chain is stretched to pull off the adhered monomers. (e) After a longer holding time, more monomers close to the initial adhesive sites form adhesive contact with the indenter. (f) When unloading after longer holding time, the polymer chain is stretched more to pull off more adhered monomers.

5.4 Conclusion

In the current study, three adhesion parameters of polyacrylamide hydrogels with different compositions are measured, including the adhesion energy, the cohesive strength, and the separation distance. The adhesion measurements are obtained from a series of indentation adhesion tests over a wide range of holding time and contact radius, and the adhesion parameters are calculated with a modified Maugis-Dugdale model. Through this approach, the adhesion parameters obtained are intrinsic parameters of the hydrogel surface and independent of the experimental length scales, thus allowing the comparison between the adhesion properties among different hydrogel compositions. To further understand the relation between hydrogel adhesion and its composition, the possible relations of these adhesion parameters with some structural parameters of the surface polymer chains are discussed. It is found out that rather than the adhesion energy, the cohesive strength scales better with the surface polymer chain density. Meanwhile, the adhesion energy is related to the surface chain density along with other properties of the surface polymer chains, which are likely related to the polymer chain length. All the adhesion parameters increase with the holding time in the current study, and a detailed mechanism for this observation is proposed.

CHAPTER 6. CONCLUSIONS

The main purpose of this thesis is to develop robust indentation methods to characterize the mechanical, transport and adhesion properties of hydrogels, especially on a small length scale. The indentation methods developed are further applied to the model polyacrylamide hydrogel of several different compositions to study their properties.

In Chapter 2, a dynamic indentation method is developed that can characterize the linear poroelastic properties of hydrogels. The experimental procedure of conducting the dynamic indentation method is proposed, and the corresponding boundary value problem is solved. Based on the solution, a simple procedure to extract the linear poroelastic parameters from experimental results is suggested. This method is further applied to the polyacrylamide hydrogel to illustrate the procedure, but it is expected that the method can be applied on a wide range of natural and synthetic hydrogels as long as a proper contact length scale is selected. When using the method on other hydrogels, it is suggested that the tests be conducted on a series of different contact radii to confirm the poroelastic nature of the hydrogel under that specific length and frequency scale.

In Chapter 3, the applicability of the dynamic indentation method is illustrated on polyacrylamide hydrogels with different compositions and at different swelling ratios. The swelling-dependent mechanical and transport properties of polyacrylamide hydrogels are studied. Analysis of the experimental results shows that the Flory-Rehner model is not able to describe hydrogels with a large range of swelling ratio only with constant parameters. This finding indicates that the applicability of the widely used Flory-Rehner model on other types of hydrogels also needs to be further examined, as some possible mechanisms

causing the discrepancy may be universal for different hydrogels. This chapter also proposes and studies possible modifications to the Flory-Rehner model. The modified model can describe the swelling-dependent linear poroelastic properties of polyacrylamide hydrogels of several different compositions, it may also serve as a reference for developing nonlinear models for other hydrogels.

In Chapter 4, the time dependence and length dependence of adhesion during indentation is first systematically examined on a model hydrogel. Several findings are obtained from the experimental results, which may apply to a wider range of hydrogels. First, the adhesion of hydrogel increases with the contact time, and the timescale for the increase is not related to the poroelasticity, which causes the time and length-dependent bulk mechanical properties. Second, the adhesion of hydrogel also depends on contact length scales, which is later proved to be a result of the adhesion hysteresis. The latter finding, for the first time, shows the importance of both the indenter radius and the indentation depth when measuring the adhesion of any hydrogels at a small length scale, and points out that the classical contact mechanics model may not be directly used to extract values of adhesion energy. Based on the experimental observations, this chapter further develops a modified contact mechanics model that can predict the length-dependent adhesion behavior of hydrogels using one set of adhesion parameters at a particular holding time, which is not covered by previous contact mechanics models. It is expected that the modified model can serve as a robust tool for comparing adhesion measurements on different hydrogels, and even at different experimental length scales.

In Chapter 5, the indentation adhesion method developed in Chapter 4 is applied to polyacrylamide hydrogels with different compositions to study their adhesion properties.

The possible relation between the adhesion parameters and several parameters of the polymer chains in the hydrogel are discussed, which suggests more detailed information on the mechanism of hydrogel adhesion. Although more experimental information about the polymeric network is needed to further study the adhesion properties of hydrogels, the discussion on the possible mechanism is expected to provide more guidance for tuning the hydrogel adhesion through controlling the hydrogel composition, for both the polyacrylamide hydrogel and a wider range of synthetic hydrogels.

APPENDIX A. EXPERIMENTAL DATA

A.1 Phase Lag Degree Results for Dynamic Indentation Tests

For each hydrogel composition at each swelling ratio, the results of the phase lag degree obtained at different indentation depths are plotted in different colors, either as a function of the oscillation frequency or as a function of the frequency times the contact radius squared. The composition number of the hydrogel sample and the concentration of the PEG solution are labeled in each plot.

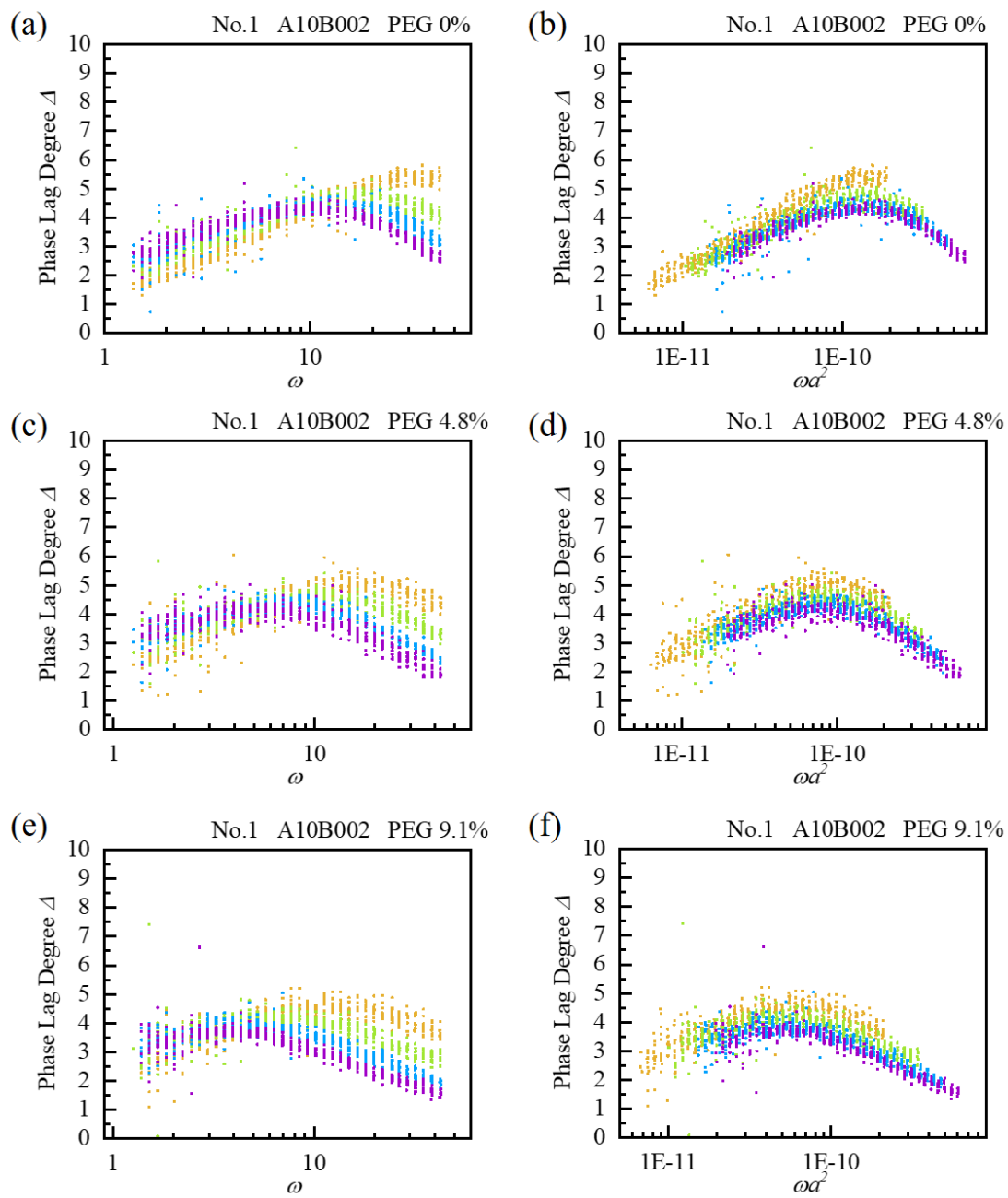


Figure A. 1 Phase lag degree results for hydrogel composition No.1.

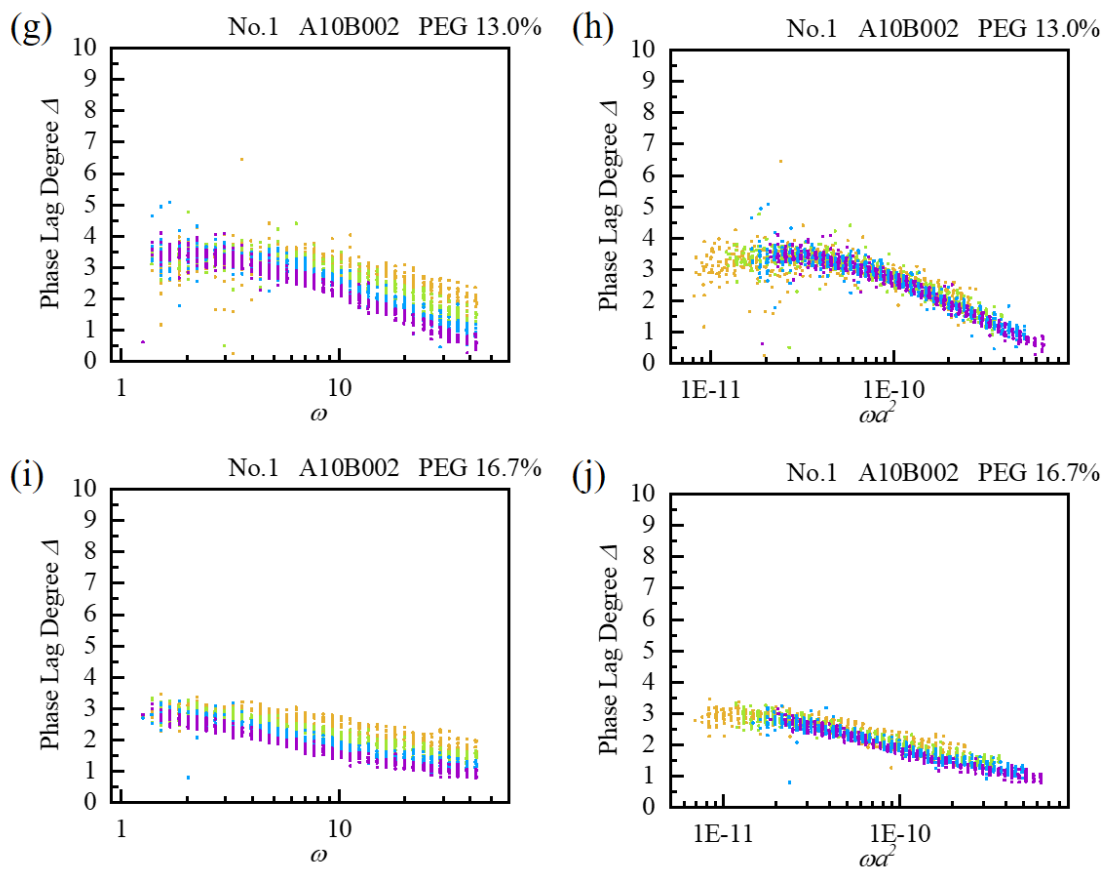


Figure A. 1 (Continued) Phase lag degree results for hydrogel composition No.1.

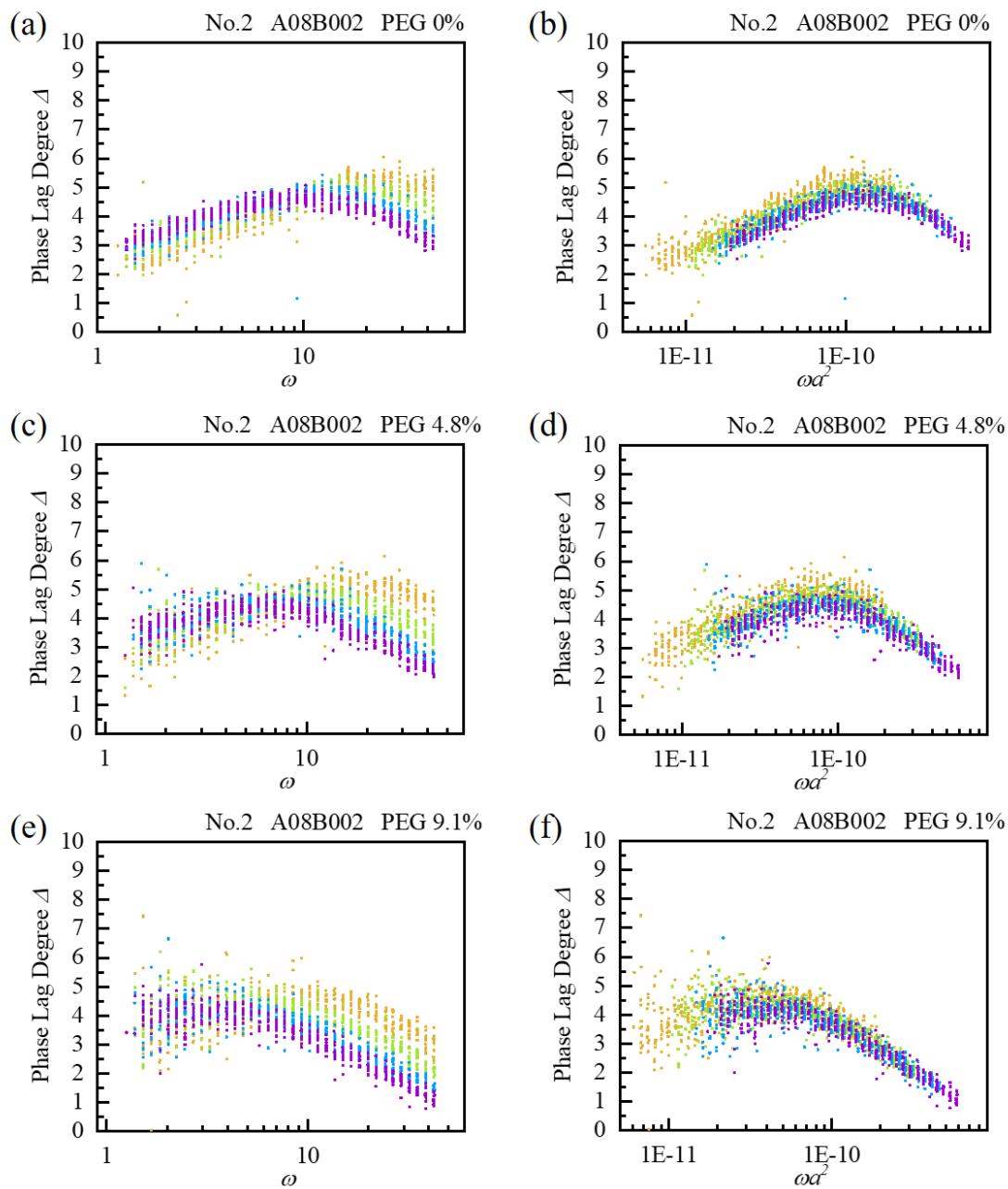


Figure A. 2 Phase lag degree results for hydrogel composition No.2.

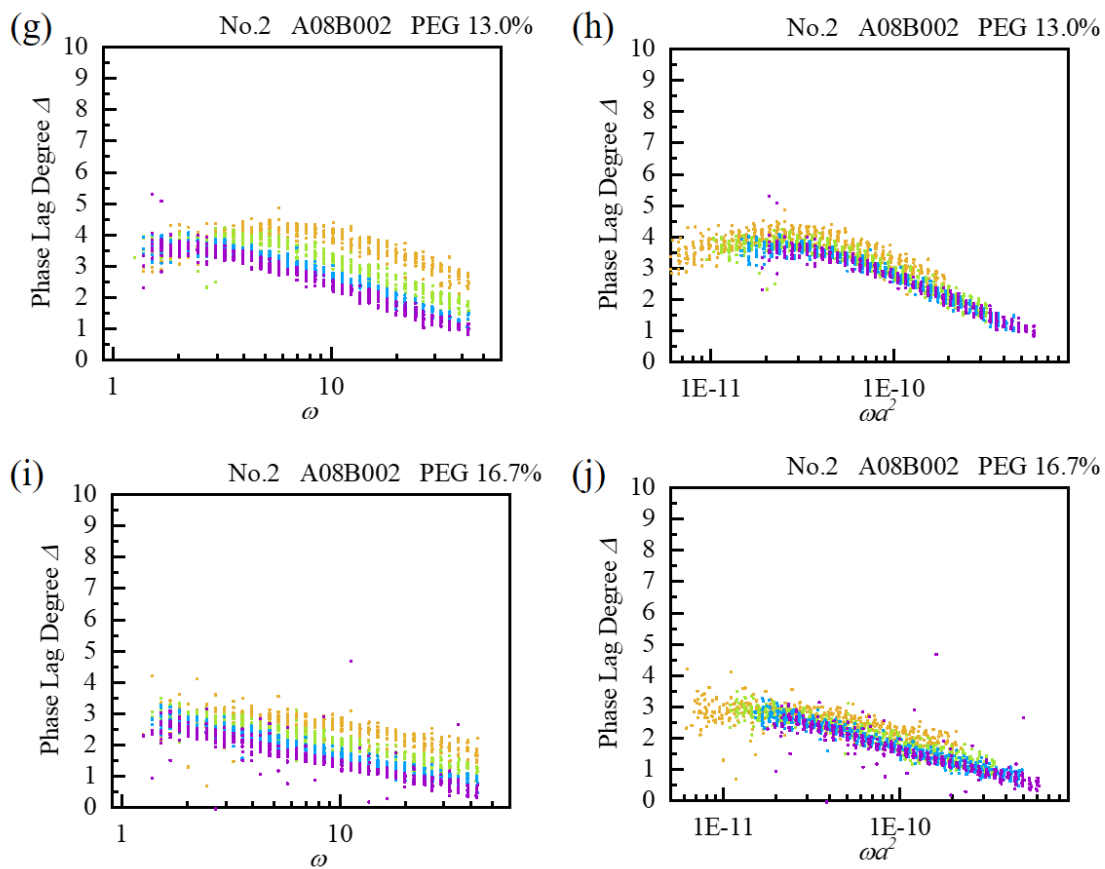


Figure A. 2 (Continued) Phase lag degree results for hydrogel composition No.2.

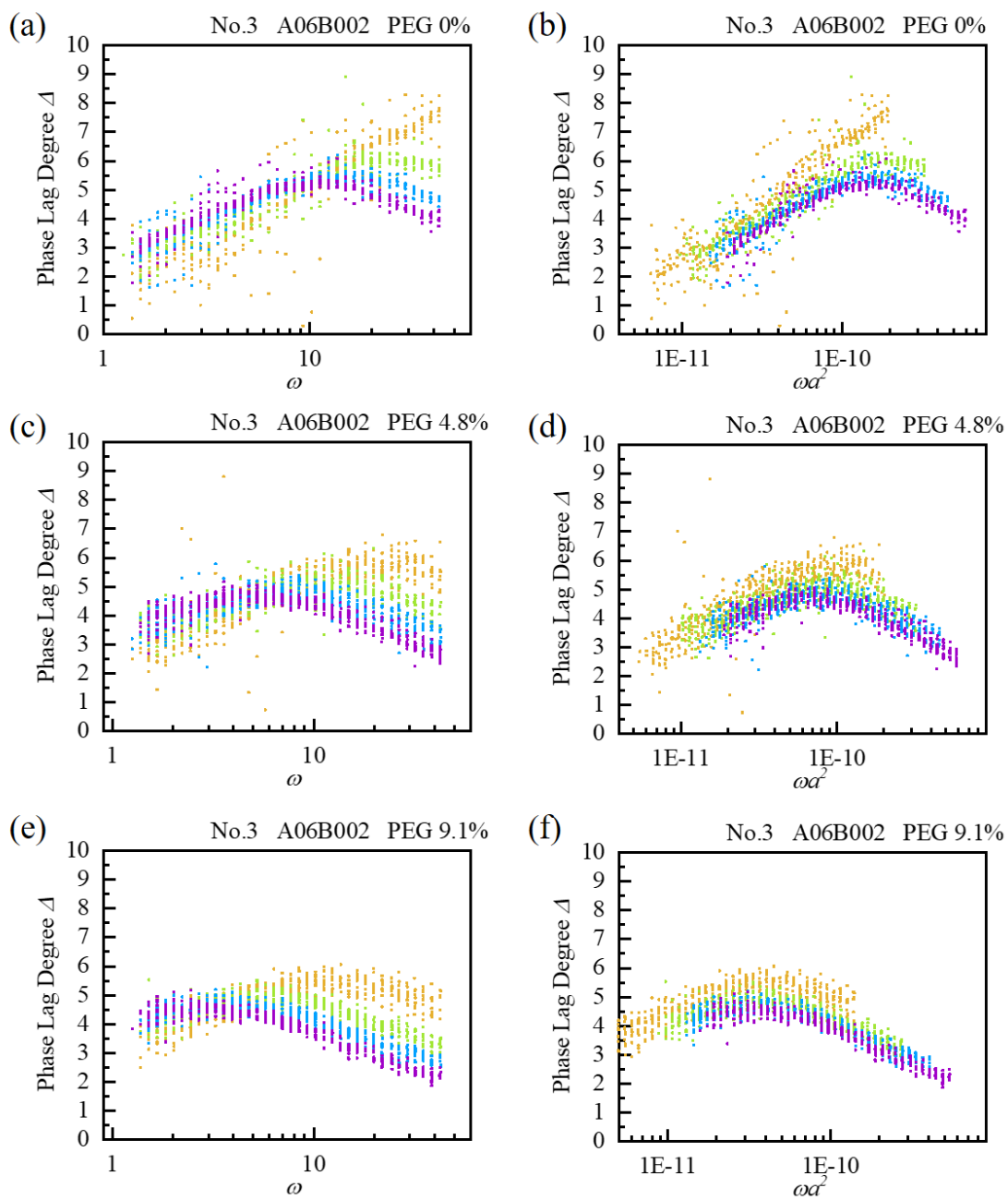


Figure A.3 Phase lag degree results for hydrogel composition No.3.

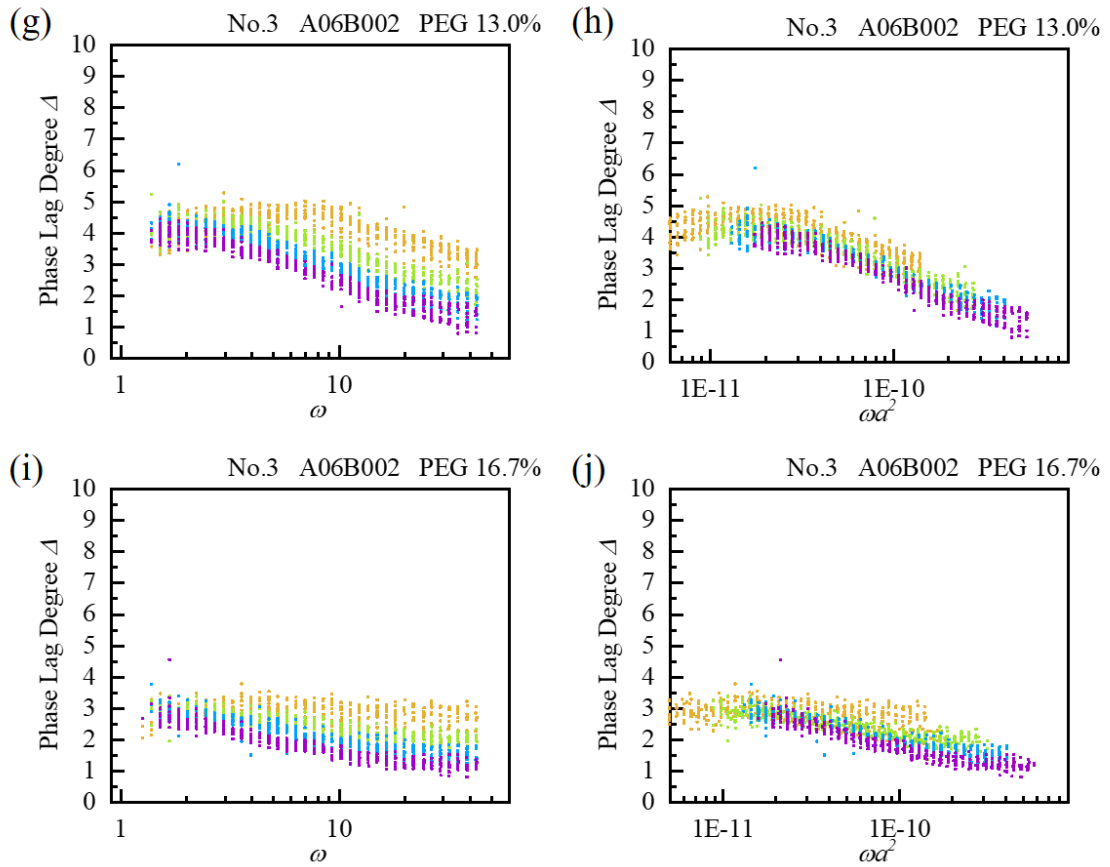


Figure A. 3 (Continued) Phase lag degree results for hydrogel composition No.3.

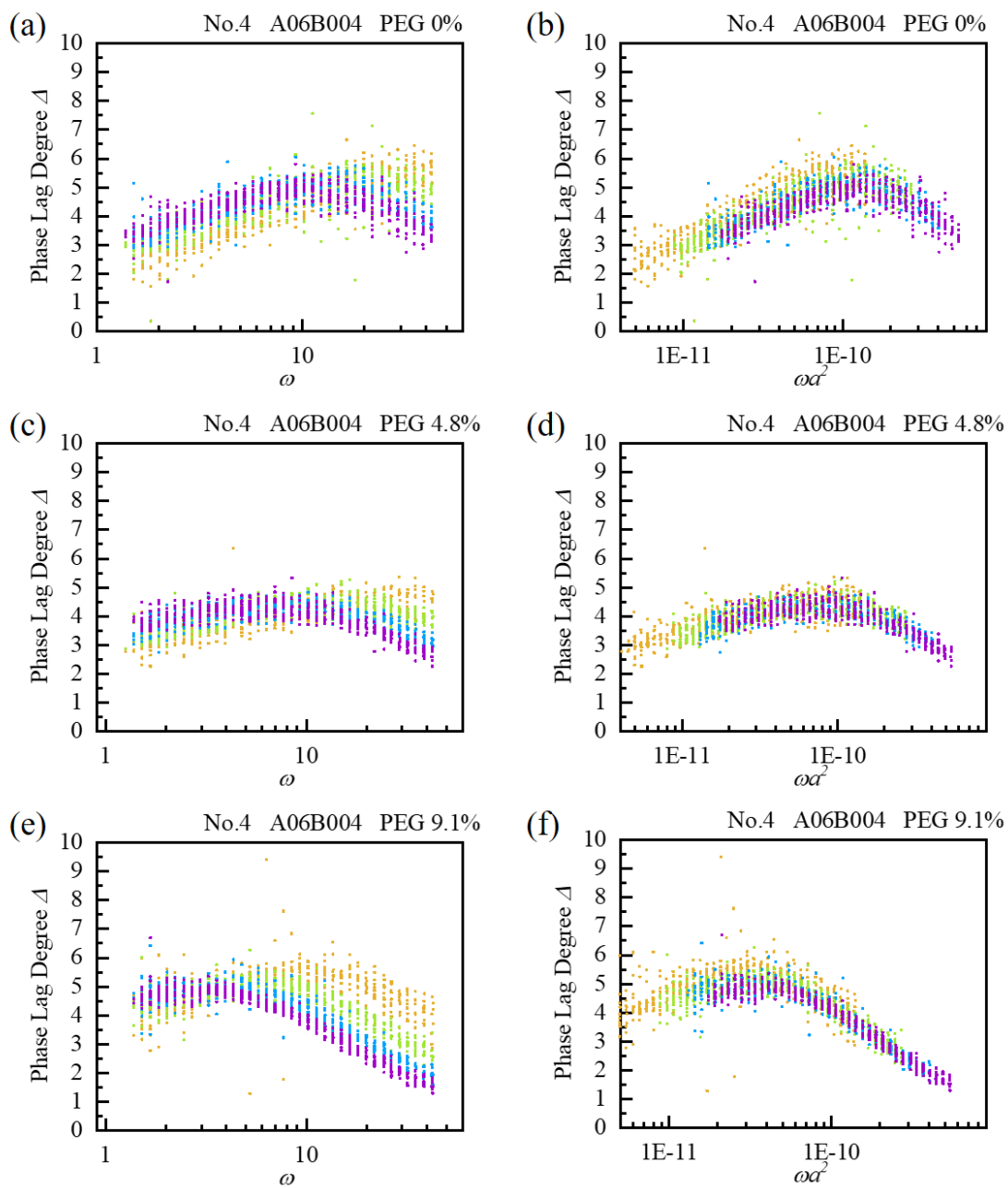


Figure A. 4 Phase lag degree results for hydrogel composition No.4.

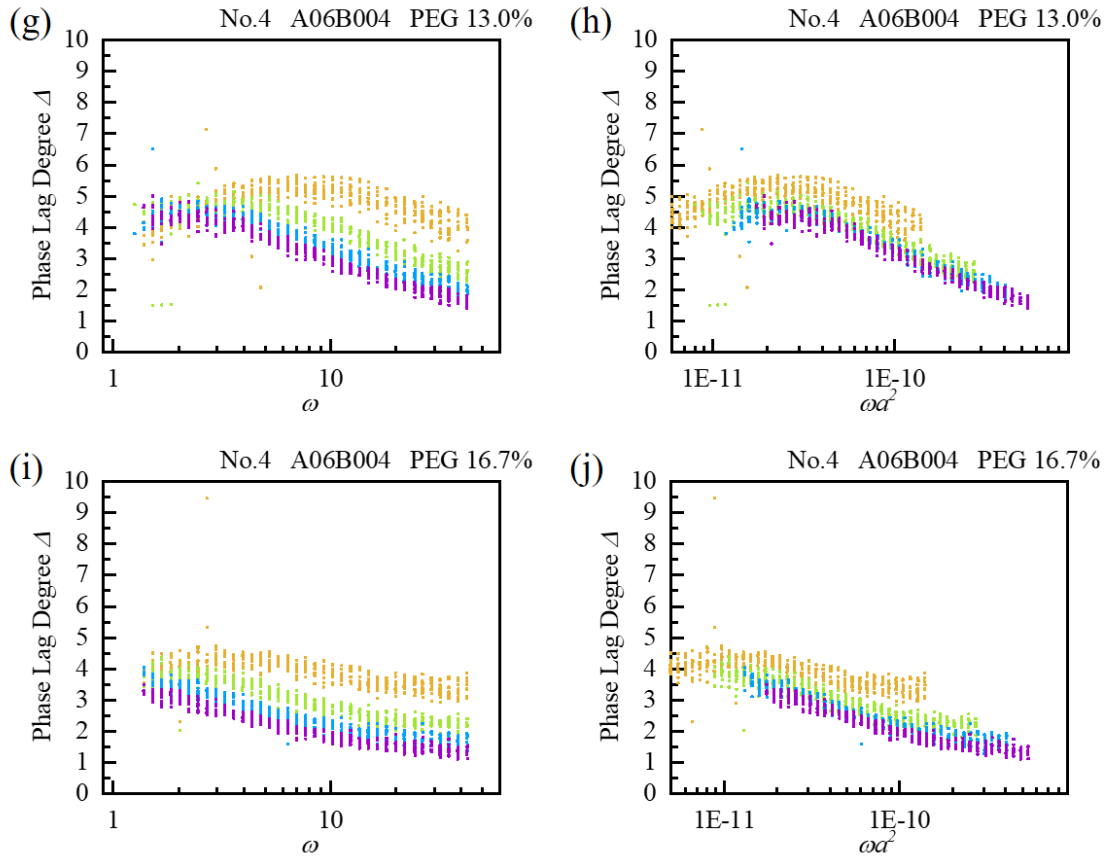


Figure A. 4 (Continued) Phase lag degree results for hydrogel composition No.4.

A.2 Calculating the Shear Moduli of Hydrogel Samples in Chapter 5

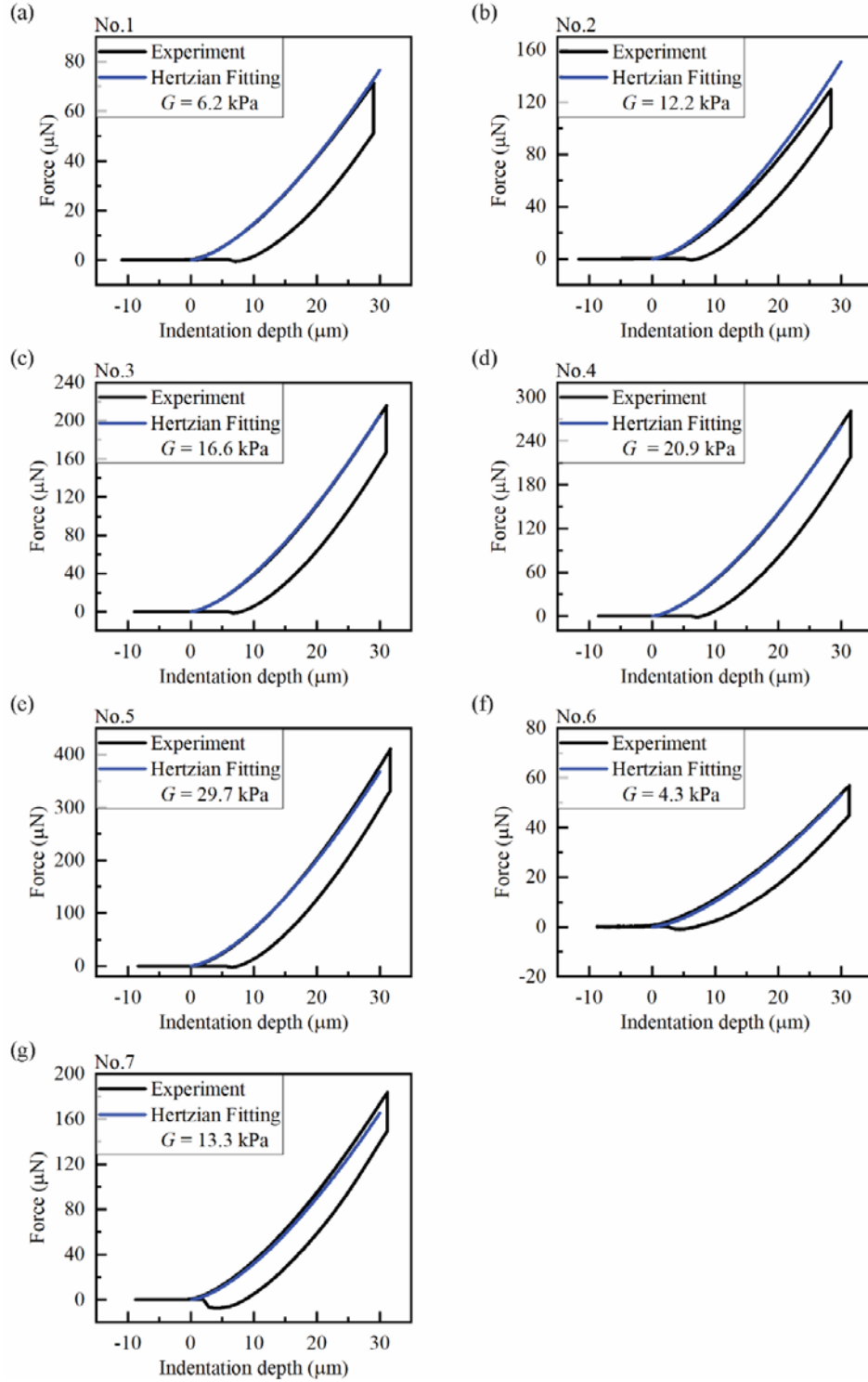


Figure A.5 Fitting curves for calculating the shear moduli of hydrogel samples.

REFERENCES

1. Samsom, M. *et al.* In vitro friction testing of contact lenses and human ocular tissues: Effect of proteoglycan 4 (PRG4). *Tribol. Int.* **89**, 27–33 (2015).
2. Morel, V. & Quinn, T. M. Cartilage injury by ramp compression near the gel diffusion rate. *J. Orthop. Res.* **22**, 145–151 (2004).
3. Lai, S. K., Wang, Y. Y., Wirtz, D. & Hanes, J. Micro- and macrorheology of mucus. *Adv. Drug Deliv. Rev.* **61**, 86–100 (2009).
4. Mehrabian, A. & Abousleiman, Y. General solutions to poroviscoelastic model of hydrocephalic human brain tissue. *J. Theor. Biol.* **291**, 105–118 (2011).
5. Budday, S. *et al.* Mechanical properties of gray and white matter brain tissue by indentation. *J. Mech. Behav. Biomed. Mater.* **46**, 318–330 (2015).
6. Chung, J. Y., Regev, I. & Mahadevan, L. Spontaneous exfoliation of a drying gel. *Soft Matter* **12**, 7855–7862 (2016).
7. Hall-Stoodley, L., Costerton, J. W. & Stoodley, P. Bacterial biofilms: From the natural environment to infectious diseases. *Nat. Rev. Microbiol.* **2**, 95–108 (2004).
8. Peppas, N. A., Bures, P., Leobandung, W. & Ichikawab, H. Hydrogels in pharmaceutical formulations. *Eur. J. Pharm. Biopharm.* **50**, 27–46 (2000).
9. Opdahl, A., Kim, S. H., Koffas, T. S., Marmo, C. & Somorjai, G. A. Surface mechanical properties of pHEMA contact lenses: Viscoelastic and adhesive property changes on exposure to controlled humidity. *J. Biomed. Mater. Res. - Part A* **67**, 350–356 (2003).
10. Han, S., Opdahl, A., Marmo, C. & Somorjai, G. A. AFM and SFG studies of pHEMA-based hydrogel contact lens surfaces in saline solution: adhesion, friction, and the presence of non-crosslinked polymer chains at the surface. *Biomaterials* **23**, 1657–1666 (2002).
11. Jeong, B., Bae, Y. H., Lee, D. S. & Kim, S. W. Biodegradable block copolymers as

- injectable drug-delivery systems. *Nature* **388**, 860–862 (1997).
12. Qiu, Y. & Park, K. Environment-sensitive hydrogels for drug delivery. *Advanced Drug Delivery Reviews* **64**, 49–60 (2012).
 13. Hoare, T. R. & Kohane, D. S. Hydrogels in drug delivery : Progress and challenges *. *Polym. with aligned carbon Nanotub. Act. Compos. Mater.* **49**, 1993–2007 (2008).
 14. You, J. O. & Auguste, D. T. Nanocarrier cross-linking density and pH sensitivity regulate intracellular gene transfer. *Nano Lett.* **9**, 4467–4473 (2009).
 15. Jen, A. C., Wake, M. C. & Mikos, A. G. Review: Hydrogels for cell immobilization. *Biotechnology and Bioengineering* **50**, 357–364 (1996).
 16. Drury, J. L. & Mooney, D. J. Hydrogels for tissue engineering: scaffold design variables and applications. *Biomaterials* **24**, 4337–51 (2003).
 17. Feksa, L. R. *et al.* Hydrogels for biomedical applications. in *Nanostructures for the Engineering of Cells, Tissues and Organs: From Design to Applications* **54**, 403–438 (2018).
 18. Buenger, D., Topuz, F. & Groll, J. Hydrogels in sensing applications. *Progress in Polymer Science* **37**, 1678–1719 (2012).
 19. Gerlach, G. *et al.* Chemical and pH sensors based on the swelling behavior of hydrogels. *Sensors Actuators, B Chem.* **111–112**, 555–561 (2005).
 20. Richter, A., Klatt, S., Paschew, G. & Klenke, C. Micropumps operated by swelling and shrinking of temperature-sensitive hydrogels. *Lab Chip* **9**, 613–618 (2009).
 21. Bassil, M., Davenas, J. & EL Tahchi, M. Electrochemical properties and actuation mechanisms of polyacrylamide hydrogel for artificial muscle application. *Sensors Actuators, B Chem.* **134**, 496–501 (2008).
 22. Keplinger, C. *et al.* Stretchable, Transparent, Ionic Conductors. *Science (80-.).* **341**, 984–987 (2013).

23. Maeda, S., Hara, Y., Sakai, T., Yoshida, R. & Hashimoto, S. Self-walking gel. *Adv. Mater.* **19**, 3480–3484 (2007).
24. Chen, Z. *et al.* A three-dimensionally interconnected carbon nanotube-conducting polymer hydrogel network for high-performance flexible battery electrodes. *Adv. Energy Mater.* **4**, 1–10 (2014).
25. Lin, S. *et al.* Stretchable Hydrogel Electronics and Devices. *Adv. Mater.* **28**, 4497–4505 (2016).
26. Khalili, A. A. & Ahmad, M. R. A Review of cell adhesion studies for biomedical and biological applications. *International Journal of Molecular Sciences* **16**, 18149–18184 (2015).
27. Flemming, H. C. & Wingender, J. The biofilm matrix. *Nat. Rev. Microbiol.* **8**, 623 (2010).
28. Coles, J. M. *et al.* In situ friction measurement on murine cartilage by atomic force microscopy. *J. Biomech.* **41**, 541–548 (2008).
29. Yang, J., Bai, R. & Suo, Z. Topological Adhesion of Wet Materials. *Adv. Mater.* **30**, 1–7 (2018).
30. Zhang, T., Yuk, H., Lin, S., Parada, G. A. & Zhao, X. Tough and tunable adhesion of hydrogels: experiments and models. *Acta Mech. Sin. Xuebao* **33**, 543–554 (2017).
31. Bradley, L. C. *et al.* Rough Adhesive Hydrogels (RAd gels) for Underwater Adhesion. *ACS Appl. Mater. Interfaces* **9**, 27409–27413 (2017).
32. Johnson, B. D., Beebe, D. J. & Crone, W. C. Effects of swelling on the mechanical properties of a pH-sensitive hydrogel for use in microfluidic devices. *Mater. Sci. Eng. C* **24**, 575–581 (2004).
33. Miller, K. & Chinzei, K. Mechanical properties of brain tissue in tension. *J. Biomech.* **35**, 483–490 (2002).
34. Cai, S., Hu, Y., Zhao, X. & Suo, Z. Poroelasticity of a covalently crosslinked alginate hydrogel under compression. *J. Appl. Phys.* **108**, (2010).

35. Stammen, J. A., Williams, S., Ku, D. N. & Guldberg, R. E. Mechanical properties of a novel PVA hydrogel in shear and unconfined compression. *Biomaterials* **22**, 799–806 (2001).
36. Miller, K. Method of testing very soft biological tissues in compression. *J. Biomech.* **38**, 153–158 (2005).
37. Armstrong, C. G., Lai, W. M. & Mow, V. C. An Analysis of the Unconfined Compression of Articular Cartilage. *J. Biomech. Eng.* **106**, 165–173 (1984).
38. Zhang, X., Hu, Z. & Li, Y. Bending of bi-gels. *J. Chem. Phys.* **105**, 3794–3800 (1996).
39. Scherer, G. W. Measuring permeability of rigid materials by a beam-bending method: III, cement paste. *J. Am. Ceram. Soc.* **83**, 2231–2239 (2000).
40. Hu, Y., Zhao, X., Vlassak, J. J. & Suo, Z. Using indentation to characterize the poroelasticity of gels. *Appl. Phys. Lett.* **96**, 2009–2011 (2010).
41. Kalcioğlu, Z. I., Mahmoodian, R., Hu, Y., Suo, Z. & Van Vliet, K. J. From macro- to microscale poroelastic characterization of polymeric hydrogels via indentation. *Soft Matter* **8**, 3393–3398 (2012).
42. Pharr, G. M. An improved technique for determining hardness and elastic modulus using load and displacement sensing indentation experiments. *J. Mater. Res.* **7**, 1564–1583 (1992).
43. Hu, Y., Chen, X., Whitesides, G. M., Vlassak, J. J. & Suo, Z. Indentation of polydimethylsiloxane submerged in organic solvents. *J. Mater. Res.* **26**, 785–795 (2011).
44. Ebenstein, D. M. & Wahl, K. J. A comparison of JKR-based methods to analyze quasi-static and dynamic indentation force curves. *J. Colloid Interface Sci.* **298**, 652–662 (2006).
45. Z. Ilke Kalcioğlu, Mahmoodian, R., Hu, Y., Suo, Z. & Vliet, K. J. Van. From macro- to microscale poroelastic characterization of polymeric hydrogels via indentation †. *Soft Matter* **8**, 3393–3398 (2012).

46. Nia, H. T. *et al.* High-Bandwidth AFM-Based Rheology Reveals that Cartilage is Most Sensitive to High Loading Rates at Early Stages of Impairment. *Biophysj* **104**, 1529–1537 (2013).
47. Han, L. *et al.* Time-Dependent Nanomechanics of Cartilage. *Biophysj* **100**, 1846–1854 (2011).
48. Luque, T. *et al.* Acta Biomaterialia Local micromechanical properties of decellularized lung scaffolds measured with atomic force microscopy. *Acta Biomater.* **9**, 6852–6859 (2013).
49. Sudre, G., Olanier, L., Tran, Y., Hourdet, D. & Creton, C. Reversible adhesion between a hydrogel and a polymer brush. *Soft Matter* **8**, 8184–8193 (2012).
50. Guvendiren, M., Messersmith, P. B. & Shull, K. R. Self-assembly and adhesion of DOPA-modified methacrylic triblock hydrogels. *Biomacromolecules* **9**, 122–128 (2008).
51. Efremov, Y. M., Bagrov, D. V, Kirpichnikov, M. P. & Shaitan, K. V. Application of the Johnson – Kendall – Roberts model in AFM-based mechanical measurements on cells and gel. *Colloids Surfaces B Biointerfaces* **134**, 131–139 (2015).
52. Nalam, P. C., Gosvami, N. N., Caporizzo, M. A., Composto, R. J. & Carpick, R. W. Nano-rheology of hydrogels using direct drive force modulation atomic force microscopy. *Soft Matter* **11**, 8165–8178 (2015).
53. Gent, A. N. & Petrich., R. P. Adhesion of Viscoelastic Materials to Rigid Substrates. *Proc. R. Soc. London. Ser. A, Math. Phys.* **310**, 433–448 (1969).
54. She, H., Malotky, D. & Chaudhury, M. K. Estimation of Adhesion Hysteresis at Polymer/Oxide Interfaces Using Rolling Contact Mechanics. *Langmuir* **14**, 3090–3100 (1998).
55. Ghatak, A., Vorvolakos, K., She, H., Malotky, D. L. & Chaudhury, M. K. Interfacial Rate Processes in Adhesion and Friction. *J. Phys. Chem. B* **104**, 4018–4030 (2000).
56. Israelachvili, J. N. *Intermolecular and surface forces.* (Academic press, 2015).

57. Sneddon, I. N. The relation between load and penetration in the axisymmetric boussinesq problem for a punch of arbitrary profile. *Int. J. Eng. Sci.* **3**, 47–57 (1965).
58. Johnson, K. L. *Contact Mechanics*. (Cambridge University Press, 1985). doi:DOI: 10.1017/CBO9781139171731
59. Rattan, S., Li, L., Lau, H. K., Crosby, A. J. & Kiick, K. L. Micromechanical characterization of soft, biopolymeric hydrogels: Stiffness, resilience, and failure. *Soft Matter* **14**, 3478–3489 (2018).
60. Tong, K. J. & Ebenstein, D. M. Comparison of Spherical and Flat Tips for Indentation of Hydrogels. *JOM* **67**, 713–719 (2015).
61. Zhu, X., Siamantouras, E., Liu, K. K. & Liu, X. Determination of work of adhesion of biological cell under AFM bead indentation. *J. Mech. Behav. Biomed. Mater.* **56**, 77–86 (2016).
62. Christ, A. F. *et al.* Mechanical difference between white and gray matter in the rat cerebellum measured by scanning force microscopy. *J. Biomech.* **43**, 2986–2992 (2010).
63. Rubinstein, M. & Colby, R. H. *Polymer physics*. (New York: Oxford university press., 2003).
64. Biot, M. A. General theory of three-dimensional consolidation. *J. Appl. Phys.* **12**, 155–164 (1941).
65. Rice, J. R. & Cleary, M. P. Some basic stress diffusion solutions for fluid-saturated elastic porous media with compressible constituents. *Rev. Geophys. Sp. Phys.* **14**, (1976).
66. Hu, Y. & Suo, Z. Viscoelasticity and poroelasticity in elastomeric gels. *Acta Mech. Solida Sin.* **25**, 441–458 (2012).
67. Oyen, M. L. Mechanical characterisation of hydrogel materials. *Int. Mater. Rev.* **59**, 44–59 (2013).
68. Terzaghi, K. von. Die berechnung der durchlässigkeitsziffer des tones aus dem

- verlauf der hydrodynamischen spannungserscheinungen. *Sitzungsberichte der Akad. der Wissenschaften Wien, Math. Klasse, Abteilung IIa* **132**, 125–138 (1923).
69. Scherer, G. W. Drying gels. VIII. Revision and review. *J. Non. Cryst. Solids* **109**, 171–182 (1989).
 70. Hong, W., Zhao, X., Zhou, J. & Suo, Z. A theory of coupled diffusion and large deformation in polymeric gels. *J. Mech. Phys. Solids* **56**, 1779–1793 (2008).
 71. Galli, M., Comley, K. S. C., Shean, T. A. V. & Oyen, M. L. Viscoelastic and poroelastic mechanical characterization of hydrated gels. *J. Mater. Res.* **24**, 973–979 (2009).
 72. Li, L. P., Soulhat, J., Buschmann, M. D. & Shirazi-Adl, A. Nonlinear analysis of cartilage in unconfined ramp compression using a fibril reinforced poroelastic model. *Clin. Biomech.* **14**, 673–682 (1999).
 73. Nia, H. T., Han, L., Li, Y., Ortiz, C. & Grodzinsky, A. Poroelasticity of Cartilage at the Nanoscale. *Biophysj* **101**, 2304–2313 (2011).
 74. Nagashima, T., Tamaki, N., Matsumoto, S., Horwitz, B. & Seguchi, Y. Biomechanics of Hydrocephalus : A new theoretical model. *Neurosurgery* **21**, 898–904 (1987).
 75. Pena, A., Bolton, M. D., Whitehouse, H. & Pickard, J. D. Effects of brain ventricular shape on periventricular biomechanics: A finite-element analysis. *Neurosurgery* **45**, 107–118 (1999).
 76. Cheng, S. & Bilston, L. E. Unconfined compression of white matter. *J. Biomech.* **40**, 117–124 (2007).
 77. Tanaka, T. & Fillmore, D. J. Kinetics of swelling of gels. *J. Chem. Phys.* **70**, 1214–1218 (1979).
 78. Hui, C. Y., Lin, Y. Y., Chuang, F. U. C., Shull, K. R. & Lin, W. C. A contact mechanics method for characterizing the elastic properties and permeability of gels. *J. Polym. Sci. Part B Polym. Phys.* **44**, 359–370 (2006).

79. Lin, W. C., Shull, K. R., Hui, C. Y. & Lin, Y. Y. Contact measurement of internal fluid flow within poly(n- isopropylacrylamide) gels. *J. Chem. Phys.* **127**, (2007).
80. Macron, J., Bresson, B., Tran, Y., Hourdet, D. & Creton, C. Equilibrium and Out-of-Equilibrium Adherence of Hydrogels against Polymer Brushes. *Macromolecules* **51**, 7556–7566 (2018).
81. Johnson, K. L., Kendall, K. & Roberts, A. D. Surface energy and the contact of elastic solids. *Proc. R. Soc. Lond. A. Math. Phys. Sci.* **324**, 301–313 (1971).
82. Greenwood, J. A. & Johnson, K. L. The mechanics of adhesion of viscoelastic solids. *Philos. Mag. A Phys. Condens. Matter, Struct. Defects Mech. Prop.* **43**, 697–711 (1981).
83. Lin, Y. Y., Hui, C. Y. & Baney, J. M. Viscoelastic contract, work of adhesion and the JKR technique. *J. Phys. D. Appl. Phys.* **32**, 2250–2260 (1999).
84. Hui, C. & Baney, J. M. Contact Mechanics and Adhesion of Viscoelastic Spheres. *Langmuir* **14**, 6570–6578 (1998).
85. Kroner, E., Maboudian, R. & Arzt, E. Adhesion characteristics of pdms surfaces during repeated pull-off force measurements. *Adv. Eng. Mater.* **12**, 398–404 (2010).
86. Derjaguin, B. V., Muller, V. M. & Toporov, Y. P. Effect of Contact Deformations on the Adhesion of Particles. *J. Colloid Interface Sci.* **53**, 314–326 (1975).
87. Tabor, D. Surface Forces and Surface Interactions. *J. Colloid Interface Sci.* **58**, 2–13 (1977).
88. Maugis, D. Adhesion of Spheres : The JKR-DMT Transition Using a Dugdale Model. *J. Colloid Interface Sci.* **150**, (1992).
89. Silberzan, P., Perutz, S., Kramer, E. J. & Chaudhury, M. K. Study of the Self-Adhesion Hysteresis of a Siloxane Elastomer Using the JKR Method. *Langmuir* **10**, 2466–2470 (1994).
90. Pussak, D. *et al.* Specific Adhesion of Carbohydrate Hydrogel Particles in Competition with Multivalent Inhibitors Evaluated by AFM. *Langmuir* **30**, 6142–

6150 (2014).

91. Reale, E. R. & Dunn, A. C. Poroelasticity-driven lubrication in hydrogel interfaces. *Soft Matter* **13**, 428–435 (2017).
92. Caulfield, M. J., Qiao, G. G. & Solomon, D. H. Some aspects of the properties and degradation of polyacrylamides. *Chem. Rev.* **102**, 3067–3083 (2002).
93. Tse, J. R. & Engler, A. J. Preparation of hydrogel substrates with tunable mechanical properties. *Curr. Protoc. Cell Biol.* 1–16 (2010). doi:10.1002/0471143030.cb1016s47
94. Denisin, A. K. & Pruitt, B. L. Tuning the Range of Polyacrylamide Gel Stiffness for Mechanobiology Applications. *ACS Appl. Mater. Interfaces* **8**, 21893–21902 (2016).
95. Peters, A. & Candau, S. J. Kinetics of swelling of polyacrylamide gels. *Macromolecules* **19**, 1952–1955 (1986).
96. Li, Y. & Tanaka, T. Kinetics of swelling and shrinking of gels. *J. Chem. Phys.* **92**, 1365–1371 (1990).
97. Li, J., Hu, Y., Vlassak, J. J. & Suo, Z. Experimental determination of equations of state for ideal elastomeric gels. *Soft Matter* **8**, 8121–8128 (2012).
98. Yang, C., Yin, T. & Suo, Z. Polyacrylamide hydrogels. I. Network imperfection. *J. Mech. Phys. Solids* **131**, 43–55 (2019).
99. Tang, J., Li, J., Vlassak, J. J. & Suo, Z. Fatigue fracture of hydrogels. *Extrem. Mech. Lett.* **10**, 24–31 (2017).
100. Efremov, Y. M., Bagrov, D. V., Kirpichnikov, M. P. & Shaitan, K. V. Application of the Johnson-Kendall-Roberts model in AFM-based mechanical measurements on cells and gel. *Colloids Surfaces B Biointerfaces* **134**, 131–139 (2015).
101. Shoaib, T. *et al.* Stick-Slip Friction Reveals Hydrogel Lubrication Mechanisms. *Langmuir* **34**, 756–765 (2018).

102. Kim, J. & Dunn, A. C. Soft hydrated sliding interfaces as complex fluids. *Soft Matter* **12**, 6536–6546 (2016).
103. Meier, Y. A., Zhang, K., Spencer, N. D. & Simic, R. Linking Friction and Surface Properties of Hydrogels Molded against Materials of Different Surface Energies. *Langmuir* **35**, 15805–15812 (2019).
104. Cai, S., Hu, Y., Zhao, X. & Suo, Z. Poroelasticity of a covalently crosslinked alginate hydrogel under compression. 1–8 (2010). doi:10.1063/1.3517146
105. Cai, S., Lou, Y., Ganguly, P., Robisson, A. & Suo, Z. Force generated by a swelling elastomer subject to constraint. 1–7 (2010). doi:10.1063/1.3428461
106. Sneddon, I. N. The relation between load and penetration in the axisymmetric boussinesq problem for a punch of arbitrary profile. *Int. J. Eng. Sci.* **3**, 47–57 (1965).
107. Lin, W.-C., Shull, K. R., Hui, C.-Y. & Lin, Y.-Y. Contact measurement of internal fluid flow within poly(n-isopropylacrylamide) gels. *J. Chem. Phys.* **127**, 094906 (2007).
108. Zong, Z. *et al.* Indentation size effects in the nano and microhardness of FCC single crystal metals. *Mater. Manuf. Process.* **22**, 228–237 (2007).
109. Katsamenis, O. L., Jenkins, T. & Thurner, P. J. Toughness and damage susceptibility in human cortical bone is proportional to mechanical inhomogeneity at the osteonal-level. *Bone* **76**, 158–168 (2015).
110. Han, C. S. Influence of the molecular structure on indentation size effect in polymers. *Mater. Sci. Eng. A* **527**, 619–624 (2010).
111. Flory, P. J. Thermodynamics of High Polymer Solutions. *J. Chemical Phys.* **10**, (1942).
112. Flory, P. J. *Principles of polymer chemistry.* (Cornell University Press, 1953).
113. Flory, P. J. & Rehner, J. Statistical Mechanics of Cross-Linked Polymer Networks II. Swelling. *J. Chem. Phys.* **11**, 521–526 (1943).

114. Huggins, M. L. Solutions of long chain compounds. *The Journal of Chemical Physics* **9**, 440 (1941).
115. Durning, C. J. & Morman, K. N. Nonlinear swelling of polymer gels. *J. Chem. Phys.* **98**, 4275–4293 (1993).
116. Doi, M. Gel dynamics. *J. Phys. Soc. Japan* **78**, 1–19 (2009).
117. Ji, H., Mourad, H., Fried, E. & Dolbow, J. Kinetics of thermally induced swelling of hydrogels. *Int. J. Solids Struct.* **43**, 1878–1907 (2006).
118. Duda, F. P., Souza, A. C. & Fried, E. Journal of the Mechanics and Physics of Solids A theory for species migration in a finitely strained solid with application to polymer network swelling \$. *J. Mech. Phys. Solids* **58**, 515–529 (2010).
119. Chester, S. A. & Anand, L. A thermo-mechanically coupled theory for fluid permeation in elastomeric materials: Application to thermally responsive gels. *J. Mech. Phys. Solids* **59**, 1978–2006 (2011).
120. Bouklas, N. & Huang, R. Swelling kinetics of polymer gels: Comparison of linear and nonlinear theories. *Soft Matter* **8**, 8194–8203 (2012).
121. Gibbs, J. W. *The Scientific Papers of J. Willard Gibbs*. (1878).
122. Biot, M. A. Variational Lagrangian-thermodynamics of nonisothermal finite strain mechanics of porous solids and thermomolecular diffusion. *Int. J. Solids Struct.* **13**, 579–597 (1977).
123. Prigogine, I. *Introduction to Thermodynamics of Irreversible Processes, third ed.* (Wiley, New York, 1967).
124. Coleman, B. D. & Noll, W. The thermodynamics of elastic materials with heat conduction and viscosity. *Arch. Ration. Mech. Anal.* **13**, 167–178 (1963).
125. Scherer, G. W. Measuring Permeability of Rigid Materials by a Beam-Bending Method: I, Theory. *J. Am. Ceram. Soc.* **83**, 2231–2239 (2000).
126. Krevelen, D. W. van. *Properties of polymers*. (Elsevier, Amsterdam, 1990).

127. J. Brandrup, E. H. I. *Polymer handbook (3rd ed.)*. (Wiley, New York, 1989).
128. Barton, A. F. M. *CRC-handbook of polymer–liquid interaction parameters and solubility parameters*. (CRC press, Boca Raton, 1990).
129. Mark, J. E. *Physical properties of polymers handbook*. (American Institute of Physics, Woodbury, 1996).
130. R. A. Orwoll. The Polymer-Solvent Interaction Parameter X. *Rubber Chem. Technol.* **50**, 451–479 (1977).
131. Peppas, N. A. & Merrill, E. W. Determination of interaction parameter χ_1 , for poly(vinyl alcohol) and water in gels crosslinked from solutions. *J. Polym. Sci. Polym. Chem. Ed.* **14**, 459–464 (1976).
132. Mikos, A. G. & Peppas, N. A. Flory interaction parameter χ for hydrophilic copolymers with water. *Biomaterials* **9**, 419–423 (1988).
133. Cai, S. & Suo, Z. Equations of state for ideal elastomeric gels. *EPL* **97**, 8121–8128 (2012).
134. Nalam, P. C., Gosvami, N. N., Caporizzo, M. A., Composto, R. J. & Carpick, R. W. Nano-rheology of hydrogels using direct drive force modulation atomic force microscopy. *Soft Matter* **11**, 8165–8178 (2015).
135. Shull, K. R. *Contact mechanics and the adhesion of soft solids. Materials Science and Engineering: R: Reports* **36**, (2002).
136. Wahl, K. J., Asif, S. A. S., Greenwood, J. A. & Johnson, K. L. Oscillating adhesive contacts between micron-scale tips and compliant polymers. *J. Colloid Interface Sci.* **296**, 178–188 (2006).
137. Lai, Y. & Hu, Y. Unified solution for poroelastic oscillation indentation on gels for spherical, conical and cylindrical indenters. *Soft Matter* **13**, 852–861 (2017).
138. Alcaraz, J. *et al.* Correction of microrheological measurements of soft samples with atomic force microscopy for the hydrodynamic drag on the cantilever. *Langmuir* **18**, 716–721 (2002).

139. Weiss, N. & Silberberg, A. Inhomogeneity of Polyacrylamide Gel Structure from Permeability and Viscoelasticity. 144–150 (1977).
140. Hu, Y., Chen, X., Whitesides, G. M., Vlassak, J. J. & Suo, Z. Indentation of polydimethylsiloxane submerged in organic solvents. *J. Mater. Res.* **26**, 785–795 (2011).
141. Flory, P. J. THERMODYNAMIC RELATIONS FOR HIGH ELASTIC MATERIALS. *Trans. FARADAY Soc.* **57**, 829–838 (1960).
142. Hou, X., Hu, Y., Grinthal, A., Khan, M. & Aizenberg, J. Liquid-based gating mechanism with tunable multiphase selectivity and antifouling behaviour. *Nature* **519**, 70–73 (2015).
143. Archie, G. E. The electrical resistivity log as an aid in determining some reservoir characteristics. *Trans. AIME* **146**, 54–62 (1942).
144. Pisani, L. Simple Expression for the Tortuosity of Porous Media. 193–203 (2011). doi:10.1007/s11242-011-9734-9
145. Hunt, A. G., Ewing, R. P. & Sahimi, M. Tortuosity in Porous Media: A Critical Review. (2013). doi:10.2136/sssaj2012.0435
146. Kulasinski, K. & Guyer, R. A. Quantification of Nanopore Networks: Application to Amorphous Polymers. *J. Phys. Chem. C* **120**, 28144–28151 (2016).
147. Kapur, V., Charkoudian, J. C., Kessler, S. B. & Anderson, J. L. Hydrodynamic Permeability of Hydrogels Stabilized within Porous Membranes. *Ind. Eng. Chem. Res.* **5885**, 3179–3185 (1996).
148. Rubinstein, M. & Panyukov, S. Elasticity of polymer networks. *Macromolecules* **35**, 6670–6686 (2002).
149. Mooney, M. A theory of large elastic deformation. *J. Appl. Phys.* **11**, 582–592 (1940).
150. Blatz, Paul J., W. L. K. Application of finite elastic theory to the deformation of rubbery materials. *Trans. Soc. Rheol.* **6**, 223–252 (1962).

151. Koningsveld, R. & Kleintjens, L. A. Liquid-liquid phase separation in multicomponent polymer systems. X. Concentration dependence of the pair-interaction parameter in the system cyclohexane-polystyrene. *Macromolecules* **4**, 637–641 (1971).
152. Koningsveld, R. & Kleintjens, L. A. Liquid-liquid phase separation in multicomponent polymer systems. 22. Thermodynamics of statistical copolymers. *Macromolecules* **18**, 243–252 (1985).
153. Orakdogan, N. & Okay, O. Correlation between crosslinking efficiency and spatial inhomogeneity in poly(acrylamide) hydrogels. *Polym. Bull.* **57**, 631–641 (2006).
154. Denisin, A. K. & Pruitt, B. L. Tuning the Range of Polyacrylamide Gel Stiffness for Mechanobiology Applications. *ACS Applied Materials and Interfaces* **8**, 21893–21902 (2016).
155. Netz, P. A. & Dorfmueller, T. Computer simulation studies on the polymer-induced modification of water properties in polyacrylamide hydrogels. *J. Phys. Chem. B* **102**, 4875–4886 (1998).
156. Hui, C., Liu, T., Salez, T., Raphael, E. & Jagota, A. Indentation of a Rigid Sphere Into an Elastic Substrate with surface tension and adhesion. *Proc. R. Soc. A Math. Phys. Eng. Sci.* **471**, (2015).
157. Style, R. W., Hyland, C., Boltyanskiy, R., Wettlaufer, J. S. & Dufresne, E. R. Surface tension and contact with soft elastic solids. *Nat. Commun.* **4**, 1–6 (2013).
158. Liu, T., Jagota, A. & Hui, C. Y. Effect of surface tension on the adhesion between a rigid flat punch and a semi-infinite neo-Hookean half-space. *Extrem. Mech. Lett.* **9**, 310–316 (2016).
159. Long, J., Wang, G. F., Feng, X. Q. & Yu, S. Effects of surface tension on the adhesive contact between a hard sphere and a soft substrate. *Int. J. Solids Struct.* **84**, 133–138 (2016).
160. Hui, C., Liu, T., Salez, T., Raphael, E. & Jagota, A. Indentation of a Rigid Sphere Into an Elastic Substrate with surface tension and adhesion. *Proc. R. Soc. A Math. Phys. Eng. Sci.* **471**, (2015).

161. Tang, T., Hui, C. Y. & Glassmaker, N. J. Can a fibrillar interface be stronger and tougher than a non-fibrillar one? *J. R. Soc. Interface* **2**, 505–516 (2005).
162. Wang, J. & Gao, H. Size and shape dependent steady-state pull-off force in molecular adhesion between soft elastic materials. *Int. J. Fract.* **166**, 13–19 (2010).
163. Kii, A., Xu, J., Gong, J. P., Osada, Y. & Zhang, X. Heterogeneous polymerization of hydrogels on hydrophobic substrate. *J. Phys. Chem. B* **105**, 4565–4571 (2001).
164. Gombert, Y. *et al.* Structuring Hydrogel Surfaces for Tribology. *Adv. Mater. Interfaces* **1901320**, (2019).
165. Shoaib, T. & Espinosa-Marzal, R. M. Insight into the Viscous and Adhesive Contributions to Hydrogel Friction. *Tribol. Lett.* **66**, 1–14 (2018).
166. Li, H., Choi, Y. S., Rutland, M. W. & Atkin, R. Nanotribology of hydrogels with similar stiffness but different polymer and crosslinker concentrations. *J. Colloid Interface Sci.* **563**, 347–353 (2020).
167. Gundogan, N., Okay, O. & Oppermann, W. Swelling, elasticity and spatial inhomogeneity of poly(N,N- dimethylacrylamide) hydrogels formed at various polymer concentrations. *Macromol. Chem. Phys.* **205**, 814–823 (2004).
168. Flory, P. J. & Rehner, J. Statistical mechanics of cross-linked polymer networks II. Swelling. *J. Chem. Phys.* **11**, 521–526 (1943).
169. Davidson, J. D. & Goulbourne, N. C. A nonaffine network model for elastomers undergoing finite deformations. *J. Mech. Phys. Solids* **61**, 1784–1797 (2013).
170. Bohdanecký, M., Petrus, V. & Sedláček, B. Estimation of the characteristic ratio of polyacrylamide in water and in a mixed theta-solvent. *Die Makromol. Chemie* **184**, 2061–2073 (1983).
171. Tehrani, M. & Sarvestani, A. Effect of chain length distribution on mechanical behavior of polymeric networks. *Eur. Polym. J.* **87**, 136–146 (2017).
172. Lu, J., Zhang, H. & Yang, Y. Monte Carlo simulation of kinetics and chain-length distribution in radical polymerization. *Macromol. Theory Simulations* **2**, 747–760

(1993).

173. Hamzehlou, S., Reyes, Y. & Leiza, J. R. A new insight into the formation of polymer networks: A kinetic monte carlo simulation of the cross-linking polymerization of S/DVB. *Macromolecules* **46**, 9064–9073 (2013).
174. Chang, C. M., Lau, Y. G., Tsai, J. C. & Juan, W. T. Relaxation of DNA on a supported lipid membrane. *Epl* **99**, (2012).
175. Yang, Q. H., Qian, C. J., Li, H. & Luo, M. B. Dynamics of a polymer adsorbed to an attractive homogeneous flat surface. *Phys. Chem. Chem. Phys.* **16**, 23292–23300 (2014).
176. Källrot, N., Dahlgvist, M. & Linse, P. Dynamics of polymer adsorption from bulk solution onto planar surfaces. *Macromolecules* **42**, 3641–3649 (2009).
177. Haschke, H., Miles, M. J. & Koutsos, V. Conformation of a Single Polyacrylamide Molecule Adsorbed onto a Mica Surface Studied with Atomic Force Microscopy. 3799–3803 (2004). doi:10.1021/ma035881j